Diamond coated carbon nanotube teepee structures as electrodes

Rosie Huggon

April 2013

Supervisor: Professor Paul May

Second assessor: Dr David Fermín

This thesis is submitted in partial fulfilment of the requirements for the Honours degree of Chemistry BSc at the University of Bristol

Acknowledgements

I would like to say a huge thank you to both my supervisor, Professor Paul May and my second assessor, Dr David Fermín. I am extremely grateful for your patience, guidance and support throughout the year. Your encouragement has given me a lot more confidence when approaching practical and theoretical problems.

I would like to thank my post doc, Dr Daniela Plana for the vast amount of time and ideas given during my time in the electrochemistry lab. Again, I am extremely grateful.

I would also like to thank Jonathan Jones for his time and technical help while using the SEM facilities.

I am finally very grateful to be given the experience of working in such inspirational and enjoyable lab groups. Both the diamond and the electrochemistry group were so kind and happy to help. It's been a pleasure!

Contents

Rosie Huggon

Electrochemical electrodes made from conducting diamond.

Abstract

Two samples of Multi-walled carbon nanotubes (MWNT's) of different lengths on a silicon substrate have been seeded with a nanodiamond suspension in methanol using electrospray deposition. As a result of this process, 'teepee' structures have formed in which groups of carbon nanotubes (CNT's) have clumped together. Using the chemical vapour deposition (CVD) reactor, the diamond morphologies and boron doping levels have been varied to obtain a range of samples. These samples have been made into electrodes that have successfully been used in electrochemistry with both a ferri/ferro cyanide system and a potassium chloride system. Perfectly reversible cyclic voltammogram (CV) curves have been obtained from a highly doped nano-crystalline diamond teepee sample B electrode using a ferri/ferro cyanide system and a diffusion coefficient of 4.56×10^{-6} cm^2 s^{-1} has been calculated which corresponds with values reported in the literature. Impedance measurements have allowed the surface area of these electrodes to be calculated and the boron doped diamond (BDD) teepee structures have proven to have up to 4.4 times the surface area than flat BDD electrodes. A theoretical range of relative surface area has been calculated as 432.24 - 1512.84.

1. Introduction

1.1 An introduction to diamond

Diamond is one of 10 allotropes of carbon (see figure 1 [1]). Along with graphite, it is one of the best known and arguably one of the most useful allotropes of carbon. Other allotropes include: Lonsdaleite, C_{540}, C_{70} and multi walled carbon nanotubes.

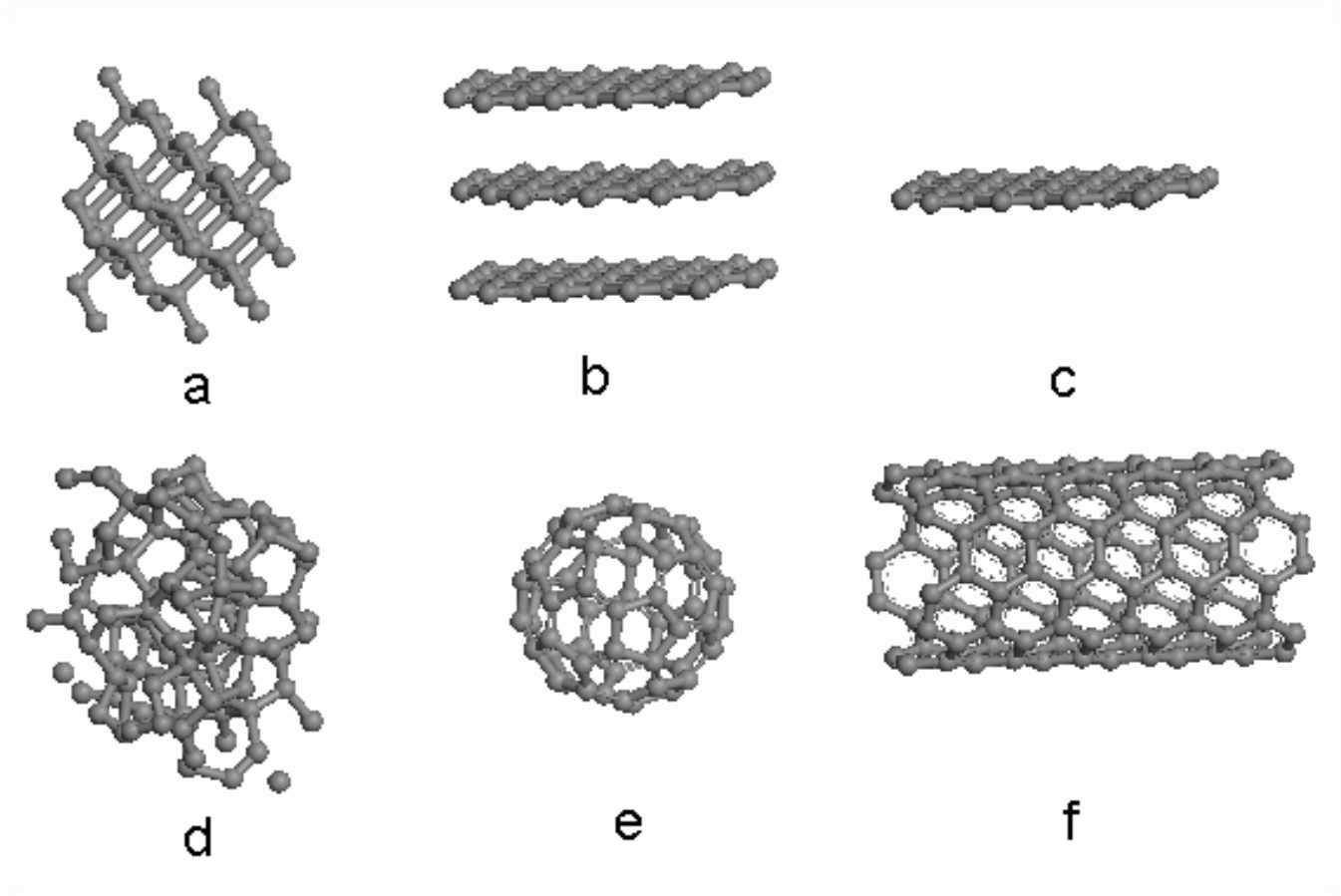

Figure 1 – Allotropes of carbon: a) Diamond b) Graphite c) Graphene d) Amorphous carbon e) C_{60} – Buckminsterfullerene f) Single walled carbon nanotube.

Graphite is the most thermodynamically stable form of carbon at room temperature and pressure. Despite a relatively small difference in the standard enthalpy of formation between diamond and graphite (2.9 kJ mol^{-1}), [2, 3] the phase diagram of carbon in figure 2 [4] shows that a large activation

energy barrier means it is kinetically unfavourable for diamond to transform into graphite under normal temperature and pressure conditions.

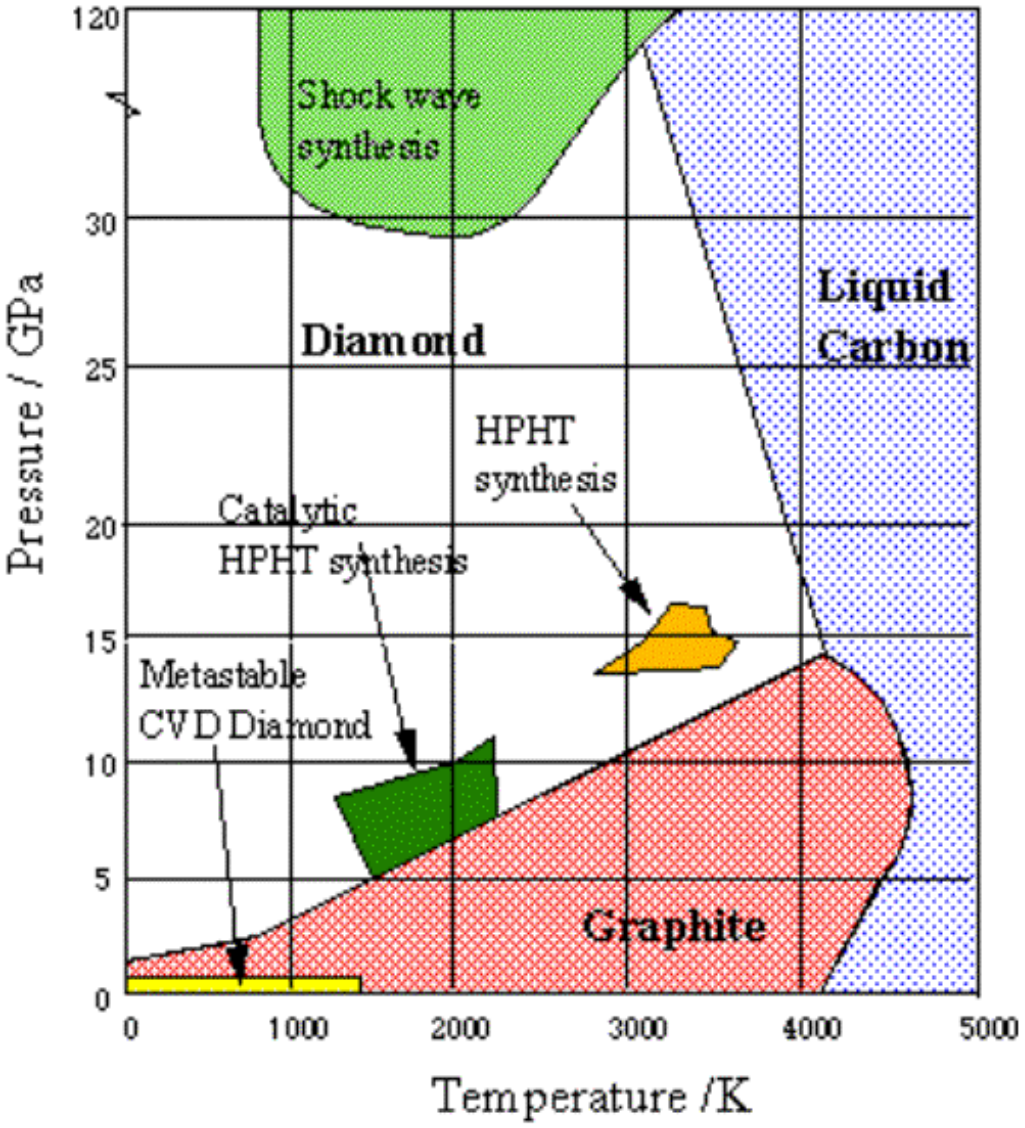

Figure 2 – Phase diagram of carbon

Figure 3 [5] shows the diamond lattice is formed from a repeating pattern of carbon atoms in a cubic structure.

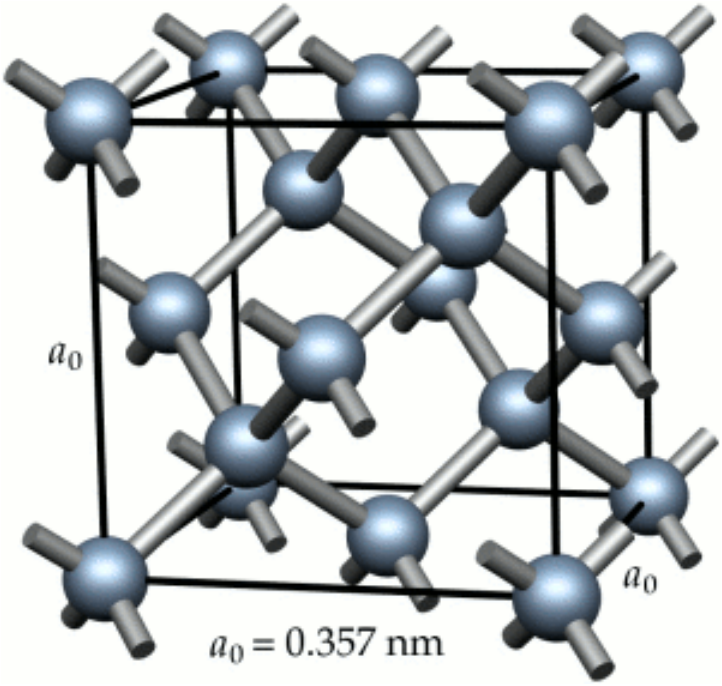

Figure 3 – Unit cell of diamond

Fundamental differences in bonding between diamond and graphite allotropes give rise to some dramatically different properties:

Diamond

- sp^3 hybridised
- Tetrahedral bonding – each C atom bonded to 4 neighbouring atoms
- Cubic crystal structure

Graphite

- sp^2 hybridised
- Each C atom bonded to 3 neighbouring atoms – layered planar structure
- Hexagonal crystal structure
- Delocalised π electrons above and below the planes of carbon atoms
- Weak Van der Waals forces between planar layers of carbon atoms

1.2 Properties of diamond in electrochemistry

The use of diamond in electrochemistry was pioneered by Pleskov et al in 1987 [6] and research and interest has continued to develop [7]. Diamond possesses some extraordinary physical properties as seen in table 1.

Property	**Magnitude**
Hardness	1×10^{4} kg mm^{-2}
Thermal expansion coefficient	1×10^{-6} K^{-1}
Thermal conductivity	20.0 W cm^{-1} K^{-1}
Heat capacity	6.2 Jmol^{-1}K^{-1}
Electron mobility	2200 cm^{2}V^{-1}s^{-1}
Hole mobility	1600 cm^{2}V^{-1}s^{-1}
Band gap	5.5 eV
Resistivity of undoped diamond	$\sim10^{16}$ Ohm cm

Table 1 – A table to show some of the physical properties of diamond.

These properties are particularly useful when using diamond as an electrode:

- Diamond has a wide potential window in aqueous solution with low background currents allowing for higher sensitivity and lower detection limits. [8-11]
- The diamond surface is stable allowing for a long term stability of response.[12-15]
- The properties of polycrystalline diamond do not differ much from those of bulk diamond [16-18] including:

    - Diamond has high thermal conductivity allowing it to be used as a heat sink. [19-24]
    - Diamond is chemically inert at room temperature and pressure allowing it to be used as a medical and biological sensor. [25-34]
    - Diamond has a good voltammetric response with no need for surface treatment/conditioning. [35-38]
    - Diamond shows transparency over a broad spectral range resulting in optical use over a large spread of wavelengths. [39, 40]

- Diamond has a Negative Electron Affinity (NEA) allowing its use in field emission devices. [41]
- Diamond has little chemical reactivity allowing it to be used in harsh chemical environments. [42]
- Diamond is the hardest known natural material making it ideal for use in radiation technology. [43, 44]
- Diamond is an electrical insulator with a wide band gap of 5.5 eV. [6]

1.3 Changing the electronic properties of diamond

Due to the electrical insulation properties of diamond, its other unique physical properties are of little use in an electrical context unless diamond can be made electronically active.

Surface termination of diamond is one way of making it electronically functional. Hydrogen terminated diamond surfaces show strong negative electron affinity with surface carrier densities up to 10^{13} cm^{-2} [46] allowing p-type conductivity on the surface. Well defined voltammetric responses for the reduction of $Rh(NH_3)_6^{3+}$ in aqueous 0.1 M KCl (an outer sphere, one electron transfer process) have been obtained for BDD electrodes after H plasma treatment. [47,48]

Oxidised surfaces show insulating characteristics and a positive electron affinity. Both hydrogenated and oxidised diamond surfaces offer properties suitable for different applications. For example, hydrogen terminated surfaces are a lot more hydrophobic than those of oxygen. [49]

Doping diamond with impurities is another way of modifying it to make it electronically active. The technique of synthetically growing diamond through Chemical Vapour Deposition (CVD) allows these modifications to be made. Figure 4 [50] shows a schematic energy level diagram for diamond indicating the band gap and the n and p energy states.

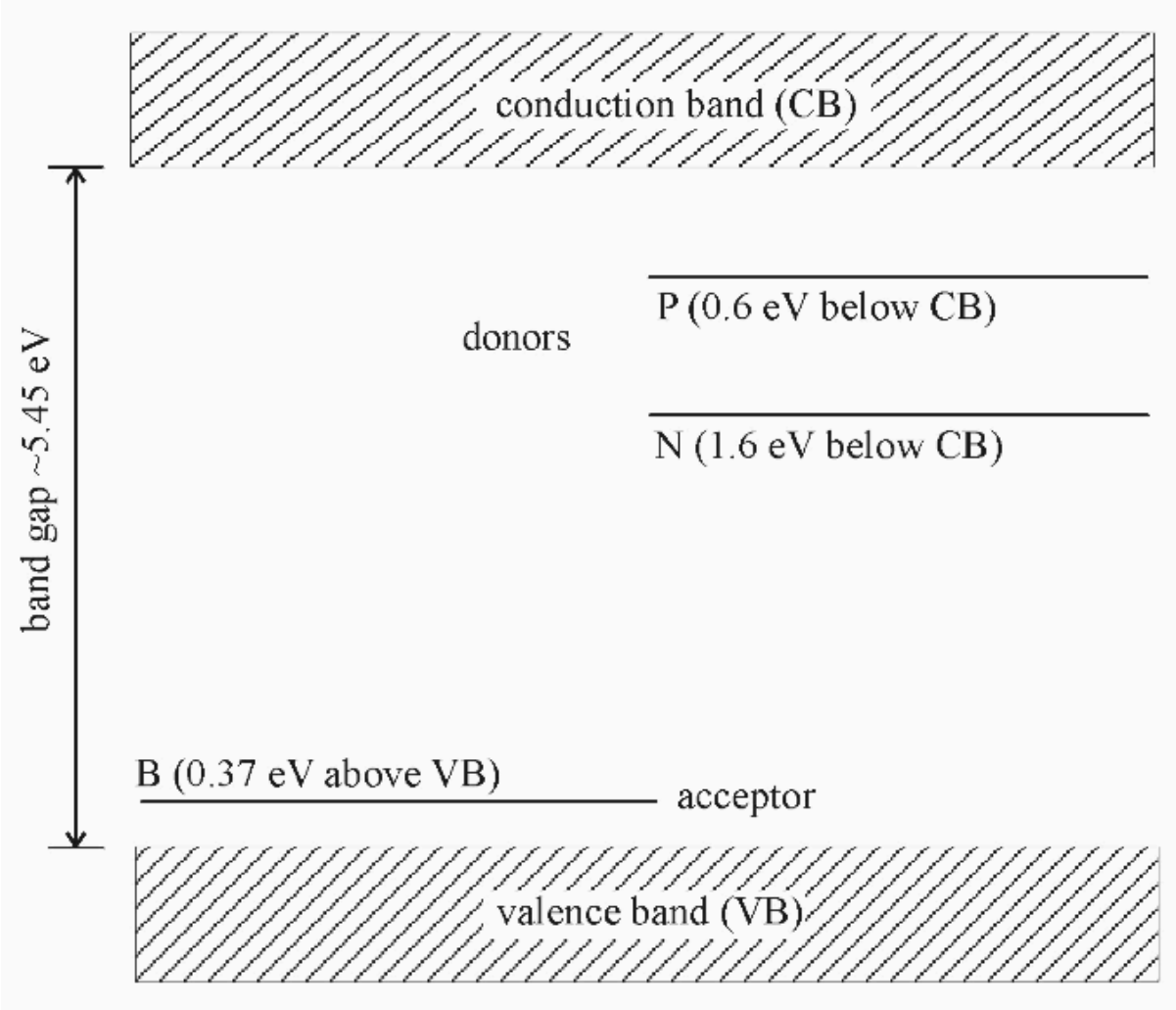

Figure 4 – Schematic energy level diagram for diamond showing the conduction and valence bands indicating the n and p energy states

Impurities such as phosphorus and nitrogen are donor atoms. Doping with atoms such as these induces n-type behaviour. Donor atoms allow the addition of another electronic energy state (in the insulating gap of diamond) that resides close to the conduction band as seen in figure 5. Electrons thermally excited from the new additional donor band to the conduction band are now free to carry charge. [51]

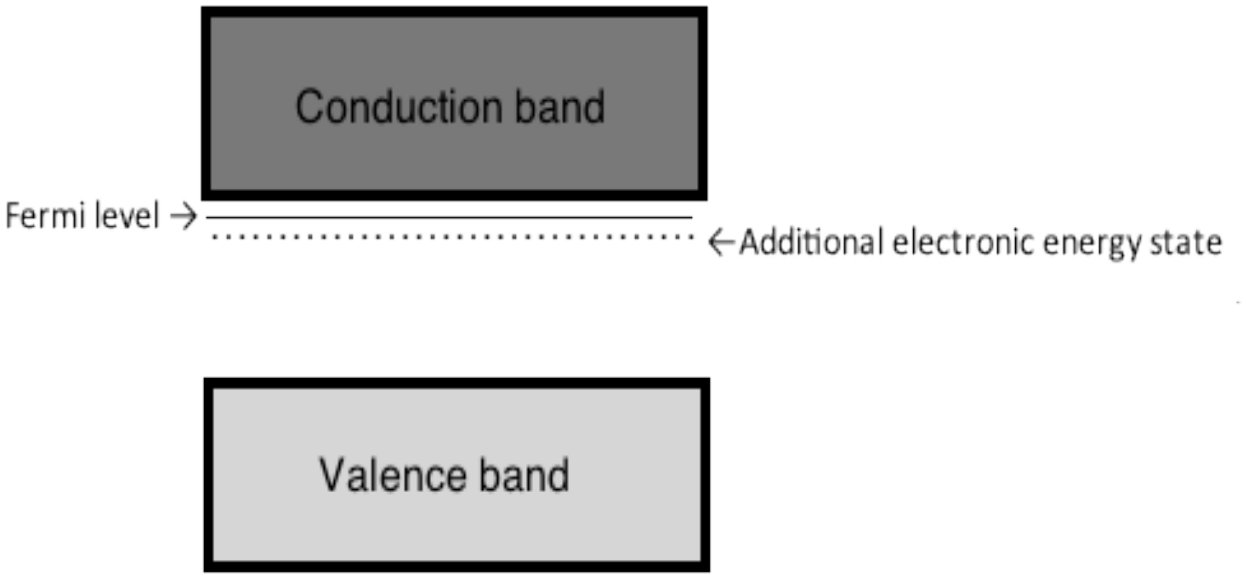

Figure 5 – A diagram to show the band theory in N-type semiconductors.

Doping diamond with boron – an acceptor impurity – gives rise to p-type behaviour. Boron with activation energy 0.37 eV [45] has an electron deficiency in its valance shell – hence an acceptor impurity. Boron is the most common acceptor impurity when using diamond as its atomic radius is similar to that of carbon so it is easily accommodated in the diamond lattice. The acceptor impurities create extra holes in the insulating band gap of diamond, [52] as seen in figure 6, allowing the thermal excitation of electrons from the valance band to the extra acceptor holes giving rise to semiconductor properties.

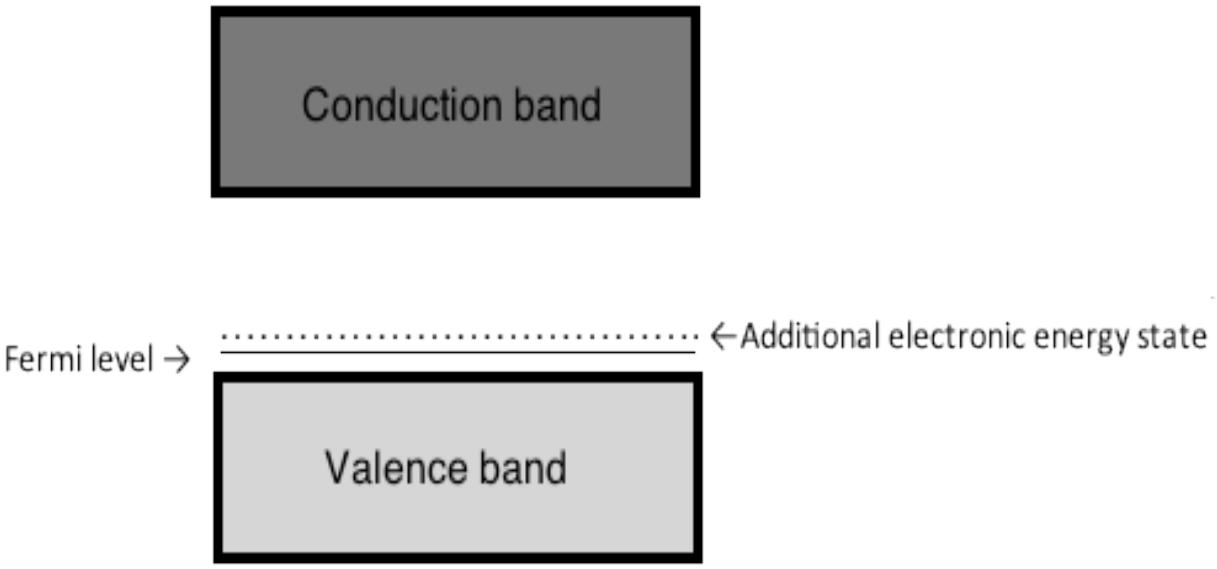

Figure 6 – A diagram to show the band theory in P-type semiconductors.

1.4 Boron doping.

At low doping levels, diamond behaves as a semiconductor and band conduction dominates. Boron doping levels of 3.92×10^{21} cm^{-3} give rise to a low temperature metal to insulator transition, [53] however, semiconductor properties can be observed at much lower doping levels where carrier mobility is sufficient to allow current to flow. [54] The resistivity of diamond is 10^4 Ω cm when doped with 10^8 boron atoms/cm.

At higher doping levels of approximately 10^{20} cm^{-3} i.e. one boron atom per 1000 carbon atoms[55] (see figure 7 [56]) the resistivity of diamond drops to 10^{-3} Ω cm and it behaves as a semimetal [57]. Here impurity band conduction dominates. [48, 59]

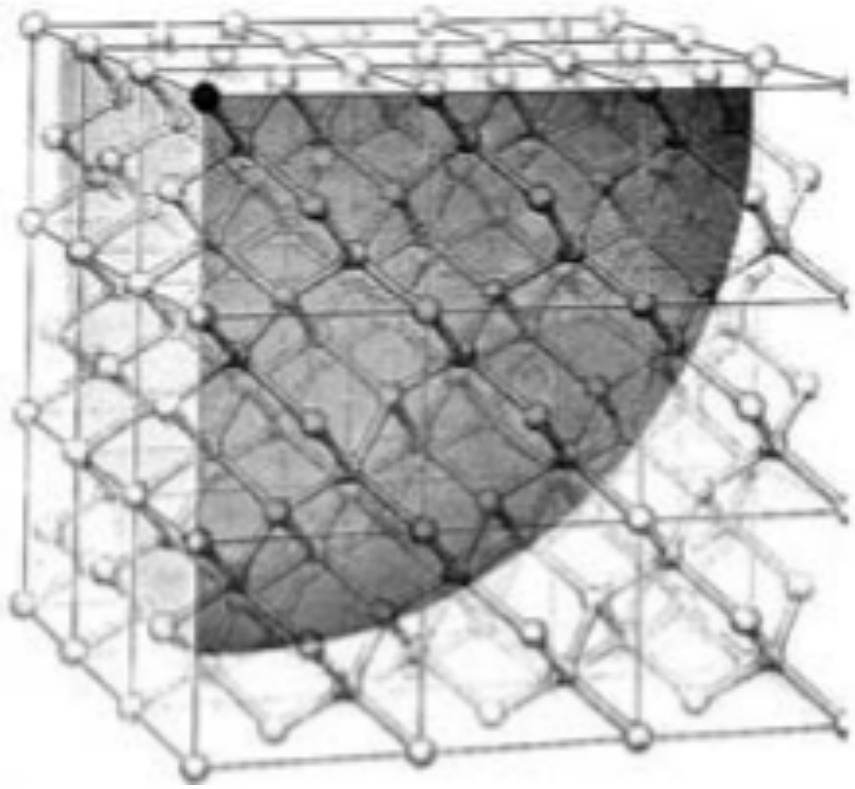

Figure 7 - Schematic diagram of a diamond lattice with boron atom surrounded by a sphere indicating the mobility of the charge carrier

The number of vacant sites/charge carriers decreases non-linearly as resistivity increases as seen in figure 8. [60] At high doping levels the charge carrier concentration is effectively equal to the doping concentration. [61] The increased number of vacant sites/charge carriers lowers the Fermi level. [62] Metallic behaviour is observed when the impurity band and the valance band meet. [63]

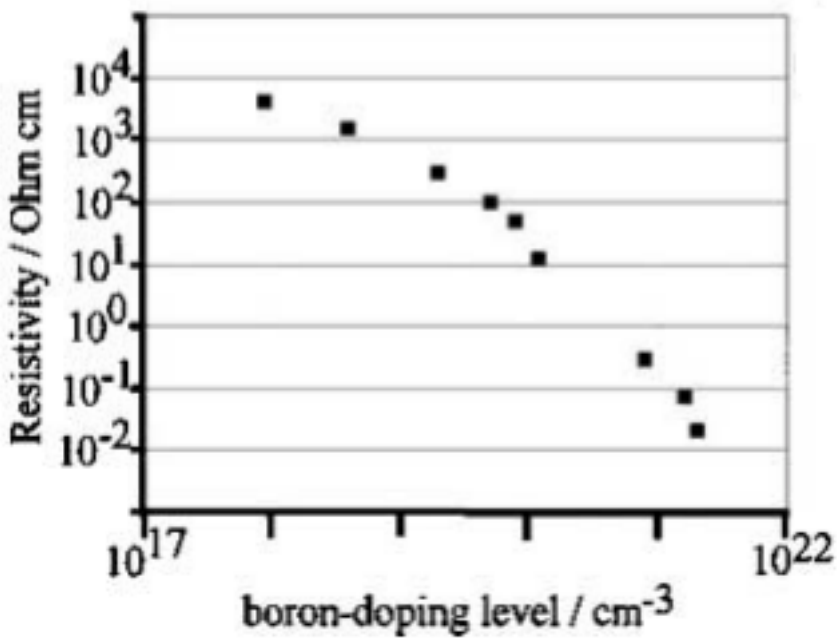

Figure 8 - Plot of the room temperature resistivity of boron-doped diamond as a function of boron doping level

1.5 Polycrystalline diamond films

Polycrystalline diamond films can be grown using gas or plasma phase deposition procedures. [64, 65] Depending on the substrate, the gases used and the parameters employed during growth, there are a number of diamond morphologies possible. Substrates need to have a tolerance of high deposition temperatures along with a similar thermal expansion coefficient to diamond. Typical substrates used are carbon and carbon cloth, [66, 67] silicon, [68] graphite, [69] niobium, [70] tungsten [71] and molybdenum.[72] The two most common forms of diamond thin films are microcrystalline and nanocrystalline. A mixture of two gases, (one carbon containing) are used for deposition to make diamond films. Different gas concentrations create different crystal morphologies. [73] Boron doped microcrystalline and nanocrystalline diamond films boast a number of electrochemical properties that set them apart from other sp^2 hybridised carbon electrodes such as glassy carbon, pyrolytic graphite and carbon paste. [74, 75]

The surface of polycrystalline diamond electrodes may need renewing and this can be done through a number of ways:

- H-plasma treatments [76]
- F-plasma treatments [77]
- O-plasma treatments [78]
- Anodic or cathodic potential treatments [79]
- Electron beam surface desorption [80]

The diamond surface can also be modified by incorporating metals or metal oxides by plasma or electrochemical treatments. Incorporating poorly conducting metal oxides (which are active electrocatalysts) by deposition allows the BDD to act as an inert and electrically conducting substrate where reactions occur at the region in which the catalyst, electrode and solution meet. [81]

1.5.1 Microcrystalline diamond films

In microcrystalline diamond the grain size varies from 0.1-10 μm. With increased deposition time, the crystallite size gets bigger along with film thickness. This gives rise to the columnar structure (as seen in figure 9 [82]) that reflects the van der Drift growth mechanism [83] and is common in films made from methane/hydrogen gas mixtures. sp^3 hybridised diamond is made through an elaborate nucleation and growth mechanism. [84, 85]

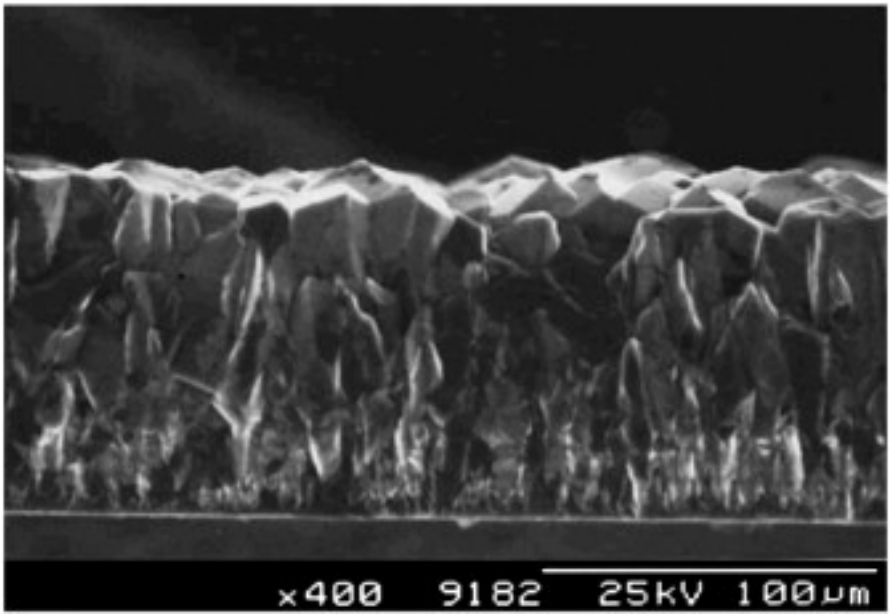

Figure 9 – Columnar structure of microcrystalline diamond

Miller indices describe the crystal planes that control the morphology of the diamond film. [86] There are 3 main planes associated with microcrystalline morphology: <111>, <110> and <100>. Figure 10 [87] shows the SEM images of each plane.

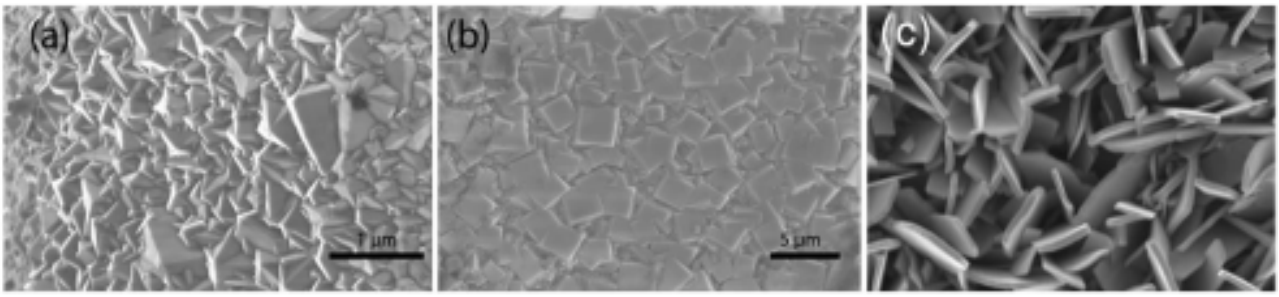

Figure 10 - SEM images of the 3 planes associated with microcrystalline morphology: a) <111> b) <100> c) <110>

1.5.2 Nanocrystalline diamond films

Nanocrystalline diamond films comprise of crystals with grain size on the nano scale. Different characteristics can be observed amongst diamond films that fall into the nanocrystalline family depending on grain size, for example some films will show columnar growth similar to that seen in microcrystalline films. Nanocrystalline diamond films can be produced from methane/argon gas mixtures. [88, 89] Nano and micro crystalline diamond have different properties as a result of the difference in crystallite size. Nanocrystalline films possess smoother surfaces as a result of the high nucleation rate in the gas mixture, [90] and also a smoother surface area across the film. High surface area along with the high surface energy of nano materials is one of the reasons they are more effective than bulk materials. [100, 101] Nanocrystalline diamond films contain more sp^2 character whereas microcrystalline diamond films contain more sp^3 character. Each crystallite is terminated by sp^2 hybridised carbon, therefore the smaller the crystallite size, the greater the sp^2 content. Although a high sp^3 content diamond film (such as microcrystalline) may seem of better quality, the properties of nanocrystalline films are sometimes preferred to those of microcrystalline. [102, 103] Nanocrystalline films have been proven to be much better field electron emitters. [104, 105]

1.5.3 Ultrananocrystalline diamond films

Ultrananocrystalline diamond is a highly graphitic material [106] with a diamond grain size towards the lower end of the nanoscale with a structure of order of 5nm. [107] Ultrananocrystalline diamond can be grown by incorporating an inert gas into the CVD growth. [108] These diamond films have different properties to a typical nanocrystalline diamond film hence why they can be categorised differently. Their surfaces are extremely smooth due to their grain size but unexpectedly, the crystallite boundary has a lower sp^2 carbon content. [109] Ultrananocrystalline diamond films can give acceptable material properties and are easier to produce over large areas making ultrananocrystalline diamond an excellent material for use in electrochemistry in certain applications. Ultrananocrystalline diamond has been proven as an effective dielectric, [110] and a good n-type semiconductor when nitrogen is used during the CVD. [111]

1.5.4 CVD diamond growth

The chemical vapour deposition time is an important factor when growing polycrystalline diamond thin films. Figure 11a) [112] shows an SEM image of poor diamond seeding as a result of 15 minutes deposition time. The diamond coating is too thin meaning that the teepee structures are not thoroughly developed and the structure is not robust. On the other hand figure 11 b) [112] shows teepee structures embedded in the CVD diamond after a 5 hour deposition time. Figure 11 c) [112] shows the ideal teepee continuous network after a deposition time of 1.5 hours.

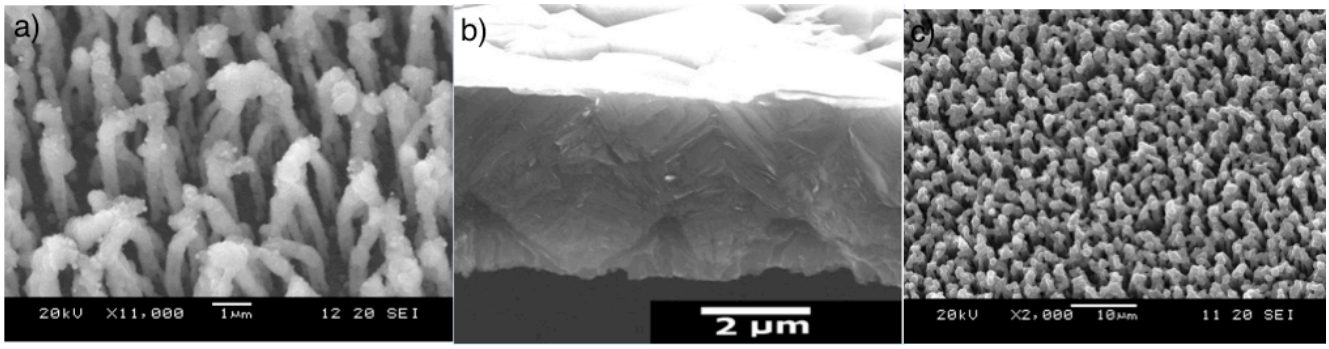

Figure 11 – a) 15 minutes CVD b) 5 hours CVD c) 1.5 hours CVD

1.6 Nanodiamond cone arrays

Conical arrays display properties that cannot be seen in bulk or film forms of diamond. [113, 114] There are 3 steps involved in structuring diamond cone arrays:

1) Nucleation (using methane and hydrogen gases)
2) Growth of micro/nanocrystalline diamond films (using methane and hydrogen gases)
3) In situ bias-assisted reactive ion etching

In the work by Sun et al, [115] a 1% methane: 99% hydrogen ratio microwave CVD process was used to prepare the microcrystalline diamond films and a 10% methane: 90% hydrogen ratio with a similar process was used for the preparation of the nanocrystalline diamond films. The reactive ion etching process followed, by delivering only hydrogen through the reactor.

The reactive ion etching process converts the whole flat nanodiamond film into a conical array as seen in figure 12 [116] which shows different cone densities depending on the etching parameters (reactant pressure and input microwave power) used.

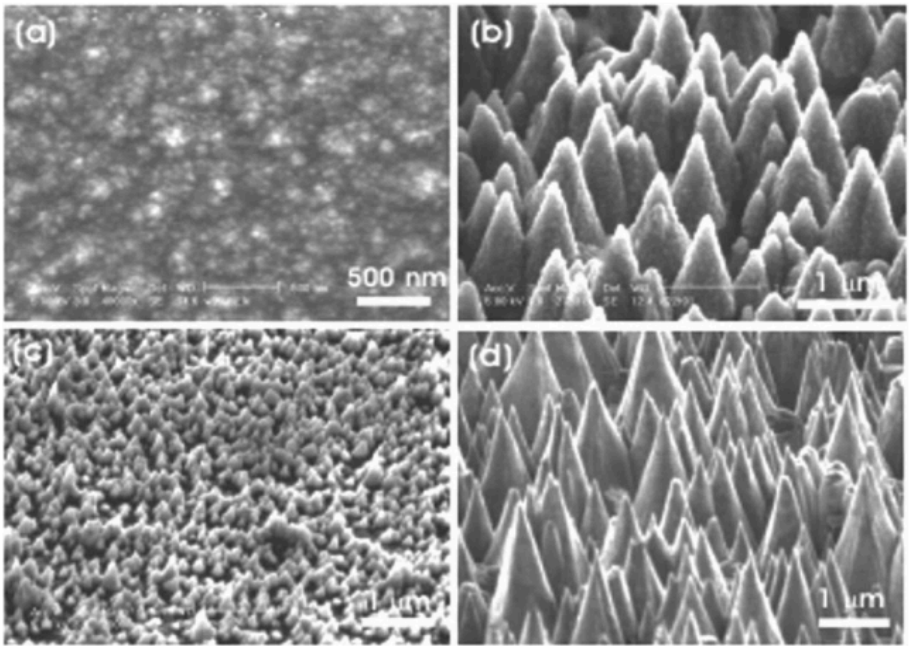

Figure 12- SEM images from a) the nanocrystalline diamond film with a flat surface b) low-density nanodiamond cones c) high-density nanodiamond cones d) single-crystal diamond cones

When the cone density increases by an order of magnitude- $2\times10^8/cm^2$ versus $3\times10^9/cm^2$ the cone height decreases by 100nm. When using microcrystalline as opposed to nanocrystalline diamond under the same etching parameters, the cone height was considerably larger. High-resolution transmission electron microscopy established that each cone consisted of a single crystalline diamond. [117]

Diamond cone arrays are formed by energetic hydrogen ion impact followed by chemical etching of the graphitic layer. The time difference between the etching of the cone head and cone base is responsible for the shape of the cone. Cone shape mainly depends on the etching parameters, whether the film is nanocrystalline or microcrystalline is irrelevant here. It is however relevant when considering the cone composition where nanocrystalline diamond forms nanodiamond cones and microcrystalline diamond forms single crystal cones.

Nanodiamond films have a columnar structure of nanocrystallites with the same orientation and clear grain boundaries. It is uncertain whether the columnar structure of the films gives rise to the cone shape. Reactive plasma etching causes electron emission from the films, this is more concentrated in the grain boundaries. As a result of uneven distributions of plasma sheath and electrical field across the film, the etching rate by energetic hydrogen ions is higher in the column boundary regions. Diamond is etched away from the edges of the columns at a faster rate leaving diamond cone arrays in the original columnar structure of the nano/microcrystalline film.

Zhang et al [118] have shown firstly that the cone array structure improves field electron emission of both nanocrystalline and microcrystalline films. Secondly that the field electron emission is better in nanocrystalline rather than microcrystalline structured diamonds if the structured geometry is the same. And thirdly that the less dense of two given cone arrays yields better field electron emission properties.

1.7 Micro/multi-electrode arrays

An electrode with more than one dimension smaller than 25μm can be described as a microelectrode. Advantages of microelectrodes include: [119, 120]

- Enhancing the response while holding onto the properties of single microelectrodes

- Low double layer capacitance
- Small ohmic drop
- Allowing steady-state limiting currents to be achieved
- Improved rate of mass transport of electroactive analyte to the microelectrode surface due to small diffusion layer across the surface and the convergent diffusion at its edges
- Excellent spatial and temporal resolution

There are several ways of fabricating MEA's including photo resist patterning, [121] photolithography, [122] and silicon nitride patterning. [123]

The fabrication process used by Kang et al [124] used a highly doped silicon substrate in a microwave plasma enhanced chemical vapour deposition system using a gas mixture of $H_2/CH_4/N_2$ as described in figure 13. [124]

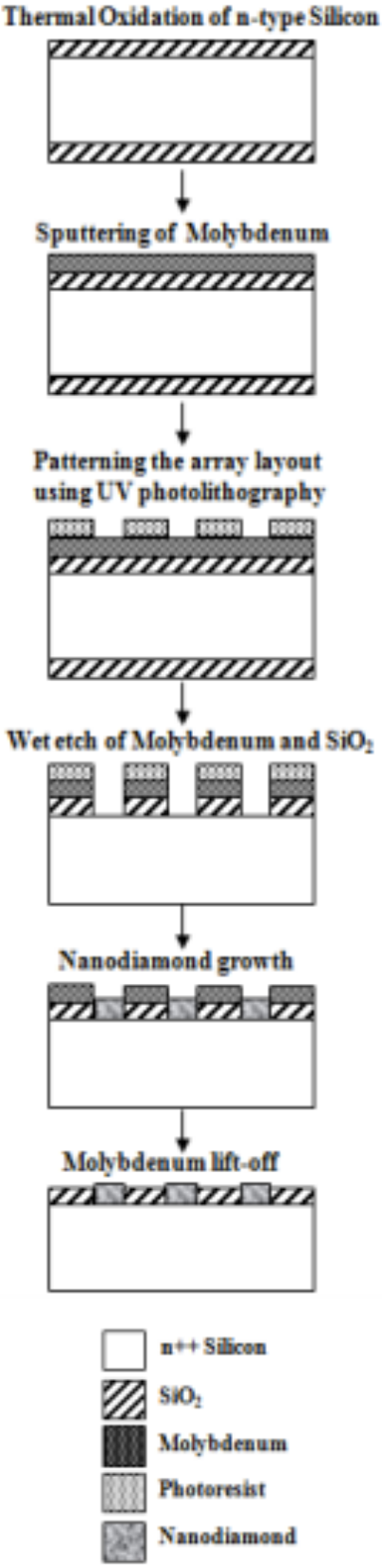

Figure 13 - Schematic diagram for fabrication of a 20x20 nanodiamond microelectrode array (MEA)

Figure 14 [124] shows SEM micrographs of the microelectrode array and an individual microelectrode respectively.

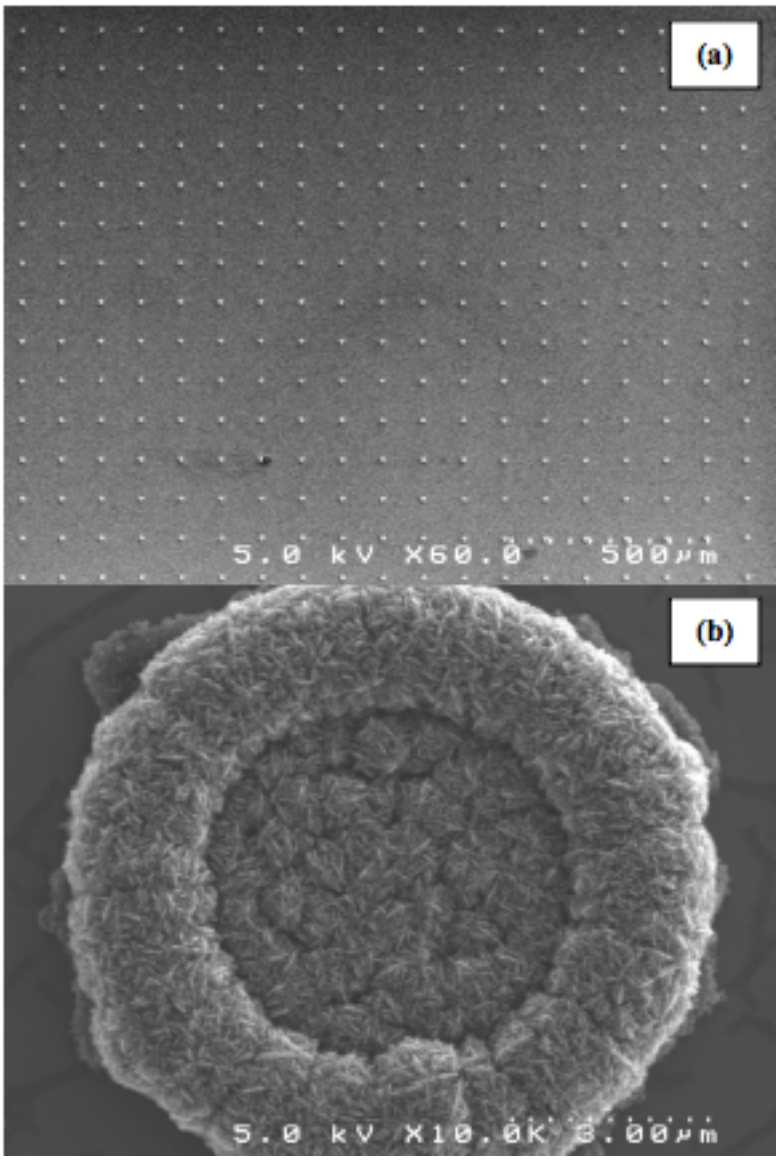

Figure 14 - a) SEM image of 20 x 20 array showing layout of the microelectrodes
b) SEM image at higher magnification of an individual microelectrode

Kang et al [124] reported using the micro-electrode, cyclic voltammograms were produced from examining the $Fe(CN)_6^{-3/4}$ redox reaction in 0.1M KCl. The CV's show the sigmoidal curve when potassium ferrocyanide is added. This shows steady-state conditions as a result of hemispherical diffusion-limited mass transport mechanism. When linear calibration curves were plotted for a 1mM-10mM concentration range, the sensitivity of the micro-electrode array was found to be 15

times greater than that of the macro-electrode (from the gradient of the curve.) This increased sensitivity can be put down to the high flux at the electrode surface.

1.8 Interdigitated array disc electrodes

Hot filament chemical vapour deposition and photoetching technology has been used by Zhong et al [125] to produce an interdigitated array disc electrode containing both insulating and conducting diamond structures. Figure 15 [125] shows images of the electrode, the part electrode and a close up of the part electrode.

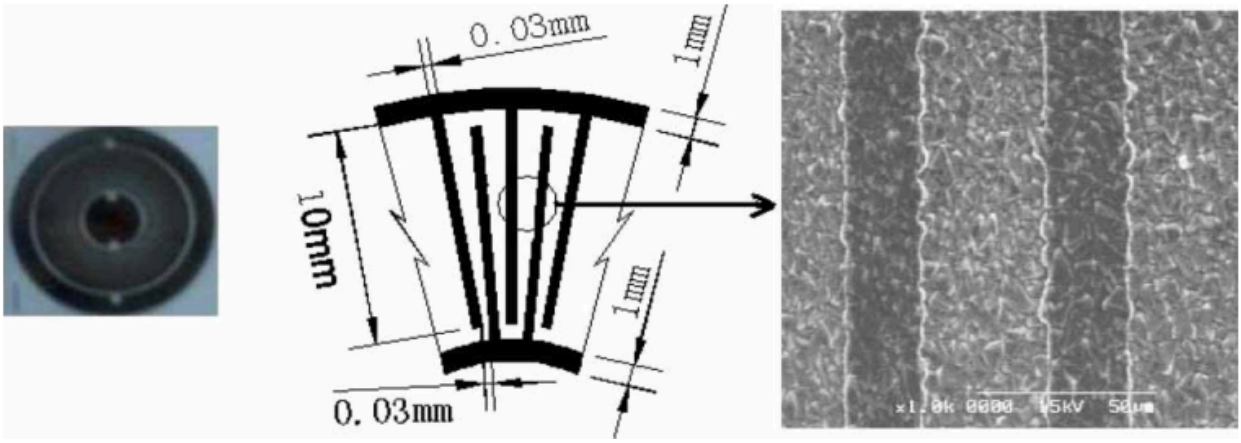

Figure 15- Boron-doped diamond interdigitated array disc electrode: (a) the photo of the electrode; (b) the sketch image of the part electrode; (c) the SEM image of the part electrode

Cyclic voltammetry of the interdigitated array disc electrode was found to be similar to that of a macro-electrode and its applications are thought to be important in harsh chemical environments such as strong acids and alkalis and also in high temperatures.

1.9 Carbon nanotubes

Carbon nanotubes have an impressive selection of electronic, structural and mechanical properties such as high strength, dimensions on the nanoscale, high aspect ratio and excellent current carrying ability [126] all of which make them ideal for use in electrochemistry. They are chemically stable, have a wide electrochemical potential window and show low capacitance in the pristine state from

low density of states of single walled nanotubes. [127, 128] Britto et al [129] were the pioneers of using carbon nanotubes as electrodes in 1996.

Carbon nanotubes are made up of sp^2 hybridised carbon. The most common ways of fabricating carbon nanotubes include: [30]

- High pressure carbon monoxide – often produces by-products requiring post growth cleaning
- Laser ablation – often produces by-products requiring post growth cleaning
- Electric arc discharge – often produces by-products requiring post growth cleaning
- Catalysed chemical vapour deposition – high crystallinity and low defect density can be achieved with carefully optimised conditions

The majority of carbon nanotubes are grown commercially using high pressure carbon monoxide, electric arc discharge or laser ablation. Metallic nanoparticle impurities may still be present despite considerable purification processes but it has been shown that they can enhance the electrochemical activity of some redox reactions. [131, 132] There are 2 main types of carbon nanotubes: single walled and multi walled.

1.9.1 Single walled carbon nanotubes (SWNT)

SWNT's can be thought of as one sheet of graphene wrapped up into a cylindrical tube (see figure 16. [134])

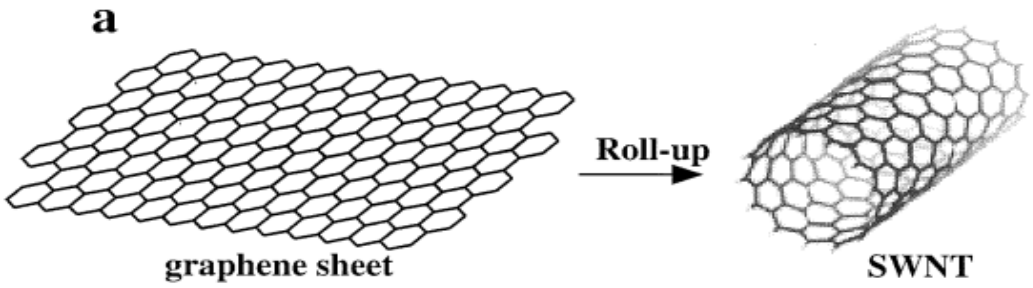

Figure 16 – Schematic diagram of graphene sheet rolled up into a SWNT

They are usually 0.7-3 nm in diameter and microns to tens of microns in length although it is possible to grow SWNT's up to centimetres long. [135] SWNT's with a small diameter have a high Young's modulus and high tensile strength. SWNT's can either be metallic or semiconducting as they are made of graphene – a zero band gap semiconductor that has different conductive properties in different directions. [136] The chirality of the wrap will determine whether the nanotube is metallic or semiconducting with approximately a third possessing metallic properties and two thirds possessing semiconducting properties. Electronic transport in metallic SWNT's occurs ballistically over extended nanotube lengths allowing them to carry high currents with practically no heating. [137, 138]

Typical defects in the surface atoms include sp^3 hybridised sites and the inclusion of 5 or 7-membered rings into the 6-membered ring structure. The surface state is very important when considering the use of carbon nanotubes in electrochemistry – particularly for SWNT's given that they are made up solely of surface atoms. The growth conditions are vitally important, as this is inevitably where impurities arise. Typical impurities are amorphous carbon, metal nanoparticles and charged particles (when post-growth purification is employed).

1.9.2 Multi walled carbon nanotubes (MWNT)

MWNT's can be thought of as a concentric tube of graphene nanotubes rolled up with walls separated by the interlayer area of graphite (0.34nm) – see figure 17. [139]

Figure 17 - A schematic diagram to show a MWNT

Typical diameter range of a MWNT is 2-30nm and they can be grown from microns to tens of microns in length. A MWNT is considered to be metallic if just one of the tubes has metallic character. Electronic transport in metallic MWNT's occurs ballistically over extended nanotube lengths allowing them to carry high currents with practically no heating. [137, 138] MWNT's display surface and sub-surface defects. [140] Voltammetric data would suggest that the sidewalls of MWNT's are chemically inert and that the open end of the nanotube dominates the electrochemistry. [141, 142]

1.10 Highly orientated pyrolytic graphite (HOPG)

HOPG comprises of layers of graphene sheets. It contains terraces and steps with surface and sub surface defects. [143] Voltammetric data suggests that the basal plane of HOPG is inert and that the step edges dominate the electrochemistry. [141, 142]

1.11 The teepee structures

May et al [144] combined the best properties of both carbon nanotubes and diamond to get CVD diamond coated carbon nanotubes. They did this by firstly depositing a dense array of vertically aligned carbon nanotubes onto a silicon substrate, followed by seeding the carbon nanotubes with a nanodiamond suspension in methanol to encourage diamond growth. Following the seeding using the electrospray, they observed that the carbon nanotubes had stuck together causing individual teepee structures to form. The methanol suspension wets the surface of the carbon nanotubes and liquid tension causes several of them to clump together. It is thought that Van der Waals forces keep the teepees together once dry. The samples are then placed in the CVD reactor to grow a thin layer of diamond over the surface. Figure 18 [144] shows SEM images of the teepees.

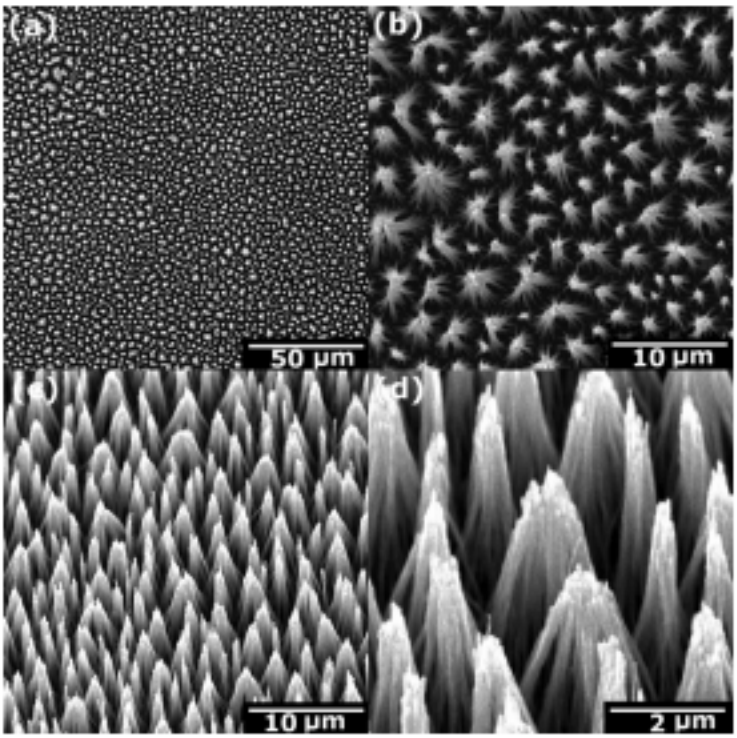

Figure 18 – SEM images of MWNTs after electrospray seeding with a DND methanol suspension. (a) and (b) top views, (c) and (d) images taken with sample tilted at 45°. The DND particles are present on the surface of the CNTs but are too small to be seen at these magnifications.

CVD diamond coated carbon nanotube teepee structures have been proven to be ideal for use in Field Emission. It was found that for diamond coated teepee structures (both undoped-diamond-

coated teepees and B-doped-diamond-coated teepees) there was no need for conditioning before a stable *I-V* curve could be produced whereas several 'conditioning' runs were required for the uncoated carbon nanotube samples. The current density for the teepee structures was also found to be much larger.

When stability tests were performed, the teepees showed a longer lifetime with less flicker and no drop-off in intensity compared to the uncoated carbon nanotube sample which showed ample flicker and nanotube burn out shown by decreased emission current with time.

1.12 Cyclic Voltammetry

Cyclic voltammetry is used to study the electrochemical properties of a redox couple in a 3-electrode system. [145] It works by sweeping the potential of the working electrode between two set potentials while the scan rate is kept constant. Oxidation occurs as the applied potential is increased causing a positive current to flow i.e. electron transfer from the species being oxidised to the electrode. When the set potential is reached the working electrodes potential is inverted and reduction will occur. In reversible systems the electron transfer kinetics must be fast enough so that the oxidation and reduction concentrations are maintained at the values predicted by the Nernst equation. [146] A sigmoidal "duck-shaped" curve is produced for a reversible system. Features of a CV for a reversible system include:

- The peak current ratio $\frac{i_a}{i_c} = 1$
- The peak current is proportional to the square root of the scan rate
- The peak voltage separation $\Delta E = \frac{59}{n}$ mV/s where n is the number of electrons being transferred in the system

The scans produced are symmetrical with the potentials at which peaks occur independent of scan rate.

Typical CV's for boron doped micro-crystalline and nanocrystalline diamond film films can be seen in figure 19. [147]

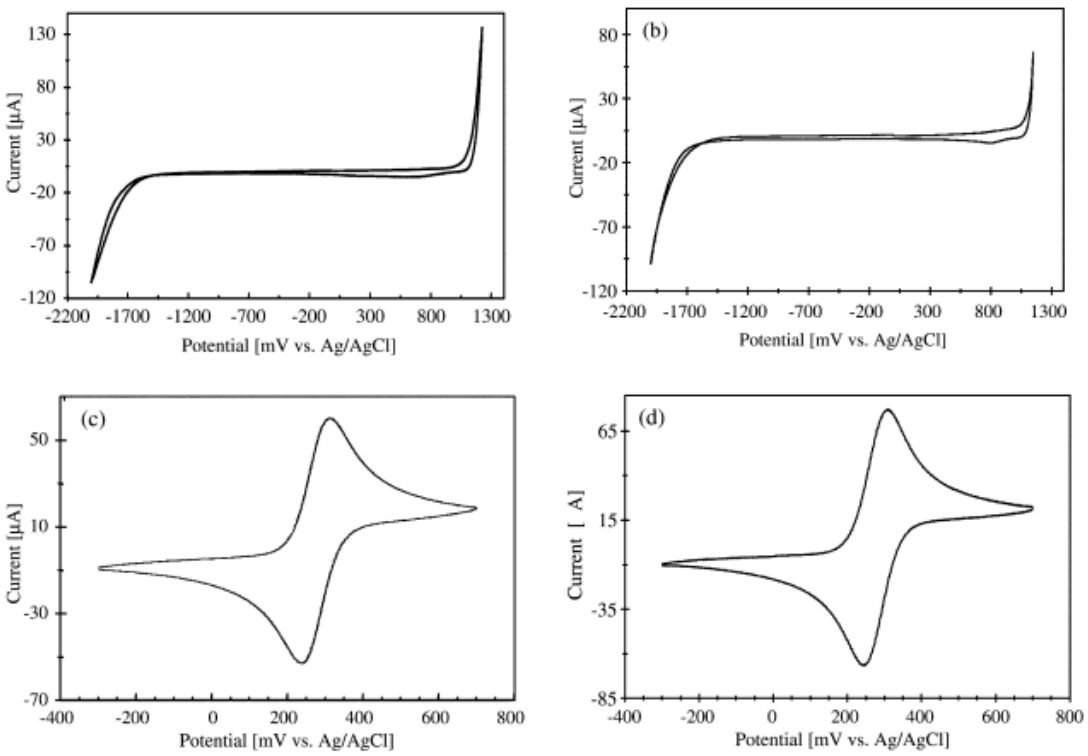

Figure 19 - Cyclic voltammetric *i–E* curves for boron-doped microcrystalline and nanocrystalline diamond thin-films deposited on Si in (a and b) 1 M KCl and (c and d) 1 mM $Fe(CN)_6^{-3/-4}$+1 M KCl. Scan rate=0.1 V/s

If the electron rate transfer constant cannot be maintained, and $\Delta E > \frac{59}{n}$ mV/s with the value of ΔE increasing as the scan rate increases, the process is said to be quasi-reversible. For example, the CV shown in figure 20 [148] shows values of ΔE 68-124 mV/s at a scan rate 10-200 mV/s indicating a quasi-reversible reaction.

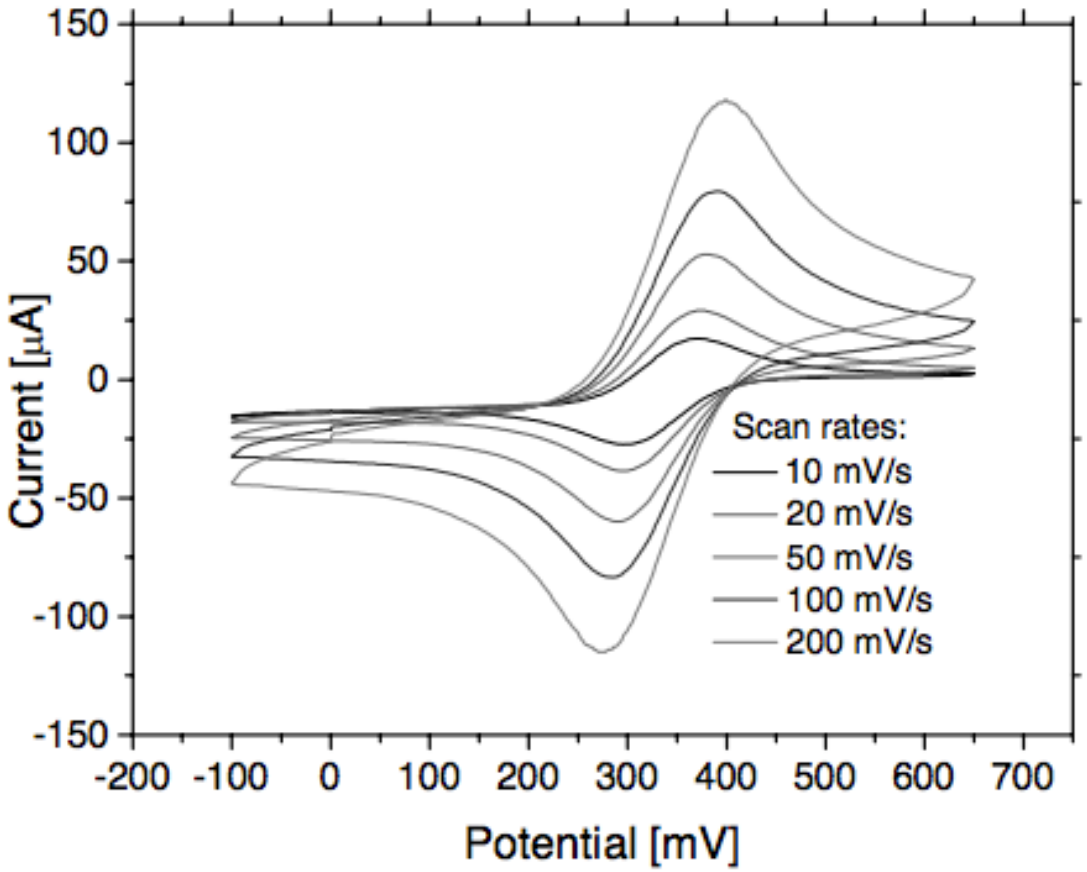

Figure 20 - CV curves at diamond electrode in 0.1 M KCl + 0.01 M $[Fe(CN)_6]^{4-/3-}$

As described in section 1, diamond has a wide potential window in aqueous solution which is why it is particularly interesting in electrochemistry. Figure 21 [149] shows the potential window of diamond compared to other traditional electrode materials. It is clear to see that diamond has a larger potential window than any of the other materials.

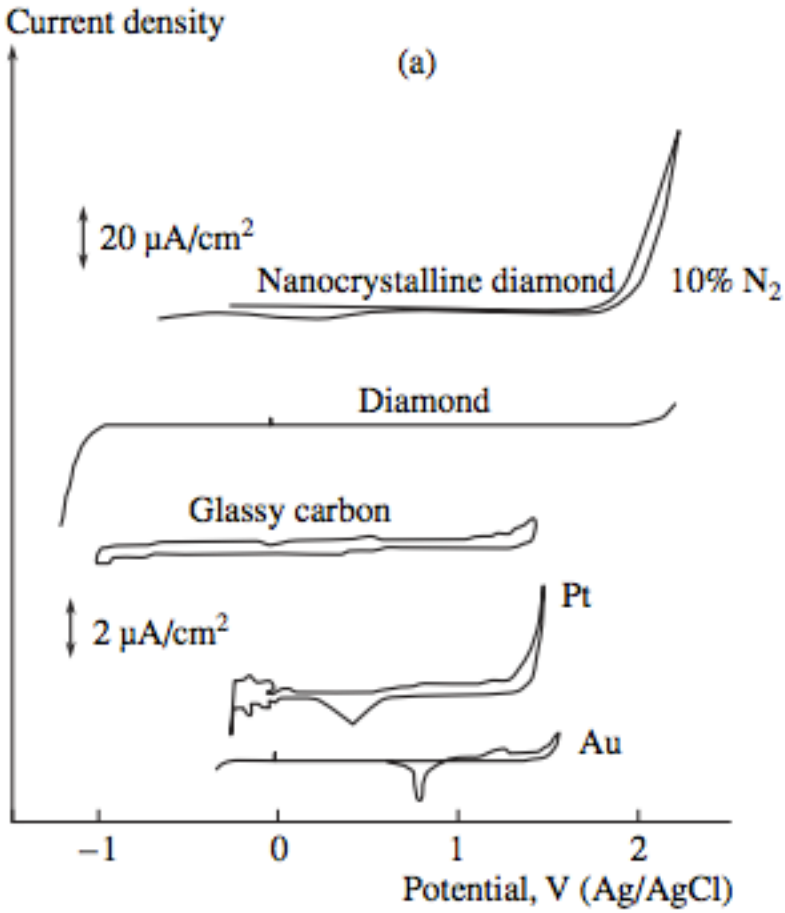

Figure 21 - Cyclic voltammograms showing the potential window for electrodes of diamond compared to traditional materials

1.13 Impedance spectroscopy

Impedance is the opposition that a circuit poses to the passage of a current when a voltage is applied. It can be thought of as resistance with both a magnitude and a phase component. The impedance spectroscopy technique identifies conduction paths within a material allowing a circuit representation to be applied. [150] Experimental data can be compared to a simulation of the data by manipulating the parameters within the circuit.

Ye et al [151] have shown that the grain boundary effects dominate electrical conduction in a wide range of microcrystalline diamond films. They have also shown that both grain boundary and grain interior conduction exist within silicon supported nanocrystalline diamond films. [170]

1.14 Conclusion

Diamond is a remarkable material with many physical properties that make it ideal for use in electrochemistry. Properties of diamond that are of particular interest include a good voltammetric response, chemically inert and a negative electron affinity. Carbon nanotubes also have features that make them ideal for use in electrochemistry such as strength, a high aspect ratio, they can pass high currents, and they show low threshold voltages. Combining the best features of both materials to give boron doped diamond carbon nanotube teepees should give an excellent electrode material with surface areas significantly larger than flat electrodes.

2. Experimental

2.1 Electrospray

Two lots of samples A and B were obtained from Sara M.C Vieira IESC-MN Lisbon, Portugal. Both consisted of a silicon substrate with a dense array of multi walled carbon nanotubes (CNT's) on the surface. Sample A had CNT's of length 5 microns and sample B had CNT's of length 10-15 microns.

Four samples in total – two of each A and B – were loaded onto the metallic substrate mount as seen in figure 22.

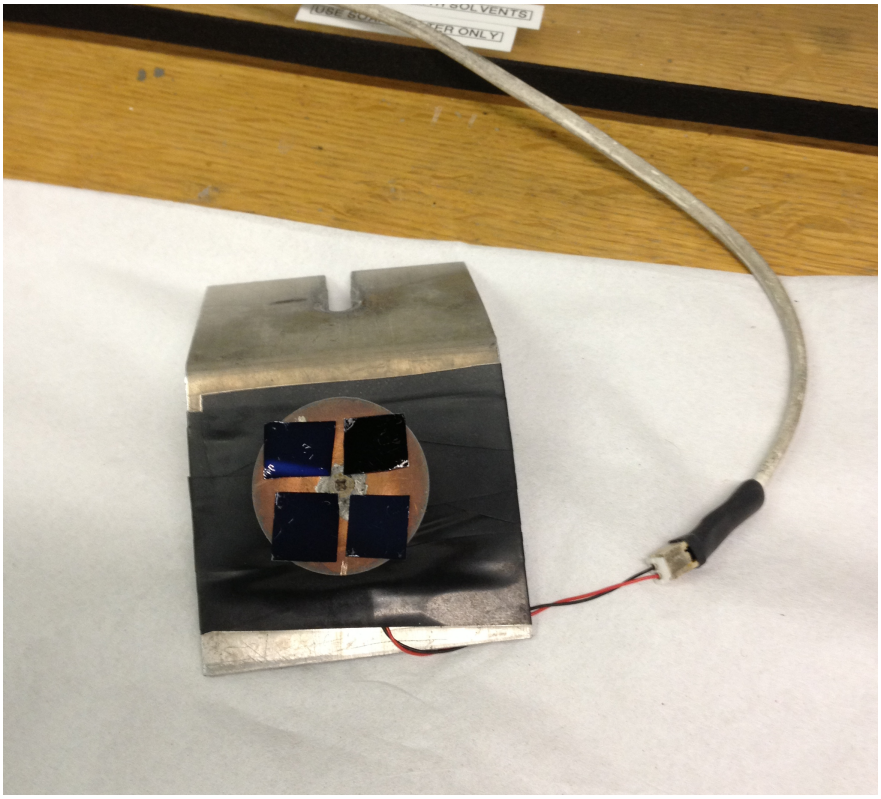

Figure 22 – A photograph to show four samples, two A and two B, loaded onto the metallic substrate mount.

A 1ml suspension of 5 nm diamond in methanol [152] was loaded into the syringe on the outside of an insulating box and the syringe and substrate mount were adjusted to ensure they were correctly aligned as seen in figure 23. [153] Figure 24 shows a photograph of the apparatus.

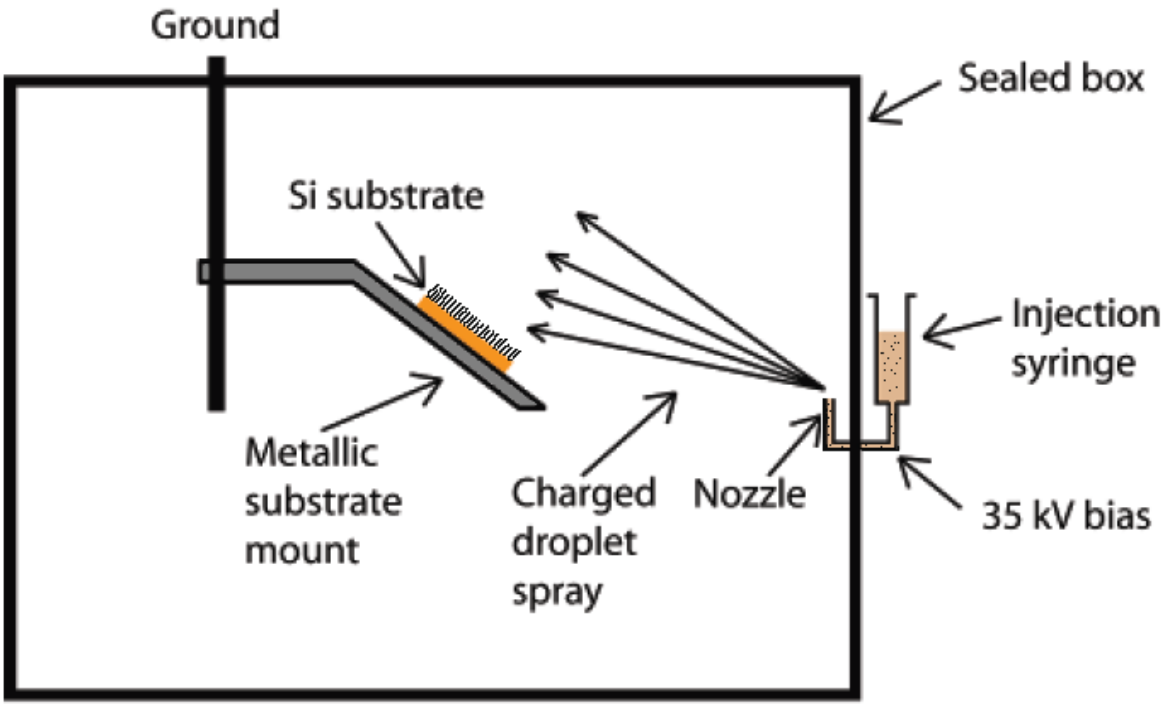

Figure 23 – A schematic diagram showing the electrospray apparatus.

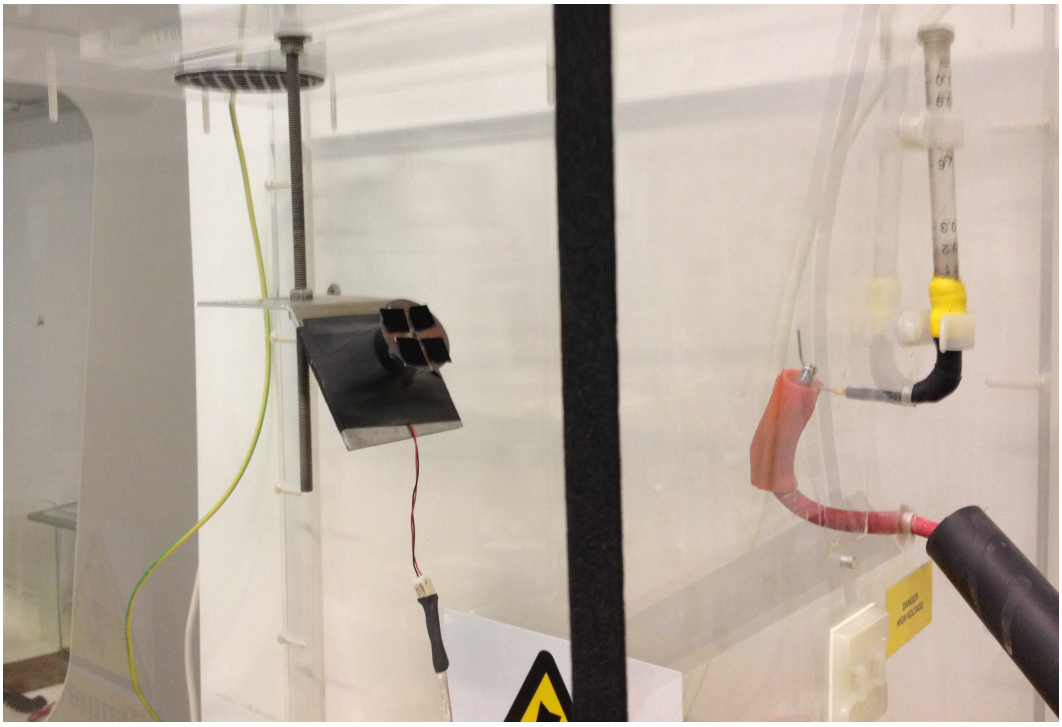

Figure 24 – A photograph to show the electrospray apparatus.

A potential difference of 32,500 V was applied to ionize the nanodiamond suspension and accelerate the nanodiamond particles towards a grounded substrate. The substrate mount was set to rotate at a high speed to ensure a uniform covering of the samples. It took 4-5 minutes for most of the suspension to be drained. There was a small amount of the suspension left which was put down to a blockage in the syringe.

When the samples were checked under a microscope it was found that there was not a homogenous covering of nanodiamond over the all of the CNT samples. This was also put down to the blockage in the syringe and the concentration of nanodiamond in methanol being too low.

This process was repeated with four further samples – all four sample B. This time the syringe was thoroughly cleaned using an ultrasonic cleaning bath and a 1.5 ml (as opposed to 1 ml) nanodiamond in methanol suspension of a higher concentration was used.

All samples were checked under the microscope to ensure an even coverage of nanodiamond forming the teepees.

2.2 CVD reactor

Once seeded with a nanodiamond thin layer, chemical vapour deposition (CVD) technique was used to grow a boron doped polycrystalline diamond thin film over each sample. Figure 25 shows two samples about to go into the reactor.

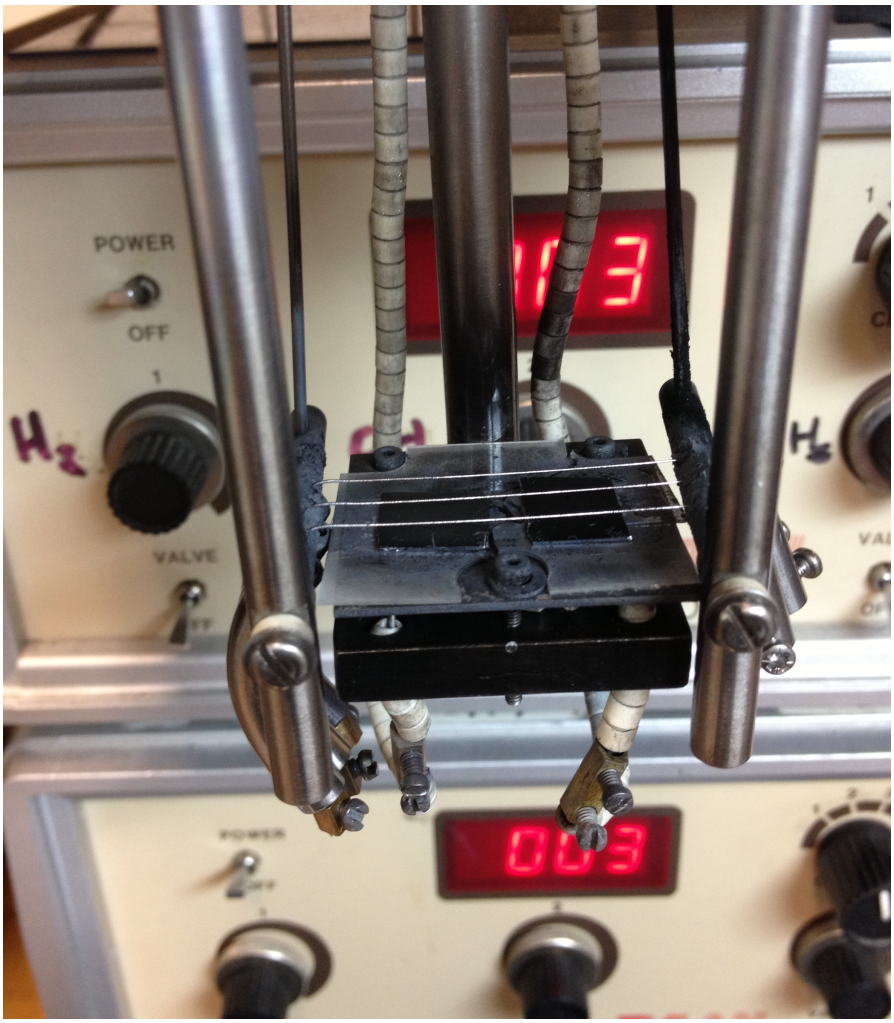

Figure 25 – A photograph to show two samples ready to go into the CVD reactor.

Conditions such as boron doping level and diamond crystallite morphology were varied to get a range of samples.

Samples:

1 – Residually doped micro-crystalline teepee sample A

2 – Residually doped micro-crystalline teepee sample B

3 – Highly doped micro-crystalline teepee sample A

4 – Highly doped micro-crystalline teepee sample B

5 – Highly doped nano-crystalline teepee sample B

6 – Undoped silicon flat sample (no CNT's) –uniform coating

7 – Oxygen terminated flat sample (Obtained from Element Six Ltd, oxygen terminated by the ozone cleaner)

8 – Hydrogen terminated flat sample (Obtained from Element Six Ltd, hydrogen terminated in a H plasma in the MW reactor)

Table 2 describes the different CVD growth conditions used to obtain the samples.

Sample	**Pressure (torr)**	**Time in reactor (hours)**	**H_2 (sccm)**	**CH_4 (sccm)**	**B_2H_6 (sccm)**	**SEM images**	**CV's**
1	20	1	200	2	0	A 13	Fig 37, A 1
2	20	1	200	2	0	A 14	Fig 36, A 2
3	20	1.5	200	20	35	A 15-17	Fig 39, fig 34
4	20	1.5	200	20	35	A 18–23	Fig 38, fig 32
5	20	1.5	200	50	35	A 24-26	Fig 30, A 3
6	20	7	200	2	35	-	Fig 37, A 5

Table 2 – A table to describe the growth conditions used to obtain each sample and the figures describing their appropriate SEM images and CV's.

2.3 Scanning Electron Microscopy (SEM)

SEM images were taken of all the samples made using both the normal and the high-resolution (Field Emission Gun) SEM machines. Figure 26 shows an example of an SEM image taken of sample 4 using the normal resolution SEM machine.

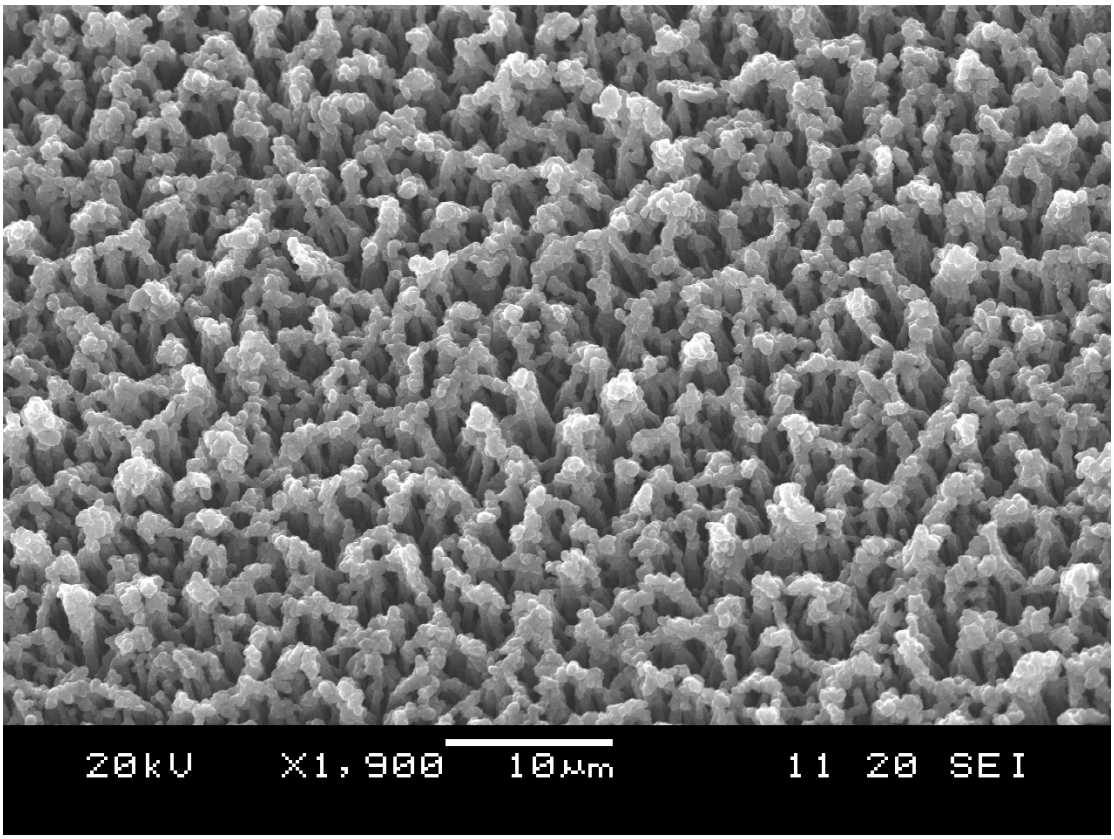

Figure 26 – An SEM image taken using the normal resolution SEM of sample 4.

2.4 Making the electrodes

There were 2 parts involved in making the samples into electrodes such as that seen in figure 27. The first part involved attaching a piece of conductive copper wire to the side of the sample covered in BDD CNT teepee structures. This was done with conductive silver paint also known as silver dag. The copper wire was sanded on both ends to get rid of any copper that had oxidised on the surface. The end of the copper wire was approximately a third of the way up the sample. Care was taken while handling the samples and while painting on the silver dag as the CNT's could easily be squashed. It was important to ensure the silver dag was completely dry by leaving the samples for at least half an hour.

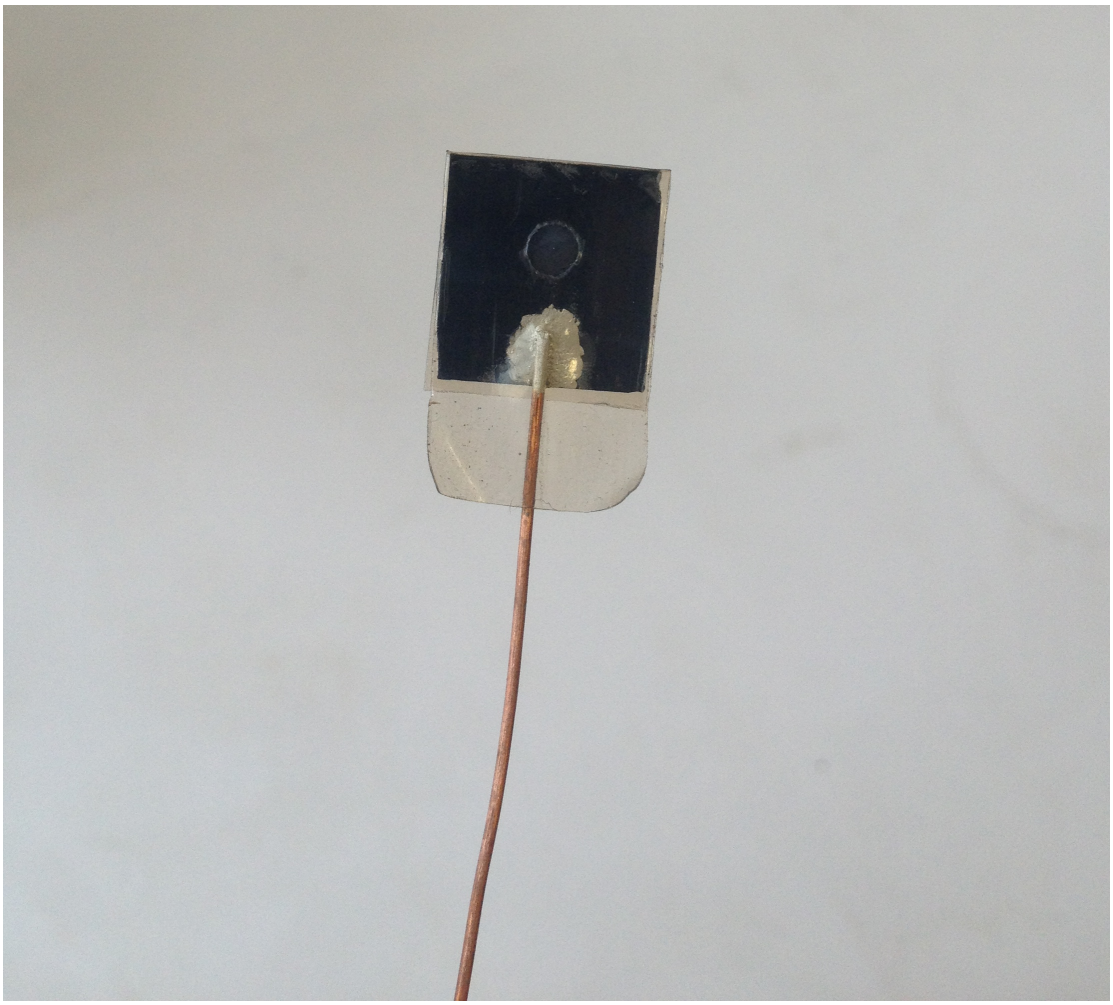

Figure 27 – A photograph to show an electrode made from a BDD CNT sample, conductive copper wire connected with silver dag and Teflon tape.

Once the copper wire was connected to the sample, a piece of Teflon tape containing a hole of diameter 0.3 cm was carefully placed over the sample. If the sample didn't have a completely homogeneous layer of CVD diamond (i.e. if a corner of the sample slipped from under the filaments) care was taken to place the hole over an area that showed good coverage.

2.5 Cyclic voltammetry

Cyclic voltammetry was performed using an Autolab potentiostat on all electrodes using both a ferro/ferri cyanide and KCl system. GPES software was used. Solutions for both electrolytes were made up as follows:

2.5.1 Ferri/ferro cyanide

A 100 ml solution of 1×10^{-3} mol dm^{-3} ferri/ferro cyanide was made up from 0.5×10^{-3} mol dm^{-3} $K_4[Fe(CN)_6].3H_2O$ and 0.5×10^{-3} mol dm^{-3} $K_3[Fe(CN)_6]$.

Ferri cyanide - $K_3[Fe(CN)_6]$

Mr = 329.24 g/mol

No of moles = 0.5×10^{-3} mol dm^{-3}

Mass (g/dm^{-3}) = Mr (g/mol) × no of moles (mol dm^{-3})

Mass (g/dm^{-3}) = 329.24 g/mol × 0.5×10^{-3} mol dm^{-3}

Mass = 164.62×10^{-3} g/dm^{-3} = 0.165 g/100ml

Ferro cyanide - $K_4[Fe(CN)_6].3H_2O$

Mr = 422.39 g/mol

No of moles = 0.5×10^{-3} mol dm^{-3}

Mass (g/dm^{-3}) = Mr (g/mol) × no of moles (mol dm^{-3})

Mass (g/dm^{-3}) = 422.39 g/mol × 0.5×10^{-3} mol dm^{-3}

Mass = 211.195×10^{-3} g/dm^{-3} = 0.021 g/100ml

2.5.2 Potassium chloride (KCl)

A 100ml solution of 0.1 mol dm^{-3} KCl was made up.

Mr = 74.551 g/mol

No of moles = 0.1×10^{-3} mol dm^{-3}

Mass (g/dm^{-3}) = Mr (g/mol) × no of moles (mol dm^{-3})

Mass (g/dm^{-3}) = 74.551 g/mol × 0.1×10^{-3} mol dm^{-3}

Mass = 7.455×10^{-3} g/dm^{-3} = 0.746 g/100ml

2.5.3 The electrochemical cell

The electrochemical cell was set up as shown in figure 28 using 50ml of solution with an Ag/Cl reference electrode (blue), a Pt counter electrode (black) and a diamond working electrode (red). Argon gas was bubbled through the solution for 20 minutes at the beginning of the session and for 5 minutes following each change of working electrode.

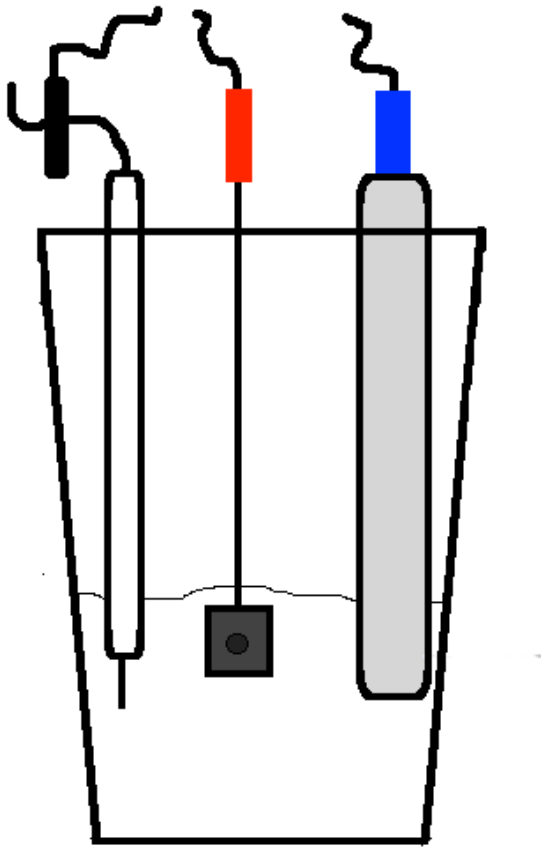

Figure 28 – A schematic diagram to show the set up of the electrochemical cell. The Pt counter electrode is black, the Ag/Cl reference electrode is blue, and the diamond working electrode is red.

2.5.4 CV readings

Readings were taken at the following scan rates for each electrode:

10 mV/s
25 mV/s
50 mV/s
75 mV/s
100 mV/s

Readings were taken between potentials ranging from -0.1 V – 0.5 V and -0.1 V – 0.7 V.

2.6 Impedance

Impedance measurements were taken for each electrode using an Autolab potentiostat using the same electrochemical cell set up as described in section 5.3 using in the KCl solution described in section 5.2. Measurements were taken at a potential of 0V. The circuit RQ was simulated and fit to each set of data where R corresponds to the resistance of the electrolyte back contact and Q corresponds to the double layer capacitor. Using the data and best fit shown in the bode plot, the values of R and Q were adjusted to get the best fitting line and the value of n that is closest to 1 where anything between 0.9 and 1 is satisfactory.

3. Results and discussion

The aim of this experiment has been to determine whether CVD diamond coated carbon nanotube teepee structures work as electrodes in electrochemistry and to assess how they differ to flat electrodes. Cyclic voltammetry was used to establish their electrochemical behaviour. The ferri/ferro cyanide system was used to determine the reversibility of the reaction and the KCl system was used to determine to what extent the electrode exhibits capacitive or resistive behaviour. The difference in the surface area between a flat electrode and teepee electrodes is to be established. Capacitance measurements taken from impedance data allows for the calculation of the surface areas of the samples.

3.1 Cyclic Voltammetry

3.1.1 Ferri/ferro cyanide

A ferri/ferro cyanide system was used as it is a well understood, reversible, one electron transfer system. Figure 29 [154] gives an example of perfectly reversible sigmoidal curves using a BDD hydrogen terminated electrode.

Features that indicate a fully reversible system are:

- The ratio of peak currents is equal to 1
- The peak currents are proportional to the square root of the scan rate
- The peak voltage separation is equal to $\frac{59}{n}$ mV where n is equal to 1 in the case of ferri/ferro cyanide as it is a one electron system.

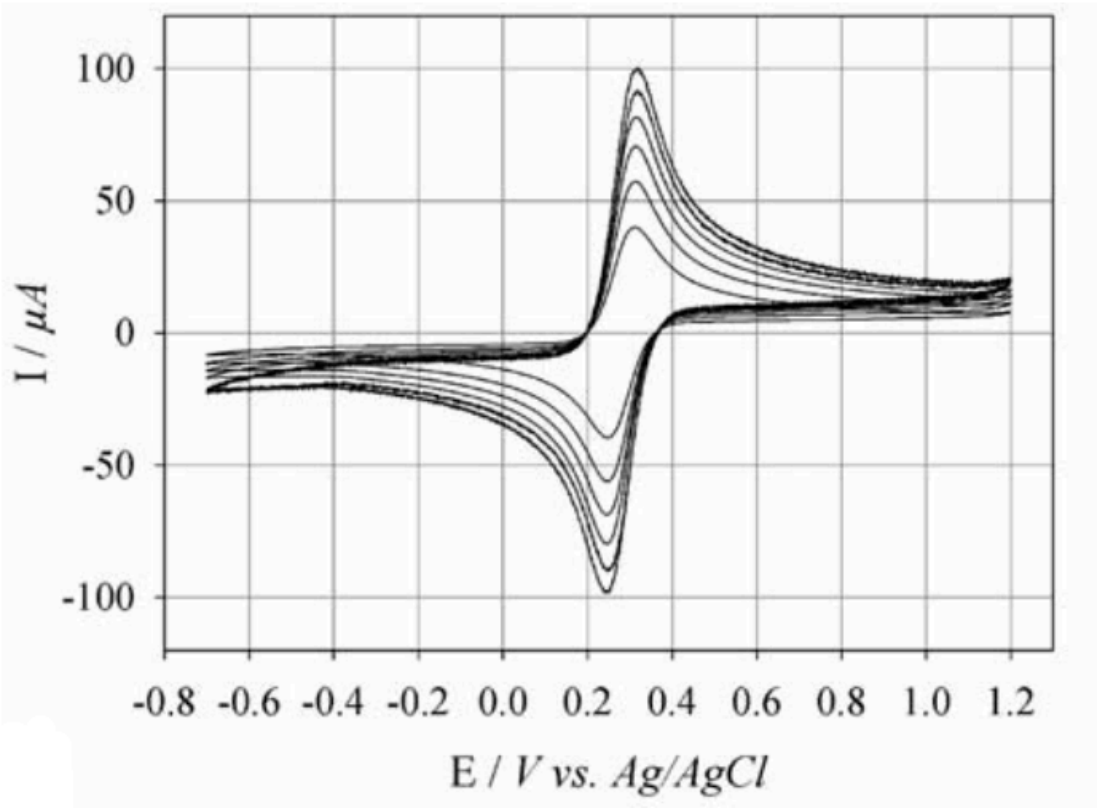

Figure 29 – A cyclic voltammogram using 1 mM $Fe(CN_6)^{-3/-4}$ in 1 M KCl using a BDD H terminated electrode. Scan rates 100 – 600 mV/s .

3.1.1.1 Electrode 5 - Highly doped nano-crystalline diamond teepee sample B electrode

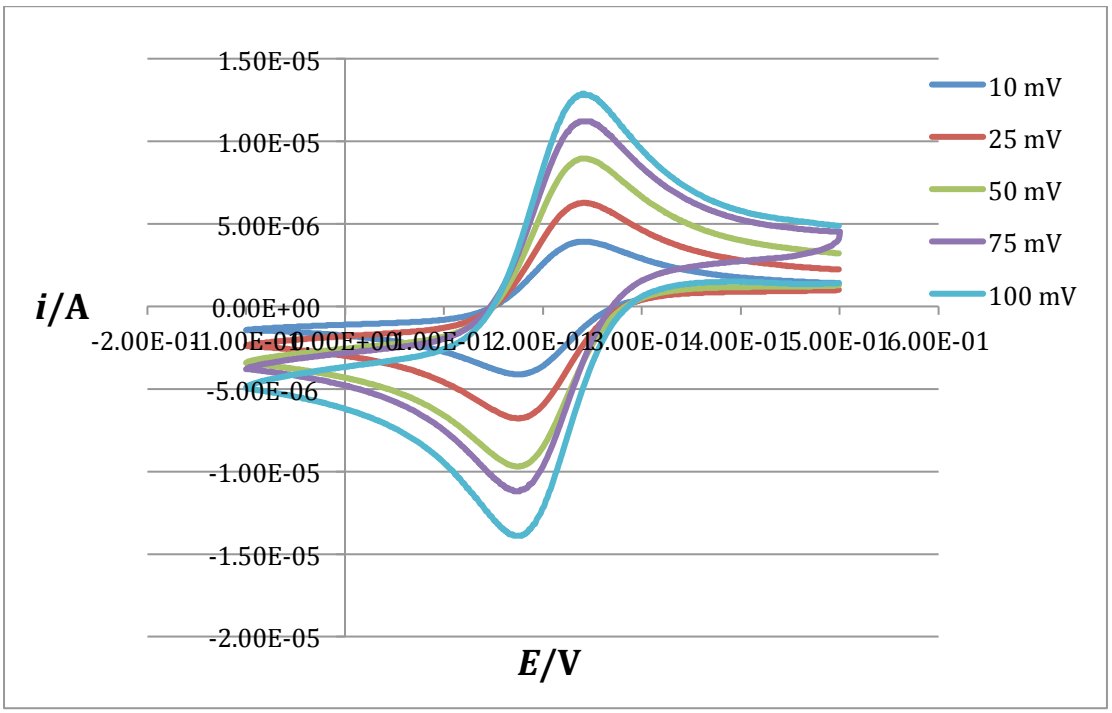

Figure 30 - A cyclic voltammogram using 1 mM $Fe(CN_6)^{-3/-4}$ on electrode 5. Start potential -0.1 V, first potential 0.5 V. Scan rates 10 mV/s, 25 mV/s, 50 mV/s, 75 mV/s, 100 mV/s.

Figure 30 shows CV *i-E* curves for 1mM $Fe(CN_6)^{-3/-4}$ using the highly doped nano-crystalline diamond sample B electrode. The graph shown in figure 30 is symmetrical and a sigmoidal shape as you would expect from a perfectly reversible system. The position of peak voltage does not alter with scan rate with the average value of the maximum peak (or the cathodic peak, E_{pc}) for each scan rate equal to 0.24 V, and the average value of the minimum peak (or anodic peak E_{pa}) for each scan rate equal to 0.18 V.

The peak voltage separation at v = 100 mV/s:

Eq (1) $\Delta E = E_{pc} - E_{pa} = 0.24\text{ V} - 0.18\text{ V} = 0.6\text{ V} = 60\text{ mV}$

This value of 60 mV calculated in equation 1 is very close to 59mV, the ideal peak voltage separation expected for a perfectly reversible system. Peak voltage separation has been calculated for all scan rates and the value of ΔE is consistently 60 mV showing that peak voltage separation

does not alter as a function of scan rate. This value reflects relatively rapid electrode-reaction kinetics. [155]

The peak current ratio should be equal to 1 at all scan rates for a perfectly reversible system. Peak current ratios for each scan rate are given as follows:

10mV/s

Eq (2) Peak current ratio = $\frac{I_{pa}}{I_{pc}} = \frac{4.11 \times 10^{-6}}{3.93 \times 10^{-6}} = 1.05$

25 mV/s

Eq (3) Peak current ratio = $\frac{I_{pa}}{I_{pc}} = \frac{6.78 \times 10^{-6}}{6.25 \times 10^{-6}} = 1.09$

50 mV/s

Eq (4) Peak current ratio = $\frac{I_{pa}}{I_{pc}} = \frac{1.11 \times 10^{-5}}{8.94 \times 10^{-6}} = 1.24$

75 mV/s

Eq (5) Peak current ratio = $\frac{I_{pa}}{I_{pc}} = \frac{1.10 \times 10^{-5}}{1.22 \times 10^{-5}} = 0.90$

100 mV/s

Eq (6) Peak current ratio = $\frac{I_{pa}}{I_{pc}} = \frac{1.38 \times 10^{-5}}{1.28 \times 10^{-5}} = 1.08$

The peak current ratios calculated in equations 3, 3, 5 and 6 are within 10% of 1 - the peak current ratio value expected for a perfectly reversible system. The value given in equation 4, corresponding to a scan rate of 50 mV/s is within 25% of the expected value for a completely reversible system.

A plot of the square root of the scan rate versus the peak current gives the current function which is a linear graph as seen in figure 31 when reversible electron transfer is observed.

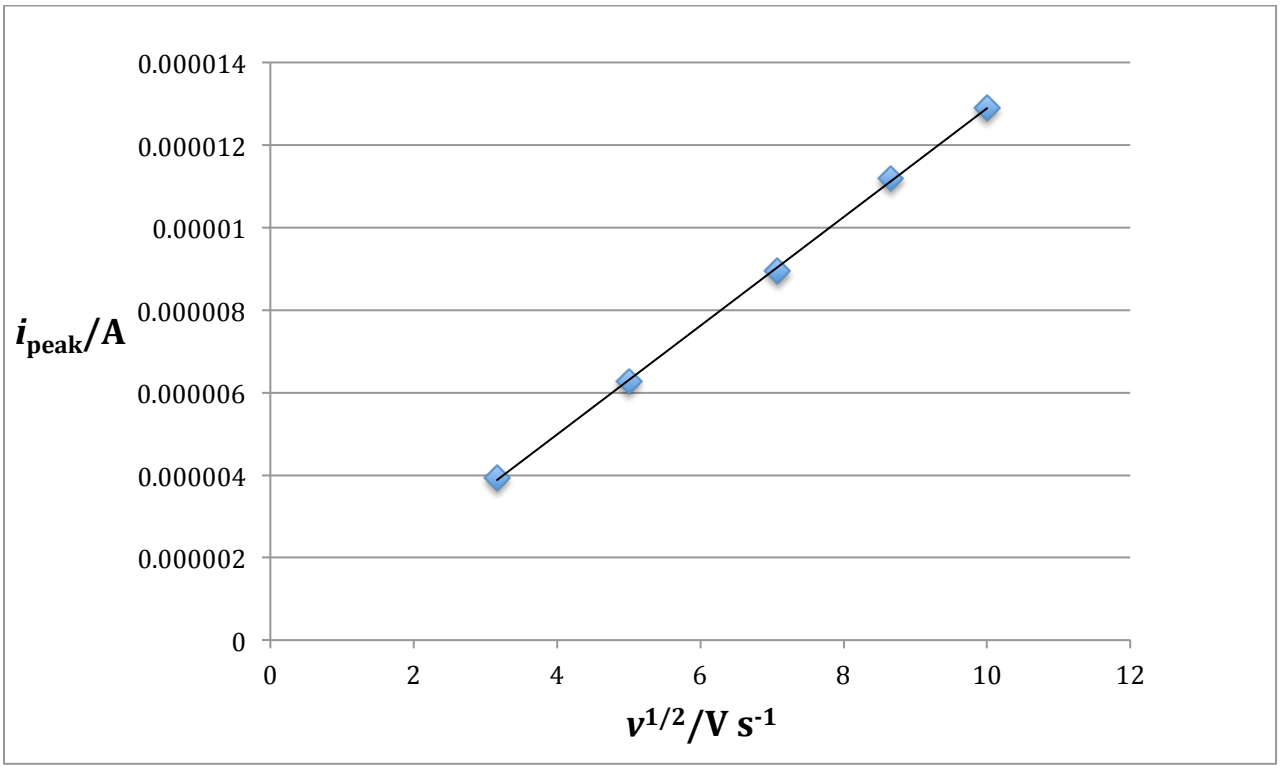

Figure 31 – A graph showing peak current vs square root of scan rate for electrode 5.

The linear plot in figure 31 proves the presence of a completely reversible reaction that is diffusion controlled in which the electron transfer kinetics are fast enough to maintain the equilibrium between the redox couple as predicted by the Nernst equation. [146]

The diffusion coefficient, *D*, can be calculated from the Randles-Sevick equation:

Eq (7) $i_{peak} = 2.69 \times 10^5 \, n^{3/2} \, A \, D^{1/2} \, c \, v^{1/2}$

Where:

i_{peak} = peak current in Amps = 1.29×10^{-5} A

n = number of e$^-$s transferred in the redox reaction = 1

A = area of the electrode in cm^2 = 0.071 cm^2

D = diffusion coefficient in cm^2 s^{-1}

c = concentration in mol cm^{-3} = 1×10^{-6} mol cm^{-3}

v = scan rate in V s^{-1} = 100 mV s^{-1} = 0.1 V s^{-1}

Rearranging equation (7) to get the unknown variable D on the LHS gives equation (8):

Eq (8) $$D^{1/2} = \frac{i\text{peak}}{2.69 \times 105\ n3/2\ A\ i\text{peak}\ c\ v1/2}$$

$$D^{1/2} = \frac{1.29 \times 10{-}5}{2.69 \times 105 \times 1 \times 0.071 \times 1 \times 10{-}6 \times 0.11/2}$$

$$D^{1/2} = 2.14 \times 10^{-3}\ \text{cm}^2\ \text{s}^{-1}$$

Therefore the diffusion coefficient D is given in equation (9):

Eq (9) $$D = (2.14 \times 10^{-3})^{2}$$

$$D = 4.56 \times 10^{-6}\ \text{cm}^2\ \text{s}^{-1}$$

A value of 6.4×10^{-6} cm^2 s^{-1} for the diffusion coefficient of ferricyanide at concentration 1 mM has been reported in the literature. [156] For ferrocyanide at a concentration of 1mM, a diffusion coefficient value of 6.67×10^{-6} cm^2 s^{-1} has been reported. [160] Given that the value of the diffusion coefficient determined in equation (9) is also of the same order of magnitude as both of the above values, it can be considered an accurate result.

3.1.1.2 Electrode 4 – Highly doped microcrystalline diamond teepee sample B electrode.

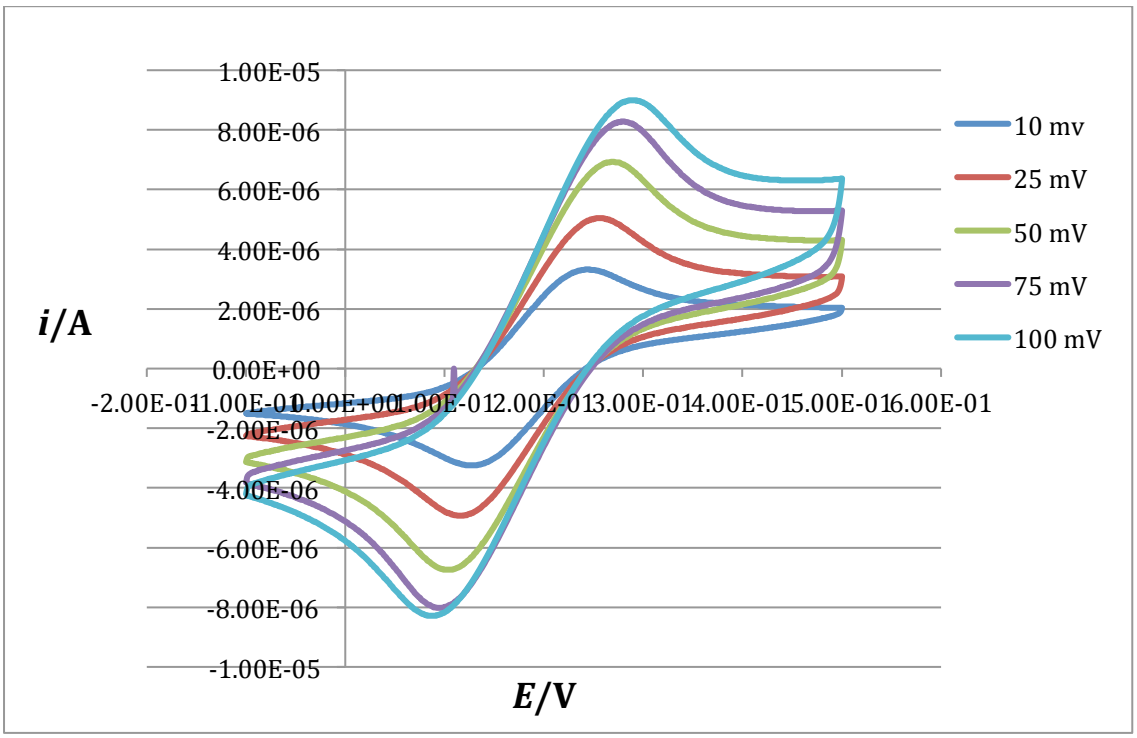

Figure 32 - A cyclic voltammogram using 1mM $Fe(CN_6)^{-3/-4}$ on electrode 4. Start potential -0.1 V, first potential 0.5 V. Scan rates 10 mV/s, 25 mV/s, 50 mV/s, 75 mV/s, 100mV/s.

Figure 32 shows CV *i-E* curves for 1mM $Fe(CN_6)^{-3/-4}$ using the highly doped microcrystalline diamond sample B electrode. The curves shown in figure 32 are nearly symmetrical and sigmoidal in shape but in comparison to the curves shown in figure 30, the graph is slightly shifted showing that the peak voltage alters slightly with scan rate. The potential value for the maximum peak, E_{pc} taken at scan rate 100 mV/s is equal to 0.29 V. The potential value for the minimum peak, E_{pa} taken at scan rate 100 mV/s is equal to 0.09 V.

The peak voltage separation at v = 100mV/s:

Eq (1) $\Delta E = E_{pc} - E_{pa} = 0.29\ V - 0.09\ V = 0.2\ V = 200\ mV$

The value of peak voltage separation calculated in equation 1 is much greater than the expected 59 mV for a reversible reaction. This is indicative of a quasi-reversible reaction. Features indicating a quasi-reversible reaction are:

- Values of $\Delta E > 59$ mV
- Peak voltage separation ΔE is increasing with higher scan rates.
- Rate of electron transfer is decreasing with increased scan rate as the curves are shifting to more reductive potentials.
- Peak current no longer varies as a function of $v^{1/2}$

It is clear to see from the graph in figure 32 that the value of ΔE increases with higher scan rates. The rate constant for electron transfer is decreasing with increased scan rate as the equilibrium (of the redox reaction) as predicted by the Nernst [146] equation is not being established fast enough. If a plot of peak current vs square root of scan rate were to be plotted as in figure 31, a linear graph would not be obtained.

3.1.1.3 Electrode 6 – Undoped silicon flat sample (no CNT's) –uniform coating

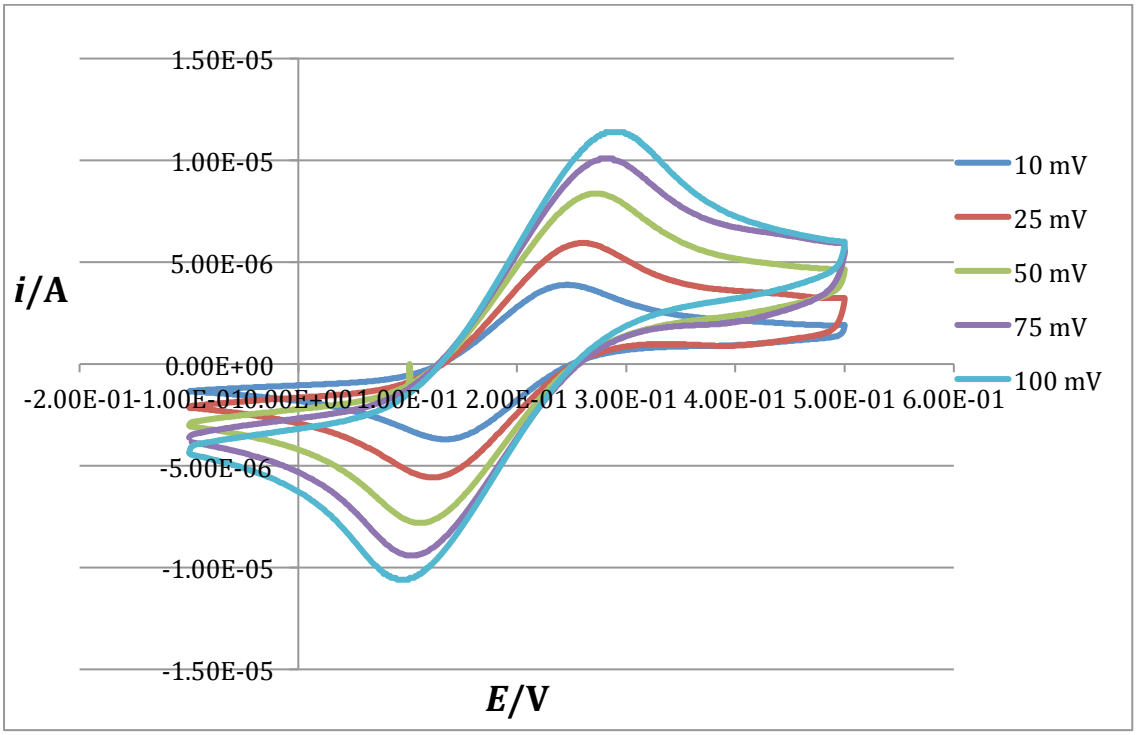

Figure 33 - A cyclic voltammogram using 1mM $Fe(CN_6)^{-3/-4}$ on electrode 6. Start potential -0.1 V, first potential 0.5 V. Scan rates 10 mV/s, 25 mV/s, 50 mV/s, 75 mV/s, 100mV/s.

Figure 33 shows CV *i-E* curves for 1mM $Fe(CN_6)^{-3/-4}$ using the undoped silicon flat sample electrode. The curves shown in figure 33 are beginning to lose the classic sigmoidal shape expected from the

$Fe(CN_6)^{-3/-4}$ system. The position of peak voltage is shifting with higher scan rate which is typical of quasi-reversible behaviour. At higher voltages the curves start to overlap in an illogical fashion. Although peak voltages are distinguishable, it is clear by looking at the graph in figure 33 that the peak voltage separation is much greater than 59 mV/s. The peak current does not vary with the square root of the scan rate. The graph in figure 33 is indicative of quasi-reversible behaviour.

3.1.1.4 Electrode 8 – Hydrogen terminated diamond surface.

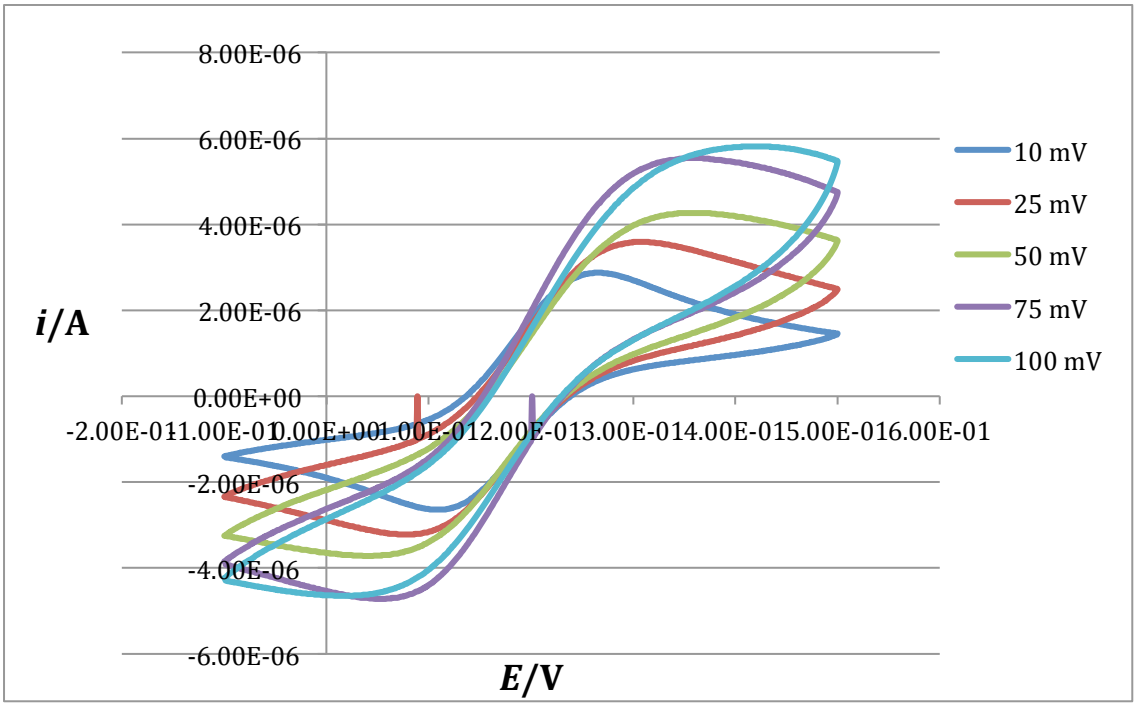

Figure 34- A cyclic voltammogram using 1mM $Fe(CN_6)^{-3/-4}$ on electrode 8. Start potential -0.1 V, first potential 0.5 V. Scan rates 10 mV/s, 25 mV/s, 50 mV/s, 75 mV/s, 100mV/s.

Figure 34 shows CV *i-E* curves for 1mM $Fe(CN_6)^{-3/-4}$ using the hydrogen terminated diamond surface electrode. The curves shown in figure 34 are losing the classic sigmoidal shape compared to the curves shown in figure 30. The position of peak voltage is shifting to higher potentials as a function of scan rate. The peak voltage value for the 75 mV/s scan rate is an anomaly and does not follow this trend. From the graph, both maximum and minimum voltage peaks can be distinguished although it is clear to see by eye that the peak voltage separation is much greater than 59 mV/s. The peak current does not vary with the square root of the scan rate. The graph shown in figure 34 shows quasi-reversible behaviour.

3.1.1.5 Electrode 3 - Highly doped micro-crystalline teepee sample A

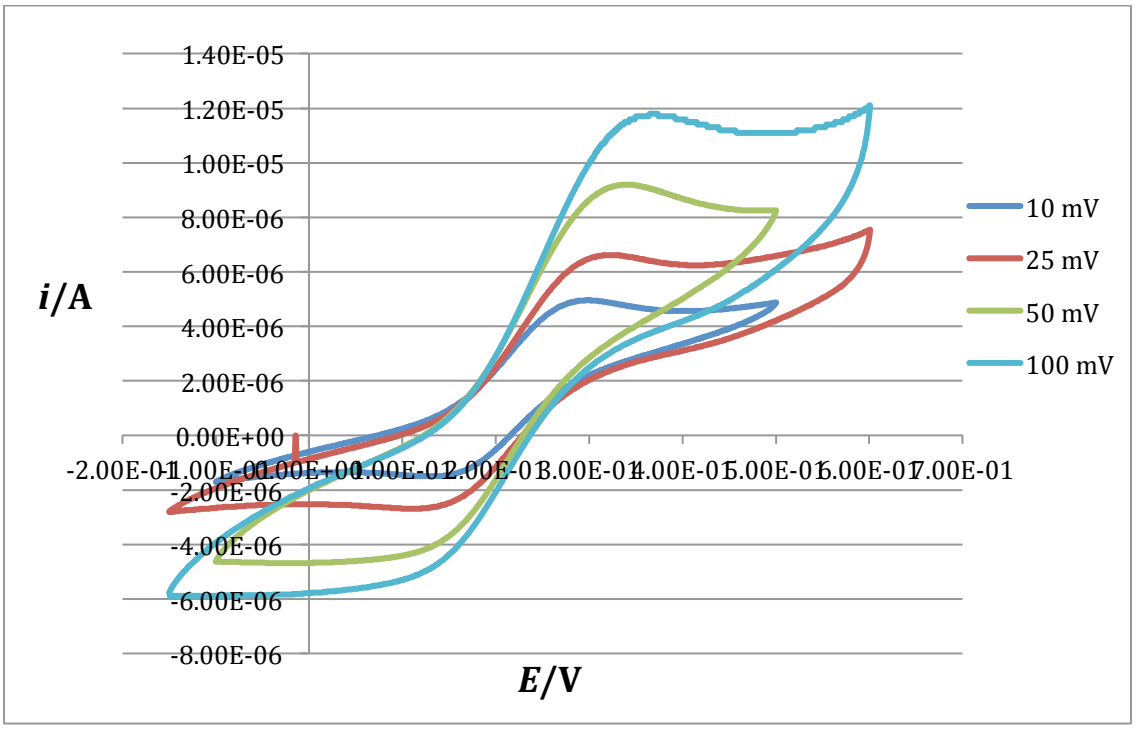

Figure 35 - A cyclic voltammogram using 1mM $Fe(CN_6)^{-3/-4}$ on electrode 3. Scan rates 10 mV/s, 25 mV/s, 50 mV/s, 75 mV/s, 100mV/s.

Figure 35 shows CV *i-E* curves for 1mM $Fe(CN_6)^{-3/-4}$ using the highly doped microcrystalline diamond sample A electrode. The curves shown in figure 35 have some characteristics of symmetry but are not completely symmetrical. Compared to the classic sigmoidal shape shown in figure 30, these curves in figure 35 have almost completely lost that characteristic shape as there is no longer a back peak as such. When the peak voltage measurement was attempted, it was proven to be impossible as there is no back peak, just a steady slope to the minimum current value.

3.1.1.6 Electrode 7 - Oxygen terminated flat sample

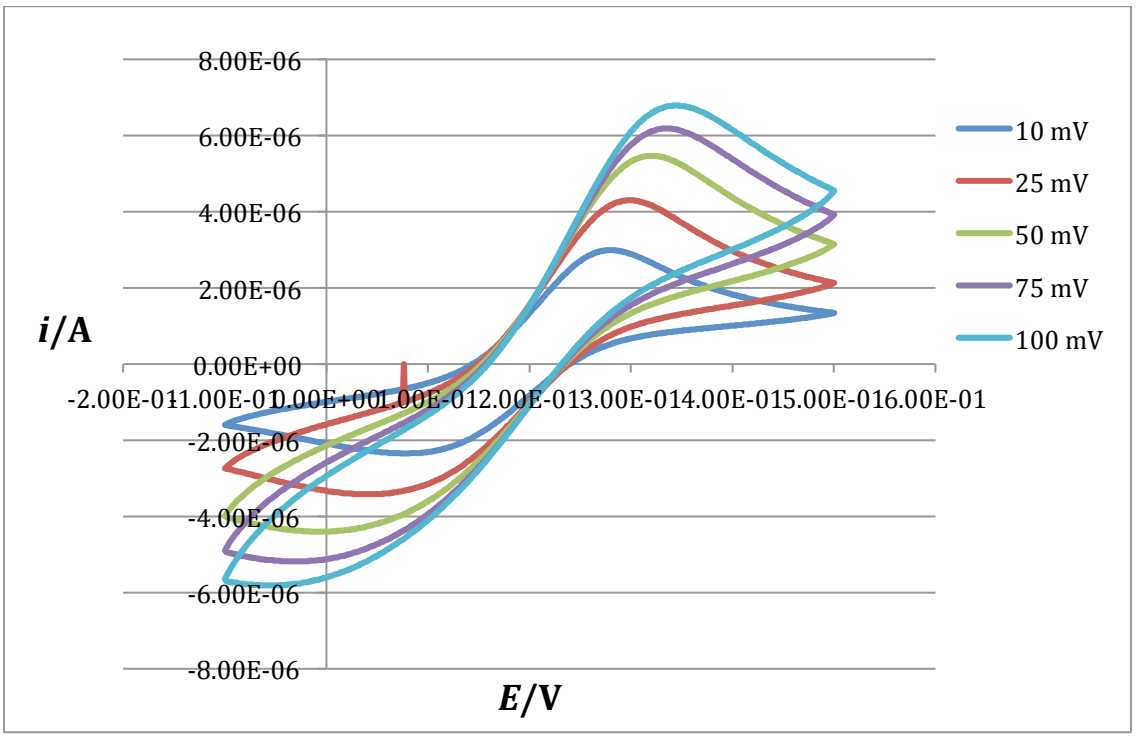

Figure 36 - A cyclic voltammogram using 1mM $Fe(CN_6)^{-3/-4}$ on electrode 7. Start potential -0.1 V, first potential 0.5 V. Scan rates 10 mV/s, 25 mV/s, 50 mV/s, 75 mV/s, 100mV/s.

Figure 36 shows CV *i-E* curves for 1mM $Fe(CN_6)^{-3/-4}$ using the oxygen terminated flat electrode. As with the curves shown in figure 34, those shown in figure 36 show little symmetry and few characteristics of a sigmoidal shape as there is no presence of a back peak. As no back peak exists, it is impossible to measure the peak voltage separation as the graphs steadily tail off to a minimum current.

3.1.1.7 Electrode 2 – Residually doped microcrystalline diamond teepee sample B

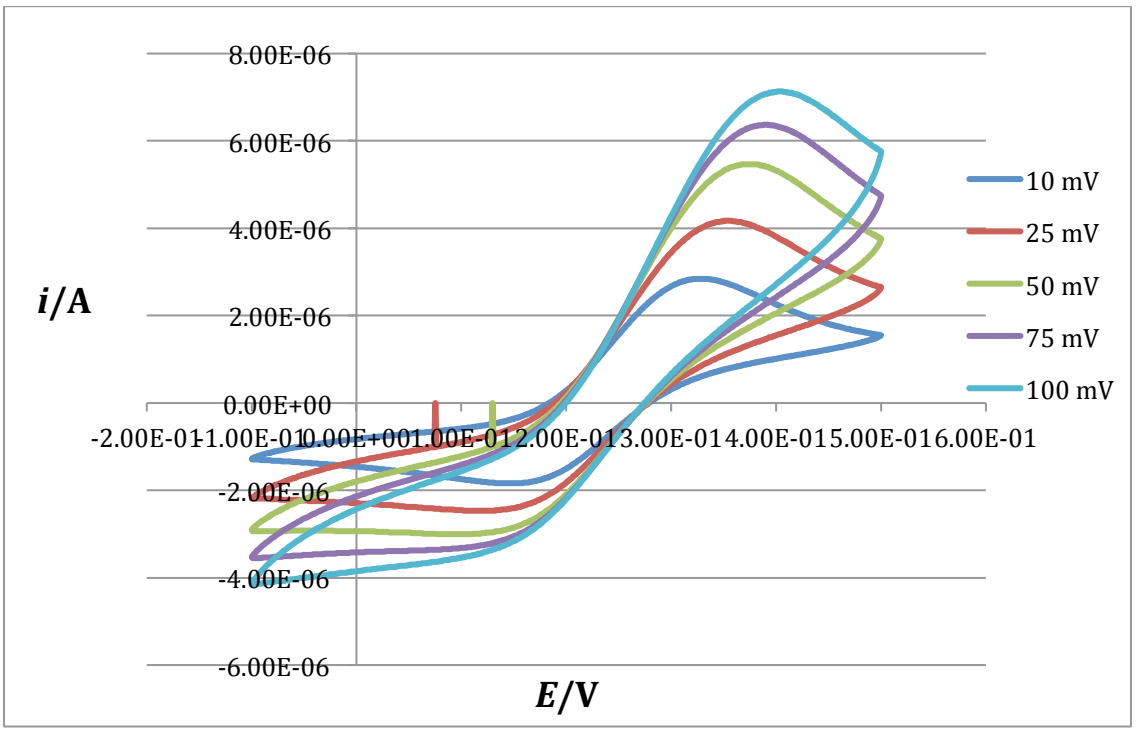

Figure 37 - A cyclic voltammogram using 1mM $Fe(CN_6)^{-3/-4}$ on electrode 2. Start potential -0.1 V, first potential 0.5 V. Scan rates 10 mV/s, 25 mV/s, 50 mV/s, 75 mV/s, 100mV/s.

Figure 37 shows CV *i-E* curves for 1mM $Fe(CN_6)^{-3/-4}$ using the residually doped microcrystalline diamond sample B electrode. Unlike the curves shown in figure 30, the curves shown in figure 37 have few characteristics representative of the classic sigmoidal shape and show little symmetry. It is impossible to measure the peak voltage separation for the curves in figure 37 as there is no back peak present, the graphs simply tail off steadily to a minimum current.

3.1.1.8 Electrode 1- Residually doped microcrystalline diamond sample A

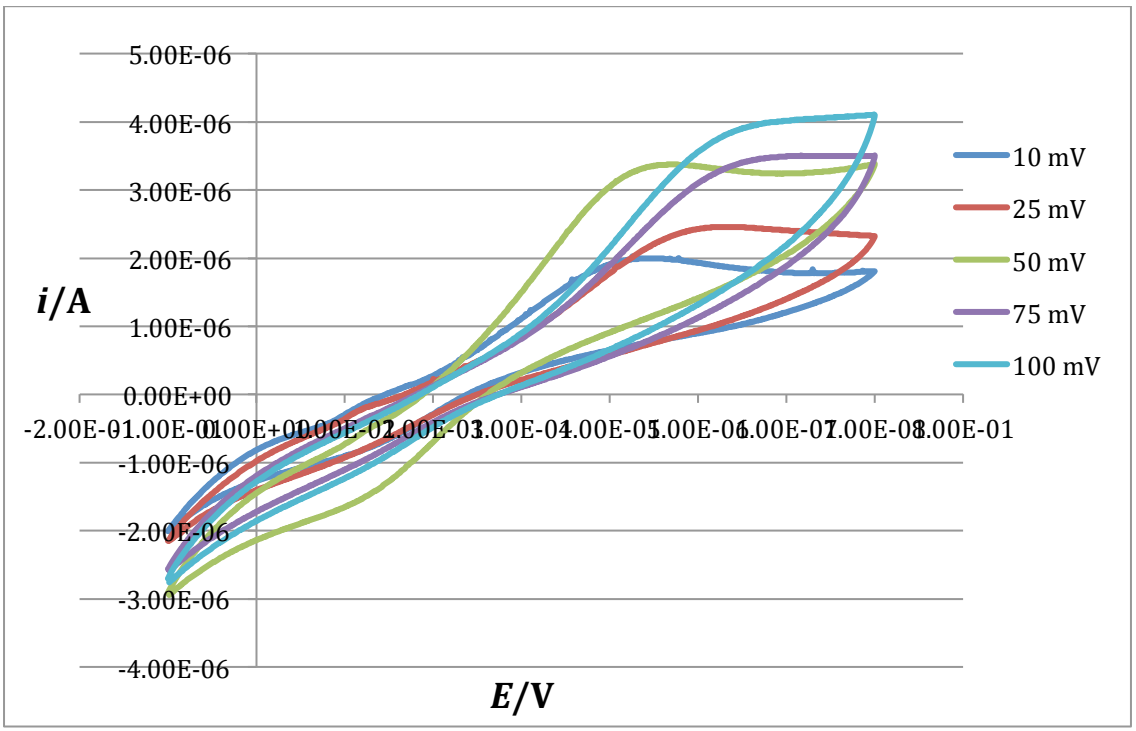

Figure 38 - A cyclic voltammogram using 1mM $Fe(CN_6)^{-3/-4}$ electrode 1. Start potential -0.1 V, first potential 0.7 V. Scan rates 10 mV/s, 25 mV/s, 50 mV/s, 75 mV/s, 100mV/s.

Figure 38 shows CV *i-E* curves for 1mM $Fe(CN_6)^{-3/-4}$ using the residually doped microcrystalline diamond sample A electrode. The curves shown in figure 38 are very different to those shown in figure 30 showing no sigmoidal features. There is no back peak, and compared to the curves in figures 35, 36 and 37 the graph slopes to a minimum current in a much steeper fashion.

3.1.2 Potassium chloride (KCl)

A KCl solution was used as it is an electrolyte with no electron transfer. This allows the capacitive and resistive behaviour of the electrode to be observed. Electrodes that showed capacitive behaviour (and in turn, little resistance) have been used for impedance measurements.

Capacitive behaviour can be observed by the extent to which the graph is centred around the x-axis. A graph which shows typical capacitive behaviour should be a rectangular, box like shape focused around the x-axis with little or ideally no slope as seen in the graph in figure 39.

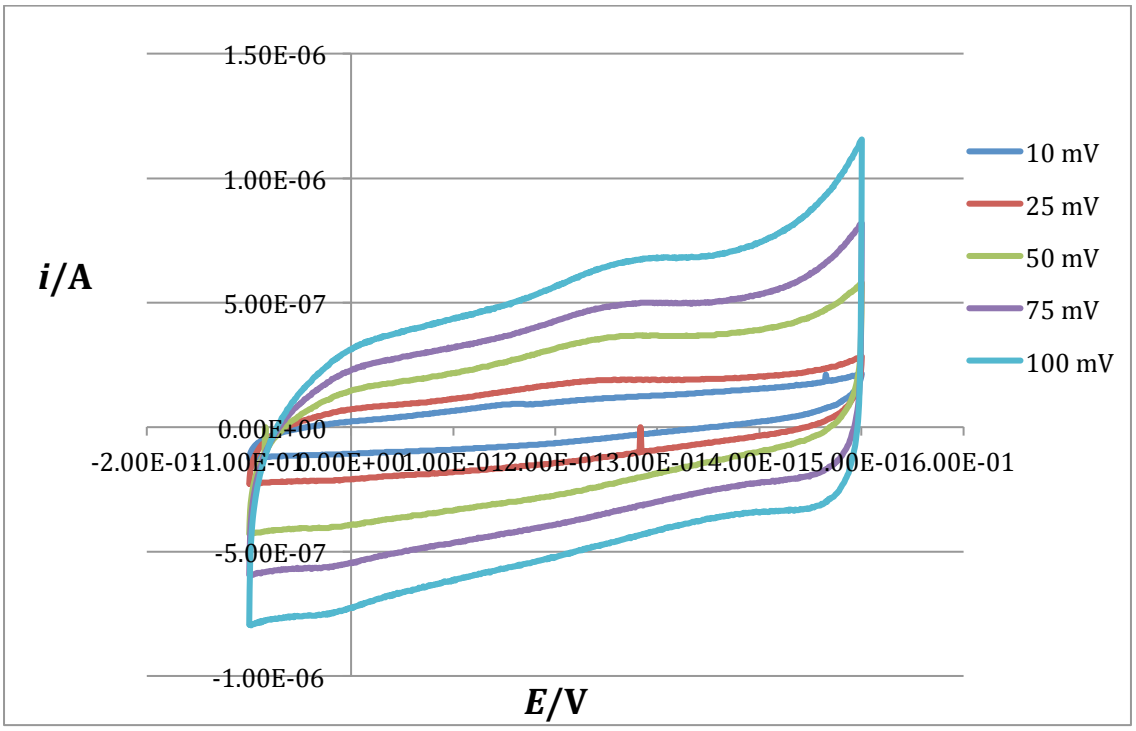

Figure 39 - A cyclic voltammogram using a KCl system on electrode 4. Start potential -0.1 V, first potential 0.5 V. Scan rates 10 mV/s, 25 mV/s, 50 mV/s, 75 mV/s, 100mV/s.

Figure 40 shows a graph that is characteristic of resistive behaviour. This can be defined by the gradient of the graph as the steeper the graph, the more resistive the electrode.

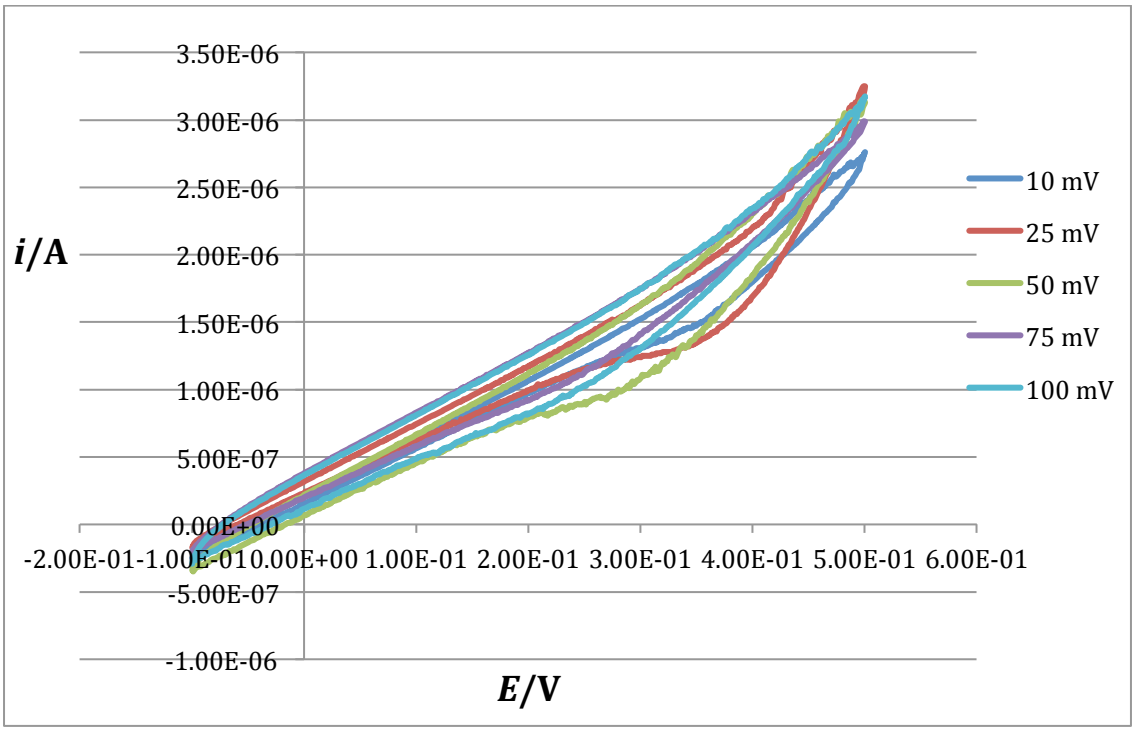

Fig 40 - A cyclic voltammogram using a KCl system on electrode 3. Start potential -0.1 V, first potential 0.5 V. Scan rates 10 mV/s, 25 mV/s, 50 mV/s, 75 mV/s, 100mV/s.

Figure 41 shows CV *i-E* curves for 8 different electrodes taken at a scan rate of 50 mV/s using a 1M KCl solution. CV graphs were constructed for all electrodes in the KCl solution but it is difficult to understand their relevance unless they are plotted on the same scale. The graph shown in figure 22 shows CV's taken for each electrode at the same scan rate, plotted on the same scale. This allows the resistive versus capacitive behaviour to be observed for each electrode with respect to one another. It is clear from figure 41 that electrode 3 shows the most resistive behaviour by far, indicated by the very steep nature of the curve. The curve corresponding to electrode 1 shows a steep gradient at higher potentials.

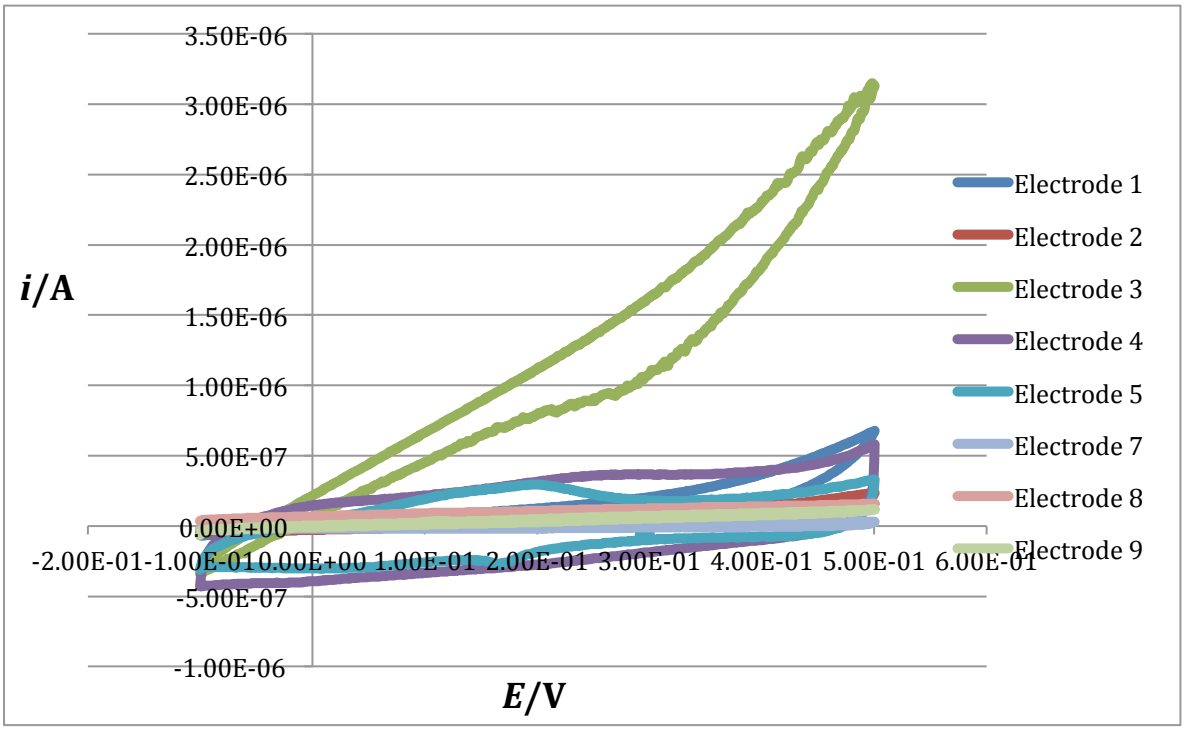

Fig 41 – A graph overlaying cyclic voltammograms using 1M KCl taken at a scan rate of 50 mV/s using 8 different electrodes.

The reason some electrodes show very high resistance is most likely down to a bad ohmic contact. Silver dag was used when making the electrode to connect the copper wire to the sample. Two different types of silver dag were used, but there has been no correlation found between electrodes that show a high resistance and a particular type of conductive paint.

3.2 Impedance measurements

Impedance measurements were taken on those electrodes that did not show high resistance in the KCl CV's visible in figure 41. The following electrodes were used for impedance measurements:

2 - Residually doped microcrystalline diamond teepee sample B
4 - Highly doped microcrystalline diamond teepee sample B
5 - Highly doped nanocrystalline teepee diamond sample B
6 - Undoped silicon – heavily boron doped diamond

The circuit *RQ* was fit to each set of impedance data measured where *R* is a resistor and *Q* is a capacitor. With respect to the circuit present, *R* corresponds to the resistance of the electrical back contact and *Q* corresponds to the double layer capacitor.

Values for *R, Q* and *n* are given as follows:

Component measured	**Value**	**Error (%)**
R	156.8 kOhm	4.38
Q	0.224 μF	5.73
n	0.935	0.533

Table 3 – A table to show *R, Q* and *n* values calculated from impedance data and corresponding percentage errors for electrode 2.

3

Component measured	**Value**	**Error (%)**
R	0.556 kOhm	1.04
Q	2.95 μF	2.83
n	0.943	0.285

Table 4 – A table to show *R, Q* and *n* values calculated from impedance data and corresponding percentage errors for electrode 4.

Component measured	**Value**	**Error (%)**
R	195 Ohm	3.11
Q	0.894 μF	4.84
n	0.934	0.537

Table 5 – A table to show *R, Q* and *n* values calculated from impedance data and corresponding percentage errors for electrode 5.

Component measured	**Value**	**Error (%)**
R	165.9 Ohm	6.05
Q	0.670 µF	3.61
n	0.932	0.670

Table 6 – A table to show *R, Q* and *n* values calculated from impedance data and corresponding percentage errors for electrode 7.

It is expected that values calculated for resistance should be on the Ohm scale, however as seen in tables 41 and 42, those values calculated for electrodes 2 and 4 are given in kOhms. This would suggest that electrodes 2 and 4 have a much higher resistance than electrodes 5 and 7. As shown in tables 42 and 44, electrodes 5 and 6 present *R* values in Ohms.

The *R* value given for electrode 4 shown in table 3 is 0.556 kOhm which is approximately 3 times that of the *R* values given for electrodes 5 and 6. The *R* value given for electrode 2 however, shown in table 3, is 156.8 kOhm which is approximately 1000 times bigger than the *R* values given for electrodes 5 and 6. This value is extremely large and therefore calculations surrounding the values given in table 3 will be treated with caution.

Electrode 2 showed a low resistance in the CV shown in figure 5 but a high resistance when impedance measurements were carried out (shown in table 3). This could be down to the electrolyte leaking into the back contact that would cause the resistance to be much higher. As the electrodes are very delicate it is also possible that the electrode could have been damaged in between the CV readings and the impedance measurements.

3.2.1 Errors

The values, including percentage errors, given in tables 3-6were output from the FRA software used to measure impedance.

3.3 Surface area calculations

As the units of capacitance Q are given in μF and the area of the electrode is given in cm^2, values for capacitances per unit area can be calculated as follows:

Eq (10) $$C = \frac{Q}{A}$$

By dividing the value of C calculated for each teepee electrode by the value of C calculated for the flat BDD electrode 7, a dimensionless relative surface area (or scale factor) for the surface area of the electrodes can be determined. From this relative surface area, the difference in surface area between the flat electrodes and teepee electrodes can be calibrated and quantified.

Electrode 6 - Undoped silicon – heavily boron doped diamond

Eq (10) $$C = \frac{Q}{A}$$

Eq (11) $$C = \frac{0.670\ \mu F}{0.071\ cm2} = 9.44\ \mu F\ cm^{-2}$$

Electrode 2 - Residually doped microcrystalline diamond sample B

Eq (10) $$C = \frac{Q}{A}$$

Values from table 3:

Eq (12) $$C = \frac{0.224\ \mu F}{0.071\ cm2} = 3.16\ \mu F\ cm^{-2}$$

Eq (13) $$\text{Relative surface area} = \frac{C}{C} = \frac{3.16\ \mu F\ cm{-}2}{9.44\ \mu F\ cm{-}2} = 0.34$$

Electrode 4 - Highly doped microcrystalline diamond sample B

Eq (10) $$C = \frac{Q}{A}$$

Values from table 4:

Eq (14) $C = \frac{2.95\ \mu F}{0.071\ cm2} = 41.55\ \mu F\ cm^{-2}$

Eq (15) Relative surface area $= \frac{C}{C} = \frac{41.55\ \mu F\ cm{-}2}{9.44\ \mu F\ cm{-}2} = 4.40$

Electrode 5 - Highly doped nanocrystalline diamond sample B

Eq (10) $C = \frac{Q}{A}$

Values from table 5:

Eq (16) $C = \frac{0.894\ \mu F}{0.071\ cm2} = 12.59\ \mu F\ cm^{-2}$

Eq (17) Relative surface area $= \frac{C}{C} = \frac{12.59\ \mu F\ cm{-}2}{9.44\ \mu F\ cm{-}2} = 1.33$

The values calculated from equations 12 and 13, both the capacitances per unit area and the relative surface area for electrode 2, are much lower than would be expected for a teepee sample. The value of capacitances per unit area calculated in equation 12 for electrode 2 is approximately a third of that calculated in equation 11 calculated for flat BDD (as seen from the relative surface area value calculated in equation 13). This would suggest that the teepee structures have a surface area that is a third of that for the flat BDD which does not seem logical. As noted in section 3.2, the calculations surrounding the values in Table 3 for electrode 2 will be treated with caution as the *R* value given is much larger than the values given for other electrodes. Possible reasons for this have been explained in section 3.2. Given that unusually small capacitances per unit area relative surface area values have been calculated in equations 12 and 13, these values will not be taken into account when considering the surface area of a BDD teepee structure to that of a flat BDD structure.

The values given in equations 14 and 16 show how much bigger the surface area of the teepee electrodes is compared to the flat BDD electrode. Equation 14 relating to electrode 4 shows that electrode 4 has a surface area 4.4 times bigger than that of the flat BDD electrode 6. Equation 16

relating to electrode 5 shows that electrode 5 has a surface area 1.33 times bigger than that of the flat electrode 6.

Macpherson et al [157] have reported a value of 58 μF cm^{-2} capacitances per unit area for polycrystalline BDD. The pBDD samples used in this study were highly doped, oxygen terminated pBDD.

In this study, from equation 11, a value of 9.44 μF cm^{-2} has been calculated for electrode 6 - undoped silicon – heavily boron doped diamond. This value is less than a sixth of 58 μF cm^{-2} which was reported in the literature. The difference between electrode 6 and the pBDD reported by Macpherson et al is that electrode 6 is not oxygen terminated. Oxygen terminating the electrodes could lead to a higher capacitances per unit area value.

3.4 Surface area estimation

A range of values for the surface area estimation can be calculated by using the maximum and minimum values as necessary and where applicable. This is highlighted at each stage.

There are four steps to get an estimate of the expected relative surface area for the teepee electrodes:

- Estimating the surface area of the CNT's
- Estimating the number of CNT's in a teepee
- Estimating the number of teepees per square area
- Estimating the relative surface area

As the CNT's are cylindrical in shape the surface area can be estimated using an adjusted formula for the surface area of a cylinder shown in equation 19 (adjusted from equation 18.) Electrodes 2, 4 and 5 are all sample B (CNT's 10-15 μm long) and given that surface area calculations have been done in section 4.3 for those electrodes, the height of the cylinder, *h*, will be taken as the average value, 12.5μm. The radius, *r*, of the cylinder can be estimated from A21 as approximately 0.67 μm.

Eq (18) $$A = 2\pi r^2 + 2\pi rh$$

The term $2\pi r^2$ relates to the area of the top of the cylinder plus the area of the bottom of the cylinder. Given that the area of the bottom of the CNT will be attached to the silicon substrate, the area of the bottom of the cylinder does not need to be included in the surface area equation. This therefore gives equation 19:

Eq (19) $$A = \pi r^2 + 2\pi rh$$

Where: $r = 0.67$ μm

$h = 12.5$ μm

Thus the surface area of the CNT's is calculated in equation (20):

Eq (20) $$A = \pi\, 0.67^2 + (2\pi \times 0.67 \times 12.5)$$

$$A = 54.03\ \mu m^2$$

The number of CNT's in a teepee can be estimated using the SEM images A9 and A22. A9 allows the number of CNT's/10 μm^2 to be counted, and A22 allows the number of teepees/10 μm^2 to be counted. The maximum number of CNT's/teepee can be calculated from equation (21), dividing the maximum number of CNT's/10 μm^2 by the minimum number of teepees/10 μm^2. The minimum number of CNT's/teepee can be calculated from equation (22) by dividing the minimum number of CNT's/10 μm^2 by the maximum number of teepees/10 μm^2 where values are given below:

No of CNT's (max) = 160/10 μm^2

No of CNT's (min) = 140/10 μm^2

No of teepees (max) = 14/10 μm^2

No of teepees (min) = 8/10 μm^2

Eq (21) $$\text{No of CNT's/teepee (max)} = \frac{160}{8} = 20$$

Eq (22) $$\text{No of CNT's/teepee (min)} = \frac{140}{14} = 10$$

The surface area of a teepee can therefore be calculated by multiplying the surface area of a CNT by the number of CNT's in a teepee.

Equation (23) gives the maximum surface area of a teepee by multiplying equation (20) by equation (21):

Eq (23) $\text{Surface area}_{max}\text{ (teepee)} = 54.03\ \mu m^2 \times 20 = 1080.6\ \mu m^2$

Equation (24) gives the minimum surface area of a teepee by multiplying equation (20) by equation (22):

Eq (24) $\text{Surface area}_{min}\text{ (teepee)} = 54.03\ \mu m^2 \times 10 = 540.3\ \mu m^2$

If there are a maximum of 14 teepees/10 μm^2 then there are 1.4 teepees/μm^2. Equation (25) gives a dimensionless maximum relative surface area by multiplying equation (23) by the number of teepees/μm^2:

Eq (25) $\text{Relative surface area (max)} = 1080.6 \times 1.4 = 1512.84$

If there are a minimum of 8 teepees/10 μm^2 then there are 0.8 teepees/μm^2. Equation (26) gives a dimensionless minimum relative surface area by multiplying equation (24) by the number of teepees/μm^2:

Eq (26) $\text{Relative surface area (min)} = 540.3 \times 0.8 = 432.24$

From equations (25) and (26) a range of relative surface area from 432.24 - 1512.84 has been calculated. If the value of the relative surface area calculated as 0.34 from equation (13) (for electrode 2) is not taken into consideration, (as explained in sections 3.2 and 3.3) the experimentally determined range calculated from equations (17) and (15) respectively is 1.33 – 4.40. The experimentally determined range is 3-4 orders of magnitude smaller than that estimated in this section.

Although it seems illogical that the two sets of values differ by 3-4 orders of magnitude and this could signify errors in both the experimental work and the estimation calculations, there are also ideas about the electrochemical activity of the teepees that can be inferred from this. One idea is that both the CNT's at the centre of the teepee, and the surface of the CNT's that are facing the centre of the teepee are not electrochemically active therefore significantly reducing surface area. Section 1.9.2 states "Voltammetric data would suggest that the sidewalls of MWNT's are chemically inert and that the open end of the nanotube dominates the electrochemistry." [141, 142] This gives good reason to suggest that the sides of the nanotubes are not electrochemically active and therefore it is possible that only a limited area of the teepee (mainly the top of the CNT's) is giving an electrochemical response. This would account for lower capacitance values and in turn lower surface area values.

4. Conclusion

It has been proven that boron doped diamond carbon nanotube teepee electrodes do work as electrodes. Figure 30, the CV for the oxidation and reduction of ferri/ferro cyanide at electrode 5 shows an almost perfect reversible response curve and the diffusion coefficient of 4.56×10^{-6} cm^2 s^{-1} calculated in equation (9) is of the same magnitude of those reported in the literature. However there have been problems reproducing the perfect reversible curve that is expected from a ferri/ferro cyanide system for all electrodes. Electrode 5 is highly doped nano-crystalline diamond sample B and although there are features of this electrode such as high boron doping levels and longer CNT's that may bode well for electrochemistry in theory, this does not explain why some of the other electrodes with equally good features did not produce good, reversible electrochemical response curves.

There is also no logical reason why some of the electrodes would show a particularly high resistance compared to others. Therefore it can be assumed that there is something fundamentally wrong with some of the electrodes. The most likely problem relates to the ohmic contact. A good ohmic contact should not reduce the performance of the electrode and should pass the required current with only a small drop in voltage compared to the drop across the active region of the electrode.

Silver dag was used to make the ohmic contact in this experiment. Although it has been shown that silver dag is a good material with which to make an electrical contact, it can give poor results. [4] A more suitable ohmic contact could be made from titanium gold as it has been proven to be a low resistance contact. [158, 159]

Another problem with regards to making the electrodes and the general handling of the electrodes is how delicate they are. Simply touching or knocking the top of the sample/electrode will squash and hence destroy the CNT's on the surface that will obviously have an effect on the electrochemical response and the surface area of the electrode. Making the electrodes was a very delicate process requiring a certain degree of dexterity given that the samples were so small (approximately $1cm^2$.) It would be easy to knock the surface of the sample in electrode preparation and also in storage, transporting the electrodes and in setting up the electrochemical cell so particular care has to be taken.

It would be useful if there were high-resolution SEM images of the samples that allowed the number of CNT's in a teepee to be counted to a closer approximation as there is still an element of guess work regarding the calculations and estimations in section 3.4. SEM images of all samples at exactly the same resolution would also be useful so that the number of teepees in a certain area could be counted accurately and compared to the number of teepees in another sample. Getting a reasonably accurate estimation to the number of CNT's in a teepee and the number of teepees in a certain area would enable a better estimation of the surface area against which experimental values could be compared.

However, a range of values for the relative surface area has been calculated as 432.24 - 1512.84 from equations (25) and (26) which has lead to the theory that only the tip of the teepee dominates the electrochemistry given that the relative surface area values from the experimental data are significantly lower (see section 3.3).

Although this report may not have found out exactly how each sample compares to one another electrochemically (as some of the CV's for ferri/ferro cyanide did not give reversible curves as expected) it can be concluded that electrode 5, the highly doped nano-crystalline diamond sample B electrode gave the best response and showed the most reversible curve. Measurements with other electrodes will have to be repeated (possibly with a different ohmic contact) to get a real idea of how the different electrodes compare to one another.

The graphs shown in figures 30 and 32 corresponding to two of the teepee electrodes (5 and 4 respectively) have shown more reversible responses than the flat electrode (shown in figure 33.) This proves that the teepee structures are capable of producing reversible sigmoidal CV's that can better those corresponding to flat BDD structures.

5. Future work

It would be interesting to repeat the experiments to see if the results are replicable. Rather than using a silver dag electrical contact, a titanium gold electrical contact may prove more effective and would hopefully lower the resistance of some of the electrodes/samples. Macpherson et al [127] reported a capacitances per unit area value of 58 μF cm^{-2} for an oxygen terminated pBDD sample which is much larger than any of the capacitances per unit area values calculated in this study for BDD teepees. It would be interesting to oxygen terminate the samples by putting them in the ozone cleaner and take impedance measurements and calculate the capacitances per unit area values again to see what/if any difference oxygen termination made to the results.

6. Appendix

6.1 CV's

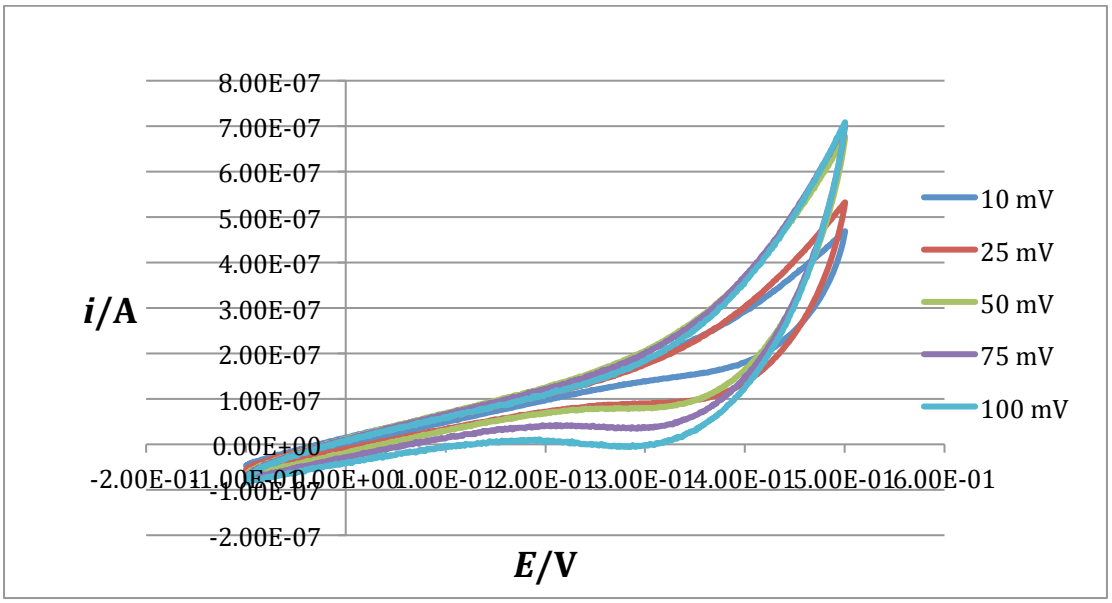

A 1 - A cyclic voltammogram using a KCl system on electrode 1. Start potential -0.1 V, first potential 0.5 V. Scan rates 10 mV/s, 25 mV/s, 50 mV/s, 75 mV/s, 100mV/s.

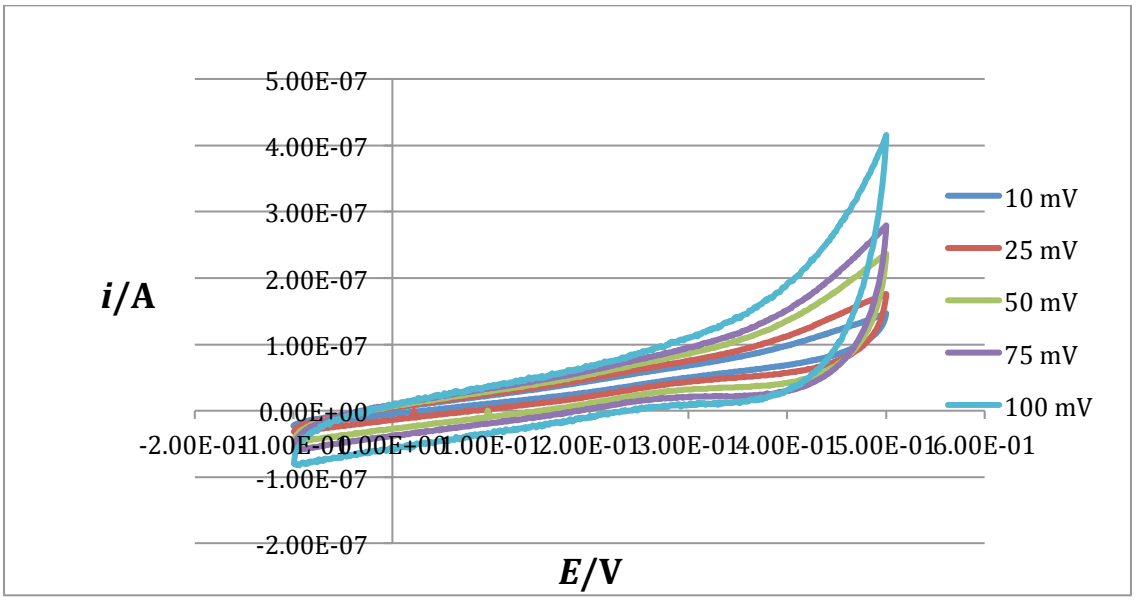

A 2 - A cyclic voltammogram using a KCl system on electrode 2. Start potential -0.1 V, first potential 0.5 V. Scan rates 10 mV/s, 25 mV/s, 50 mV/s, 75 mV/s, 100mV/s.

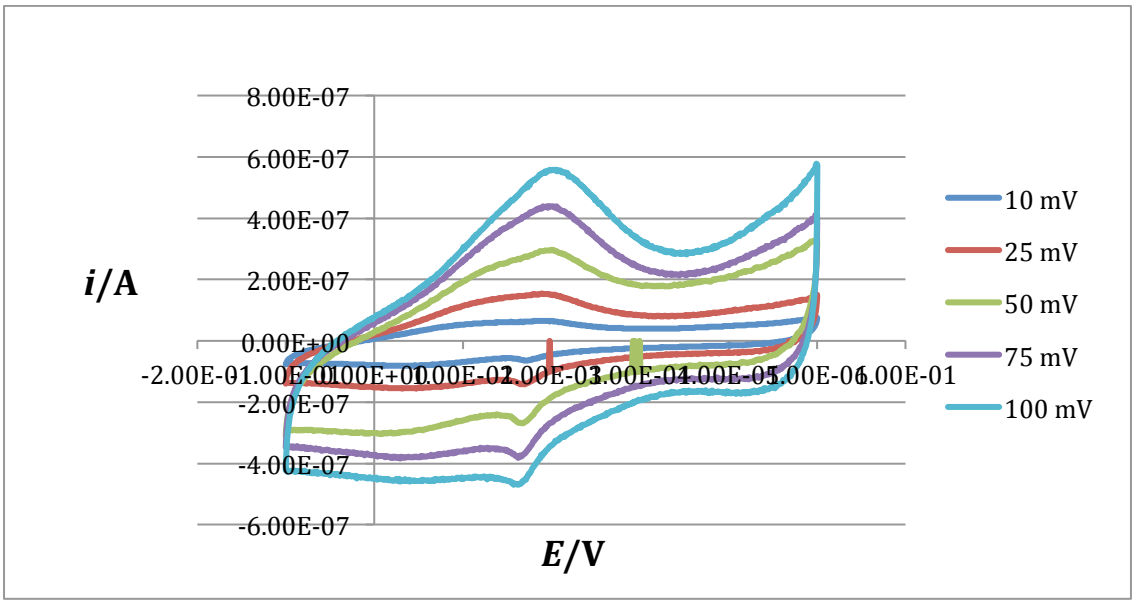

A 3 - A cyclic voltammogram using a KCl system on electrode 5. Start potential -0.1 V, first potential 0.5 V. Scan rates 10 mV/s, 25 mV/s, 50 mV/s, 75 mV/s, 100mV/s.

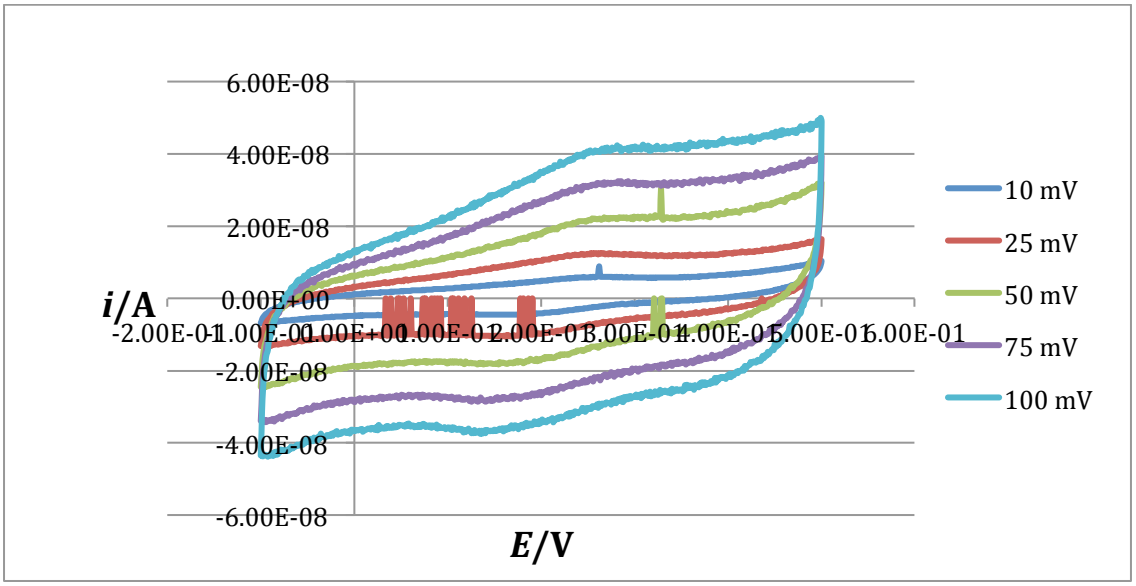

A 4 - A cyclic voltammogram using a KCl system on electrode 6. Start potential -0.1 V, first potential 0.5 V. Scan rates 10 mV/s, 25 mV/s, 50 mV/s, 75 mV/s, 100mV/s.

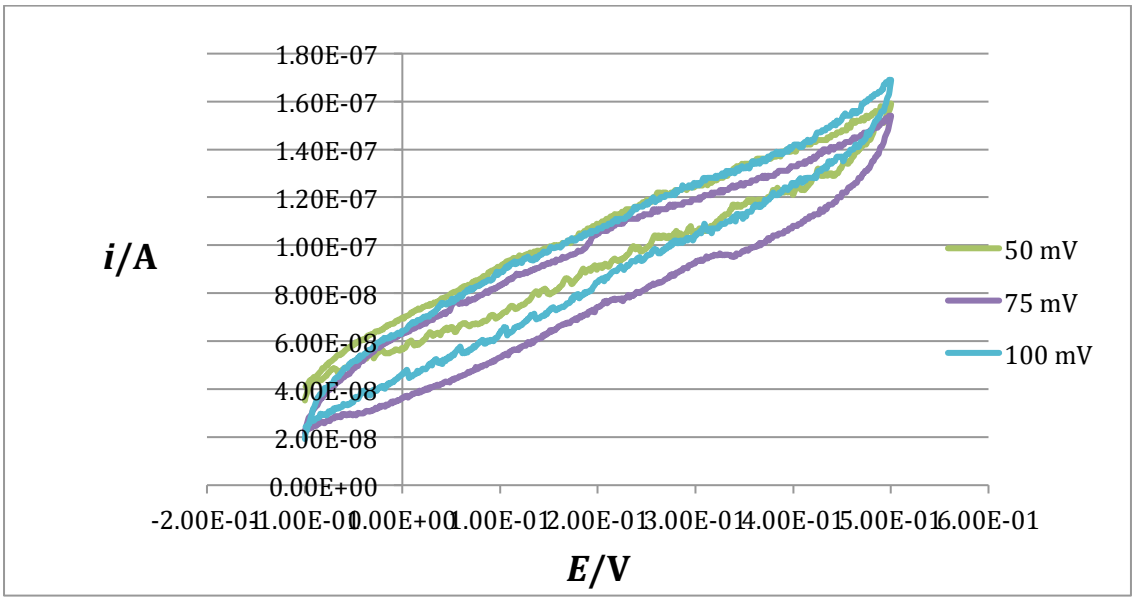

A 5 - A cyclic voltammogram using a KCl system on electrode 7. Start potential -0.1 V, first potential 0.5 V. Scan rates 10 mV/s, 25 mV/s, 50 mV/s, 75 mV/s, 100mV/s.

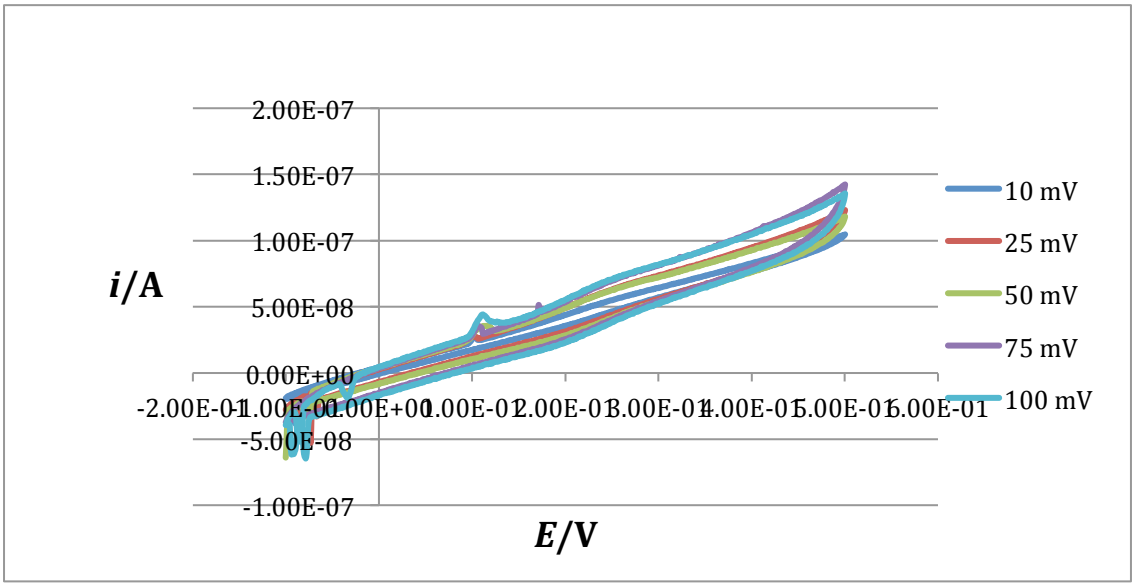

A 6 - A cyclic voltammogram using a KCl system on electrode 8. Start potential -0.1 V, first potential 0.5 V. Scan rates 10 mV/s, 25 mV/s, 50 mV/s, 75 mV/s, 100mV/s.

6.2 SEM images

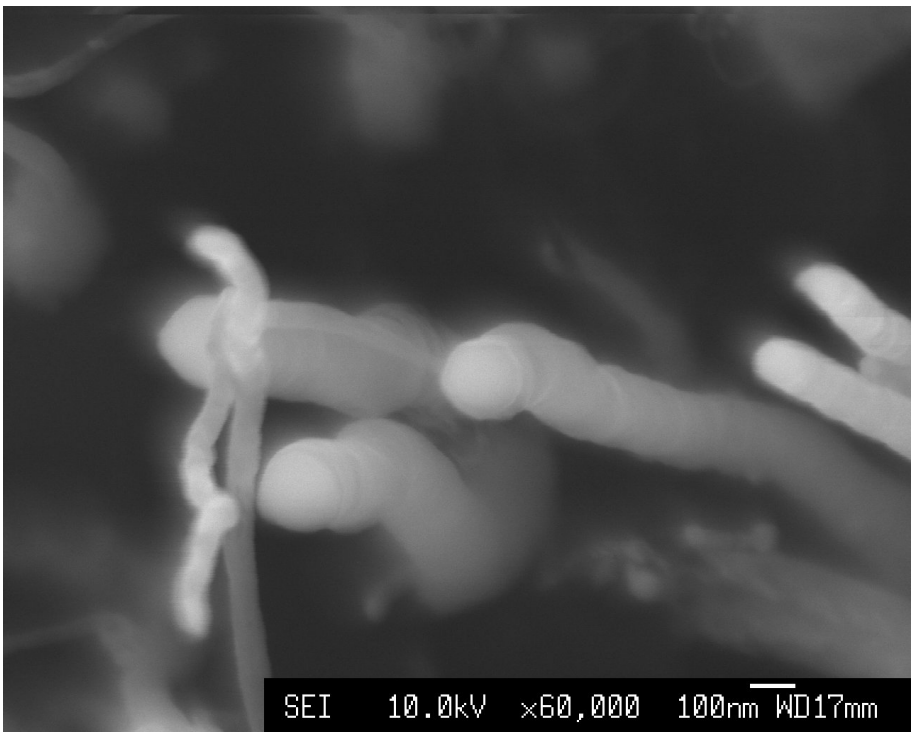

A 7 – SEM image using high-resolution SEM of undoped CNT's.

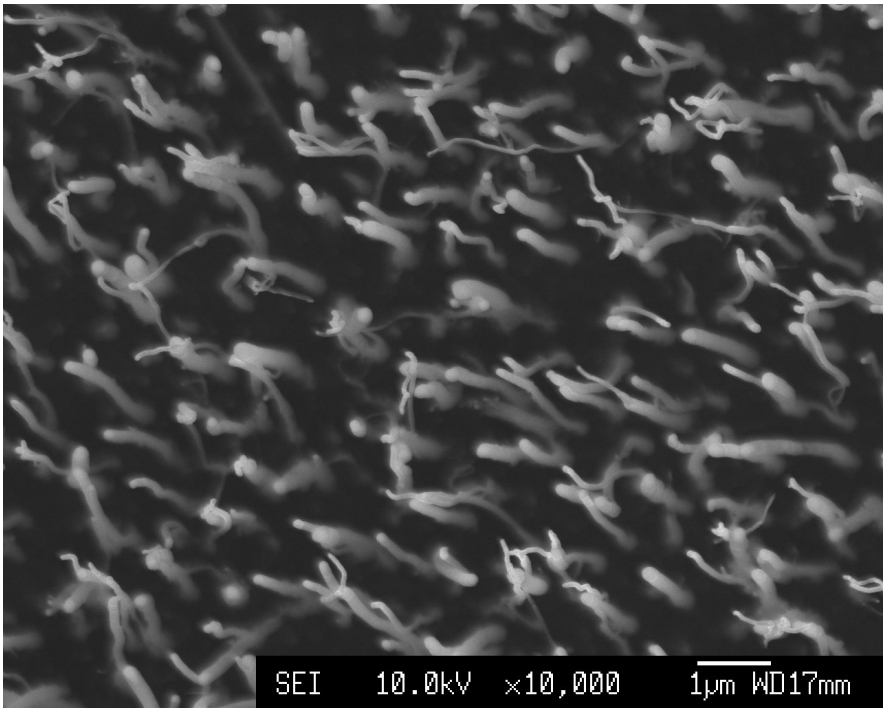

A 8 - SEM image using high-resolution SEM of undoped CNT's.

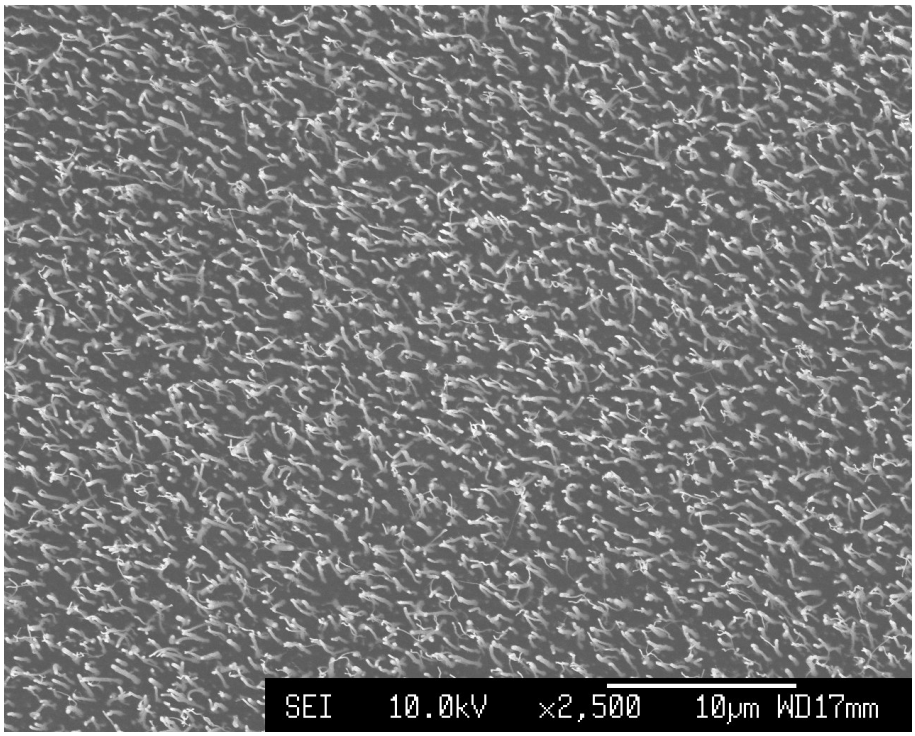

A 9 - SEM image using high-resolution SEM of undoped CNT's.

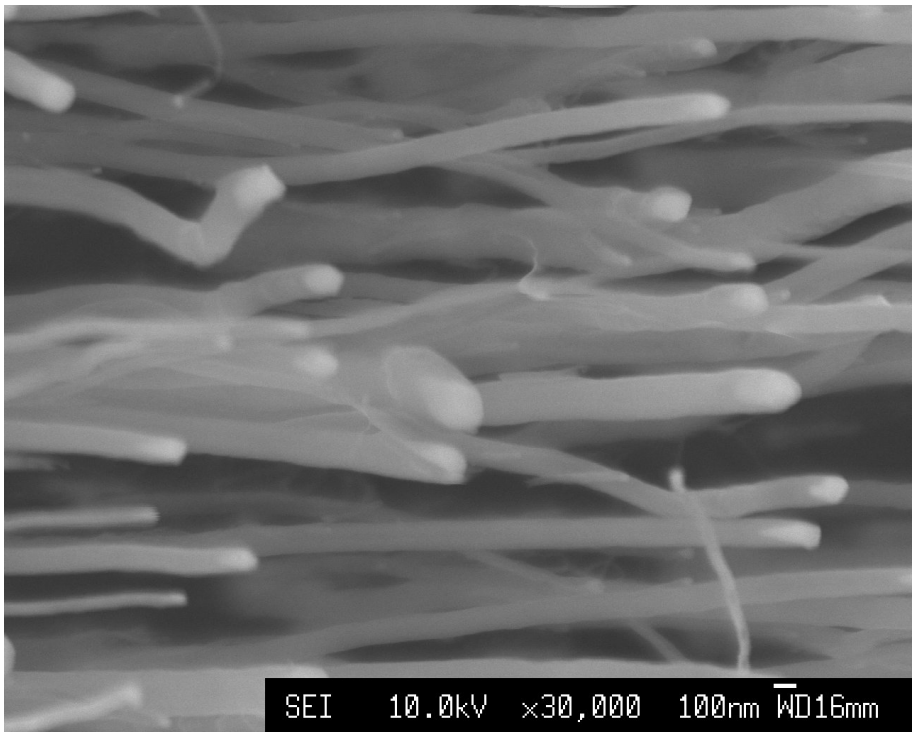

A 10 - SEM image using high-resolution SEM of undoped CNT's.

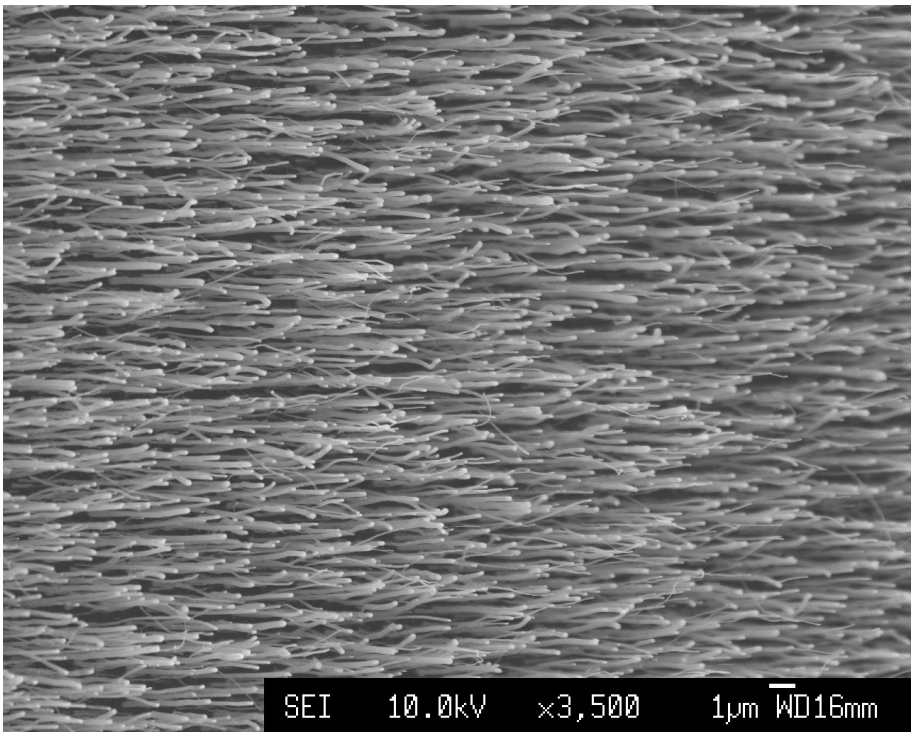

A 11 - SEM image using high-resolution SEM of undoped CNT's.

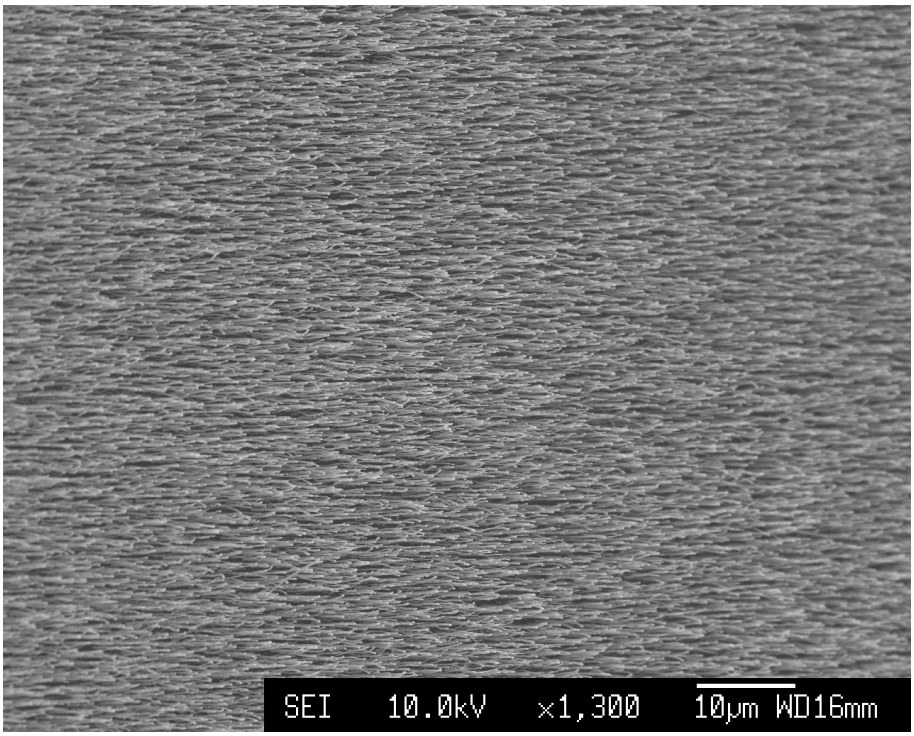

A 12 - SEM image using high-resolution SEM of undoped CNT's.

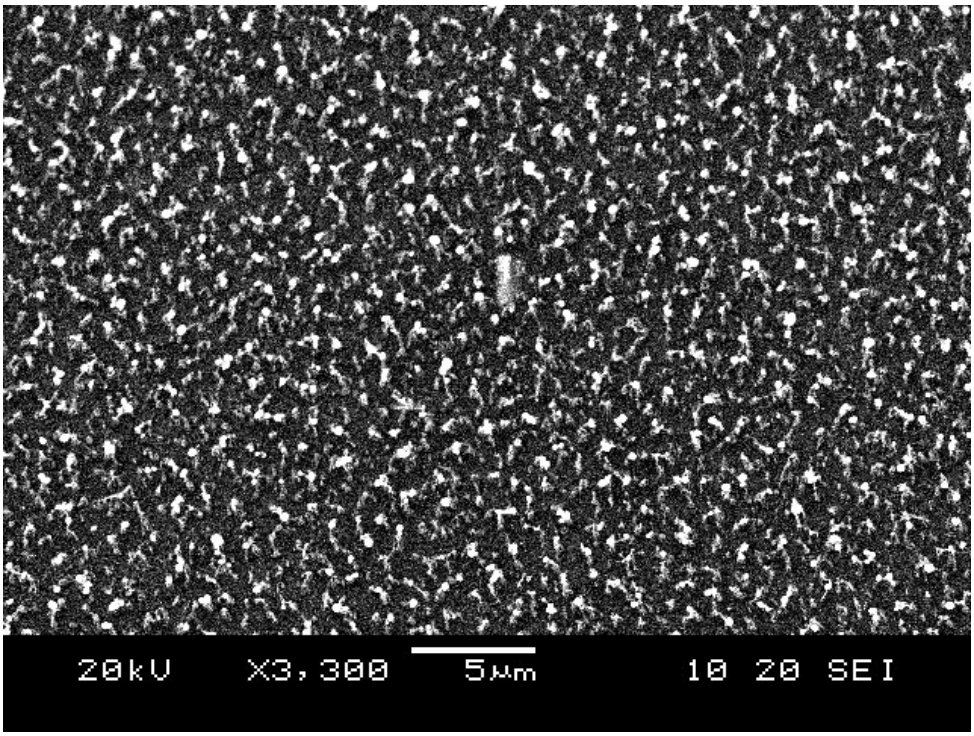

A 13 – SEM using normal resolution SEM of electrode 1.

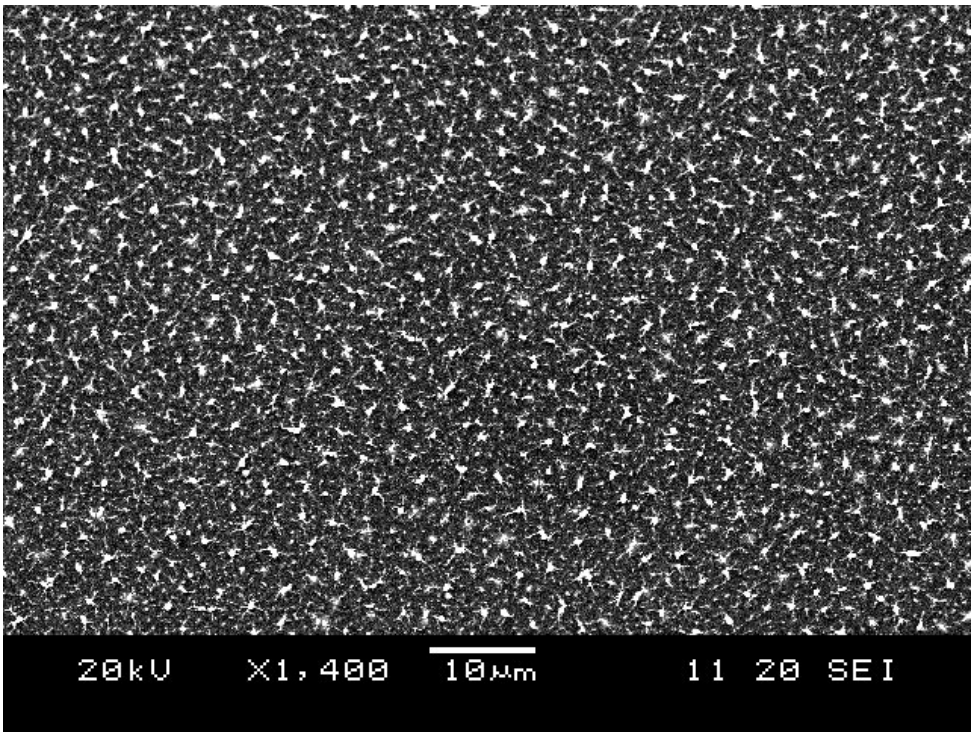

A 14 – SEM using normal resolution SEM of electrode 2.

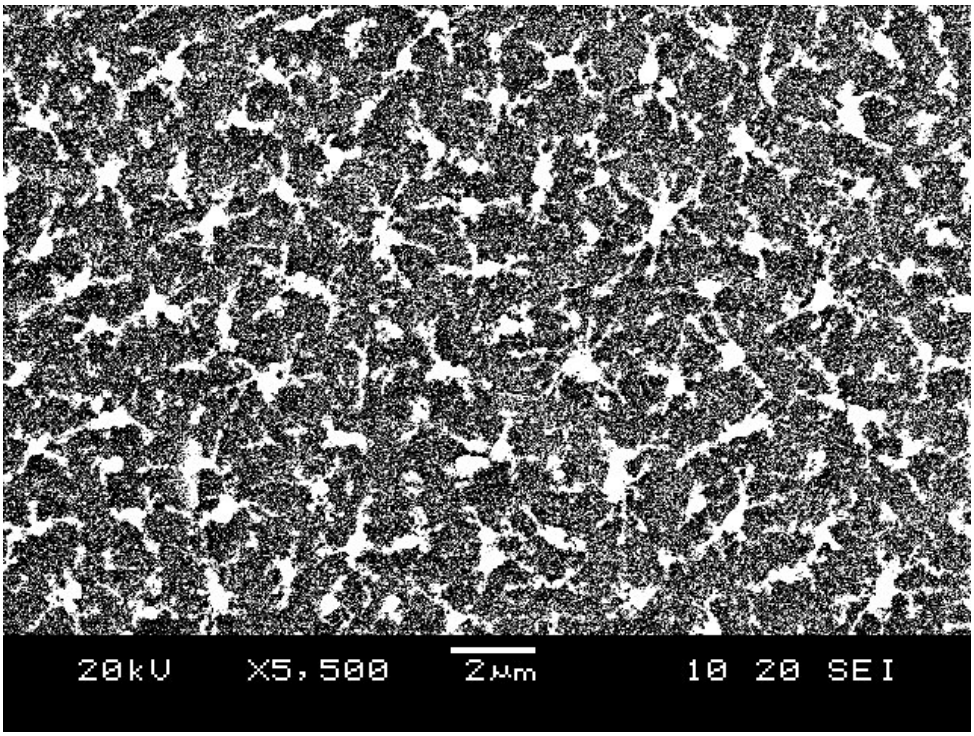

A 15 – SEM using normal resolution SEM of electrode 3.

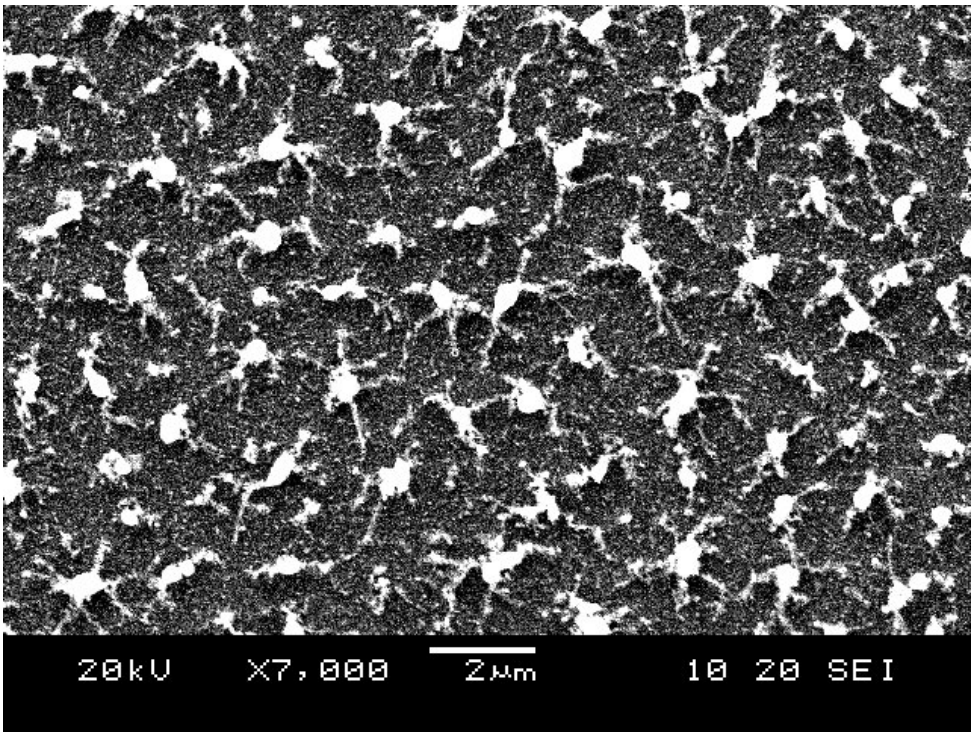

A 16 – SEM using normal resolution SEM of electrode 3.

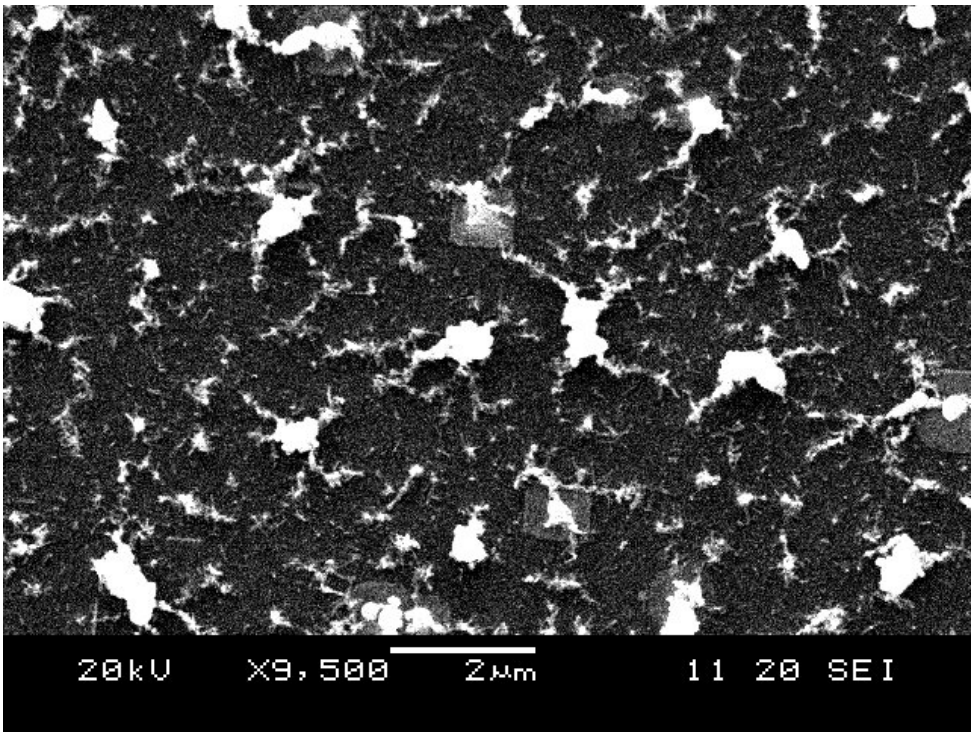

A 17 – SEM using normal resolution SEM of electrode 3.

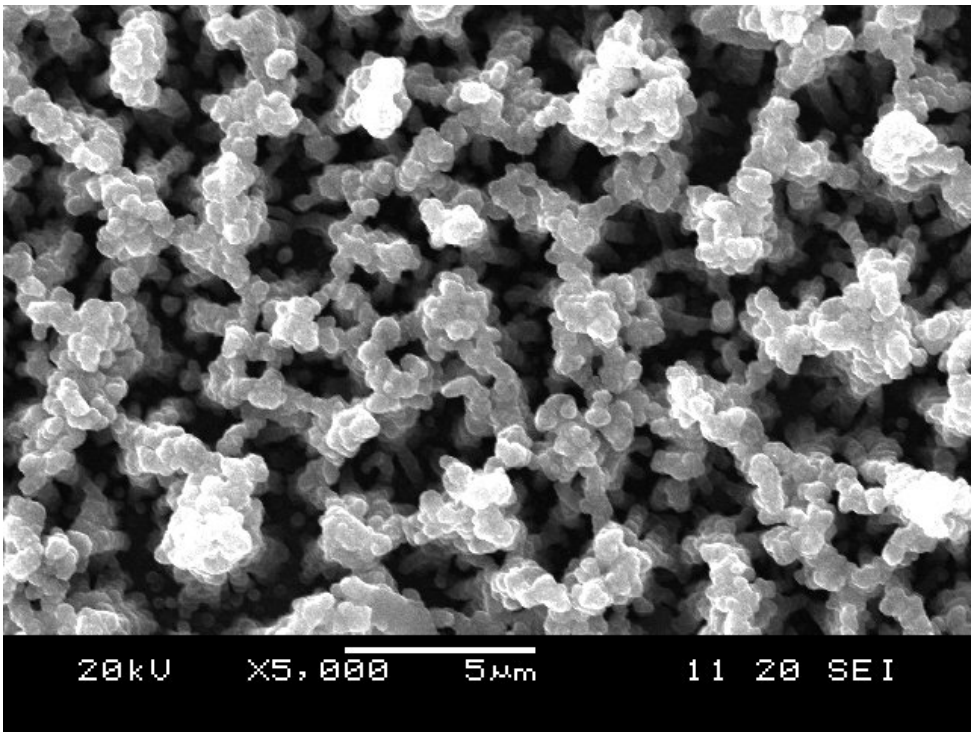

A 18 – SEM using normal resolution SEM of electrode 4.

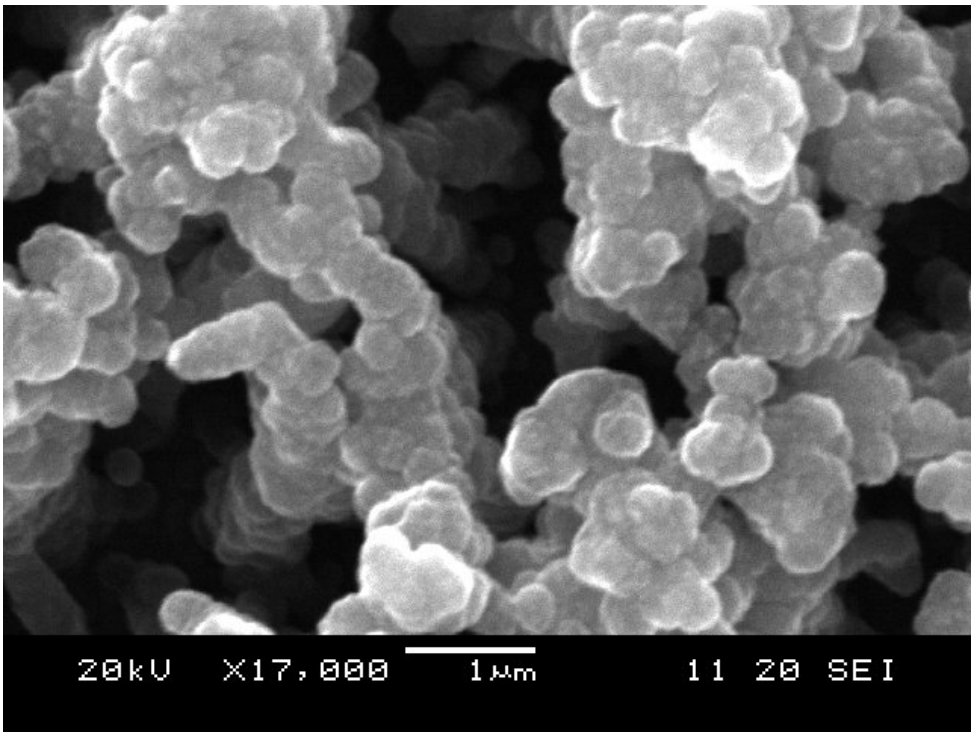

A 19 – SEM using normal resolution SEM of electrode 4.

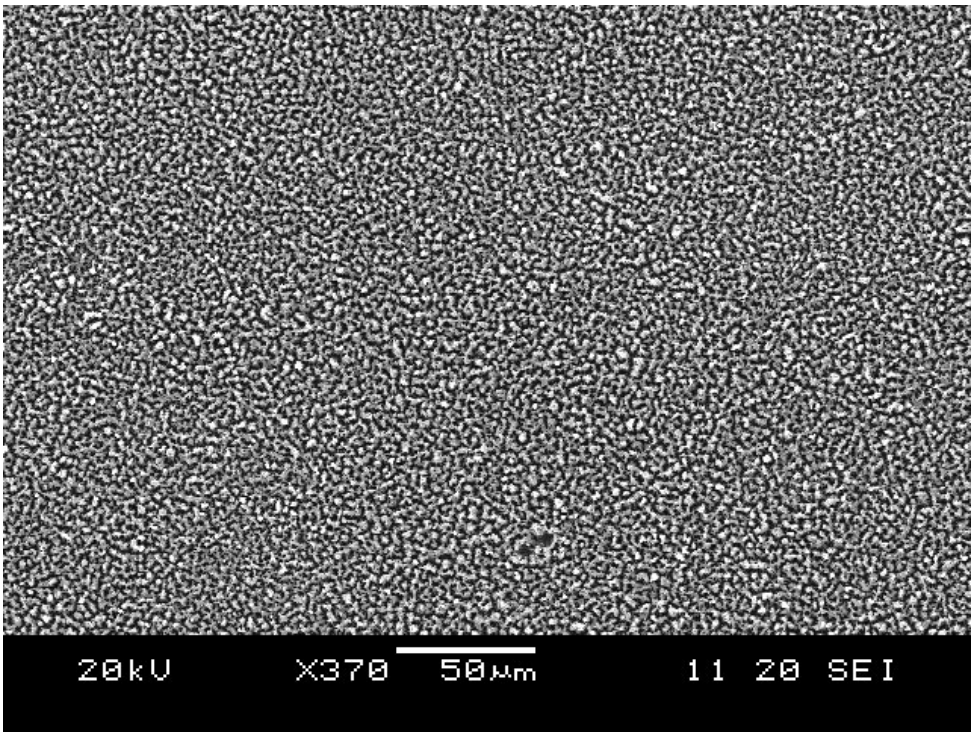

A 20 – SEM using normal resolution SEM of electrode 4.

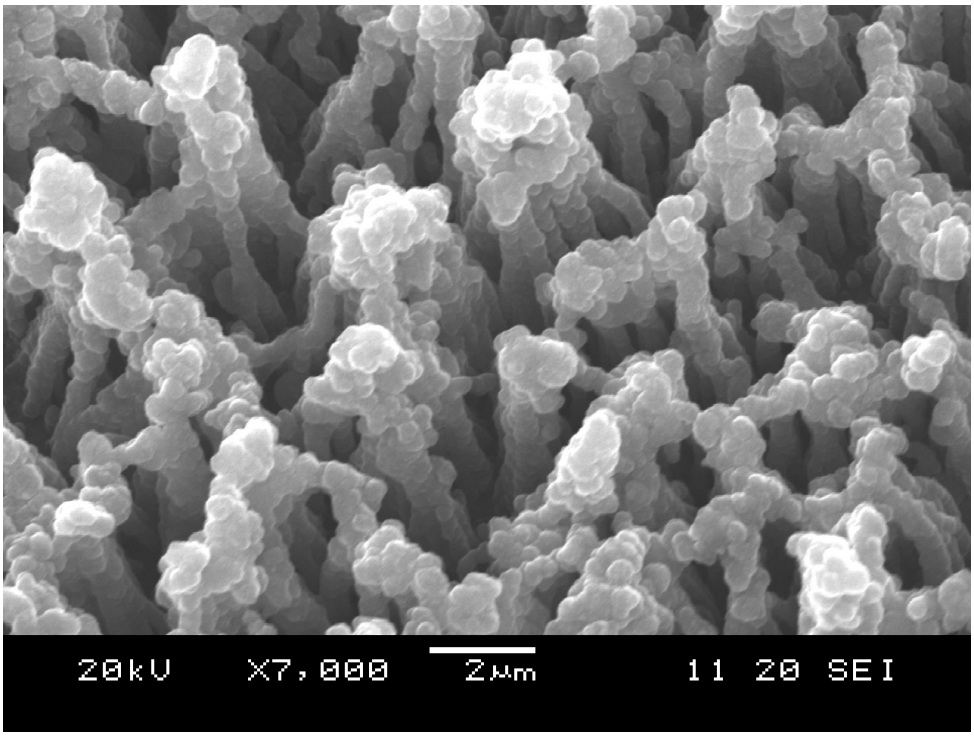

A 21 – SEM using normal resolution SEM of electrode 4.

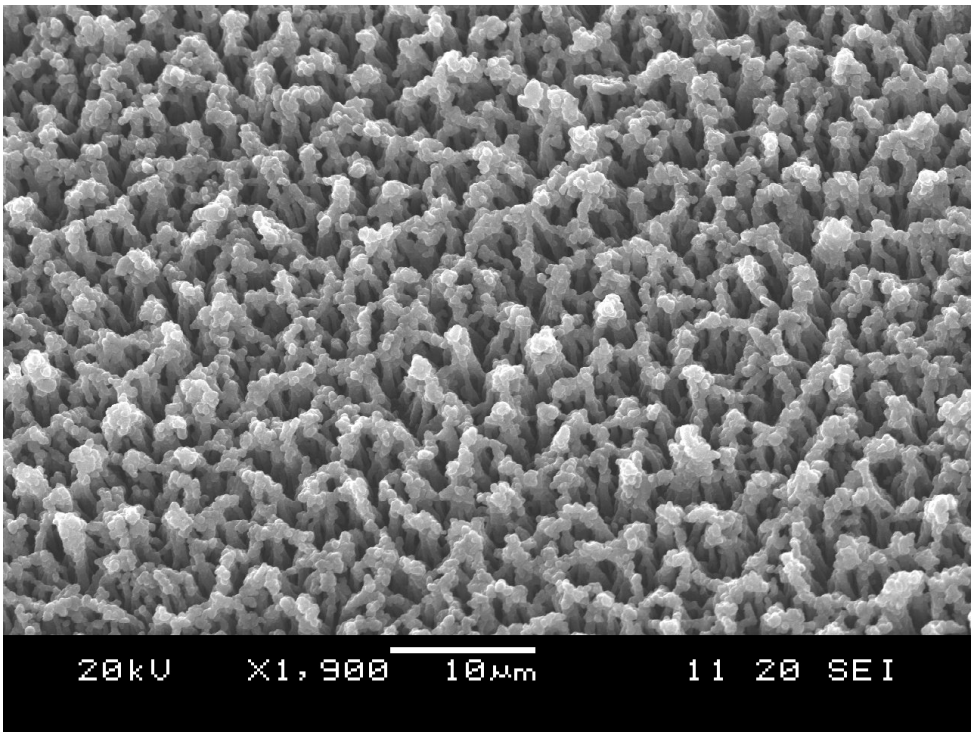

A 22 – SEM using normal resolution SEM of electrode 4.

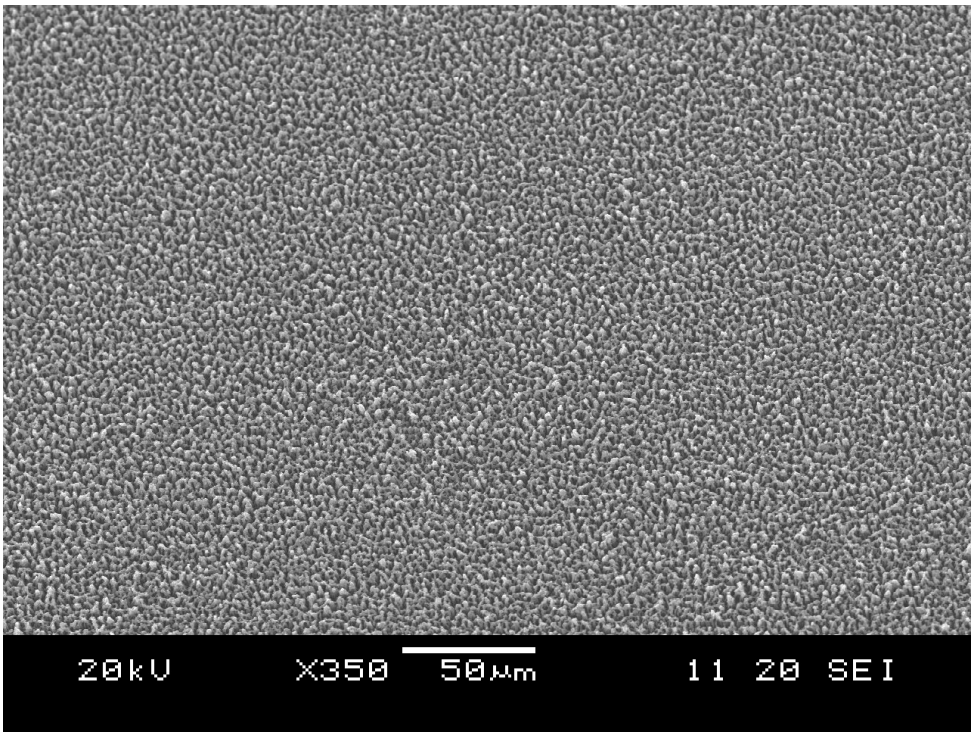

A 23 – SEM using normal resolution SEM of electrode 4.

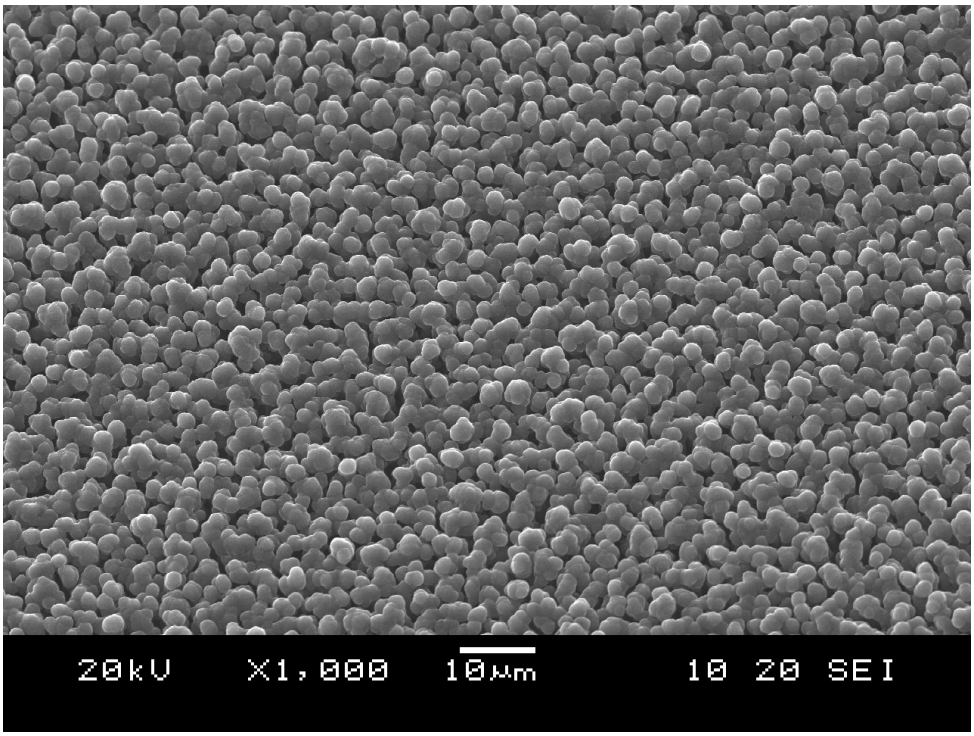

A 24 – SEM using normal resolution SEM of electrode 5.

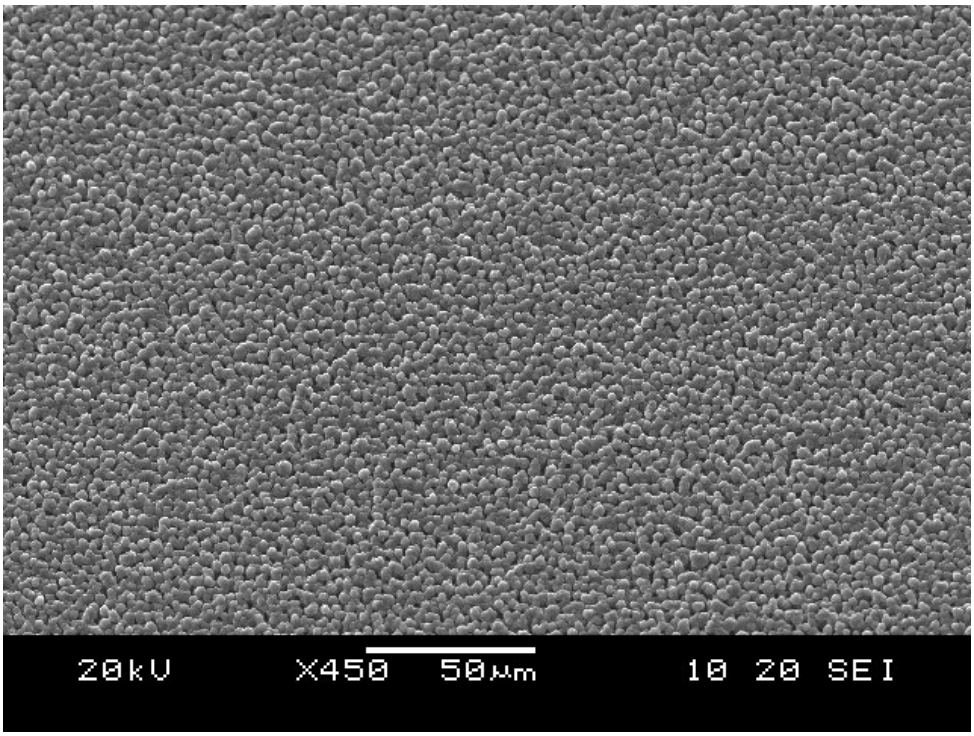

A 25 – SEM using normal resolution SEM of electrode 5.

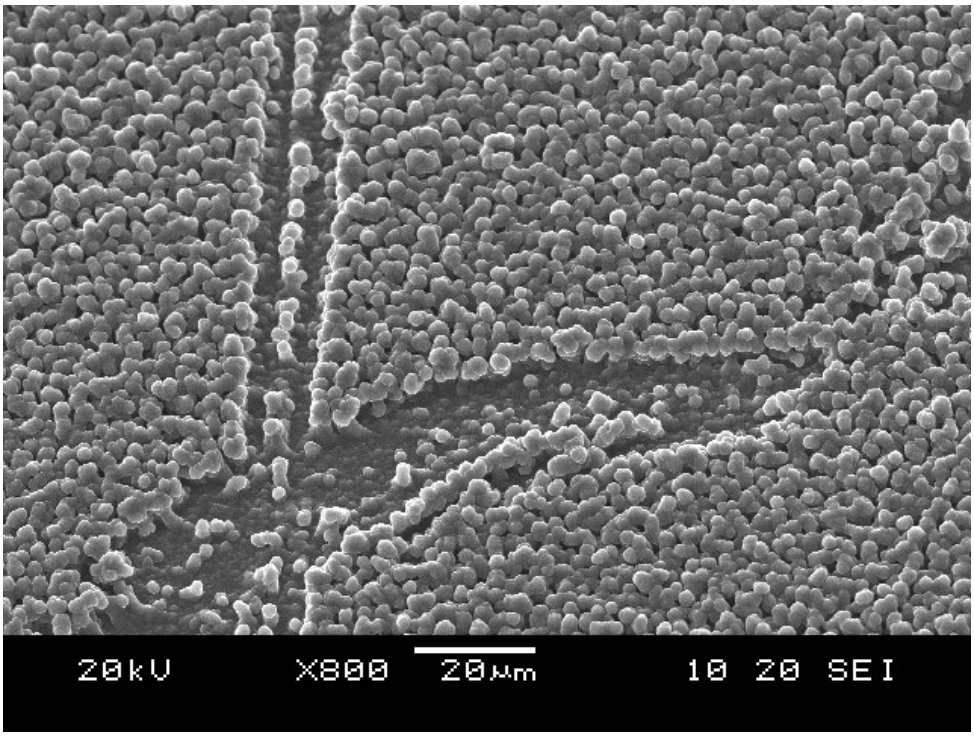

A 26 – SEM using normal resolution SEM of electrode 5.

References

1 - http://cnx.org/content/m22963/latest/

2 - Stark, J.G. and Wallace, H.G. Chemistry Data Book, 2nd Edition in S.I. Edition, John Murray, London (1982)

3 - F. P. Bundy, J. Geophys. Res, 1980, 85, 6930

4- Matt Latto, PhD thesis, University of Bristol, 2001

5 – Stephen Sque, PhD thesis, University of Exeter, 2005

6 – Yu. V. Pleskov Russian journal of electrochemistry, 2002, 38, 12, 1275-1291

7 – G.M. Swain, J.C. Angus, A.B. Anderson, MRS Bull, 1998, 9, 16-60

8 – G.M. Swain, Advanced Materials, 1994, 6, 388-392

9 – F. Bouamrane, A. Tadjeddine, J.E. Butler, R. Tenne, C. Levy-Clement, Journal of Electroanalytical Chemistry, 1996, 405, 95-99

10 – F. Beck, H. Krohn, W. Kaiser, M. Fryda, C.P Klages, L. Schafer, Electrochemical Acta, 1998, 44, 525-532

11- H.B. Martin, A. Argoitia, U. Landau, A.B. Anderson, J.C. Angus J. Electrochem. Soc, 1996, 143, L133

12 – T. N Rao, I. Yagi, T. Miwa, D. A. Tryk, A. Fujishima, Anal Chem, 1999, 71, 2506

13 – E. Popa, H.Notsu, T. Miwa, D.A Tryk, J.Electrochem. Solid State, 1999, 49, L2

14 –R. Ramesham, Thin Solid Films, 1999, 339, 82-87

15 – J. Iniesta, P.A. Michaud, M. Panizza, G. Cerisola, A. Aldaz, C. Comniellis, Electrochimica Acta, 2001, 46, 3573-3578

16 – J. C. Angus, C. C. Hayman, Science, 1988, 241, 913-921

17 – R. Ramesham, D. C. Hill, S. R. Best, M. F. Rose, R. F. Askew, Thin Solid Films, 1995, 257, 68-71

18 - A. J. Saterlay, J. S. Foord, and R. G. Compton, Electroanalysis, 2001, 13, 1065

19 - D. J. Twitchen, C. S. J. Pickles, S. E. Coe, R. S. Sussmann, and C. E. Hall, Diam. Relat. Chem., 2001, 10, 731

20 - A. Vlasov, V. Ralchenko, S. Gordeev, D. Zakharov, Vlasov, A. Karabutov, and P. Belobrov, Diam. Relat. Chem., 2000, 9, 1104

21 - H. P. Ho, K. C. Lo, S. C. Tjong, and S. T. Lee, Diam. Relat. Chem., 2000, 9, 1312

22 - S. Ertl, M. Adamschik, P. Schmid, P. Gluche, A. Floter, and E. Kohn, Diam. Relat. Chem., 2000, 9, 970.

23 - J. L. Davidson, W. P. Kang, Y. Gurbuz, K. C. Holmes, L. G. Davis, A. Wisitsora-at, D. V. Kerns, R. L. Eidson, and T. Henderson, Diam. Relat. Chem., 1999, 8, 1741

24 - E. Worner, C. Wild, W. Muller-Sebert, R. Locher, and P. Koidl, Diam. Relat. Chem., 1996, 5, 688

25 - C. E. Troupe, I. C. Drummond, C. Graham, J. Grice, P. John, J. I. B. Wilson, M. G. Jubber, and N. A. Morrison, Diam. Relat. Mater., 1998, 7, 575

26 - T. N. Rao, I. Yagi, T. Miwa, D. A. Tryk, and A. Fujishima, Anal. Chem., 1999, 71, 2506

27 - A. Denisenko, A. Aleksov, and E. Kohn, Diam. Relat. Chem., 2001, 10, 667

28 - N. Spataru, T. N. Rao, D. A. Tryk, and A. Fujishima, J. Electrochem. Soc., 2001, 148, E112

29 - N. Spataru, B. V. Sarada, E. Popa, D. A. Tryk, and A. Fujishima, Anal. Chem., 2001, 73, 514

30 - R. Uchikado, T. N. Rao, D. A. Tryk, and A. Fujishima, Chem. Lett., 2001, 144.

31 - K. Ohnishi, Y. Einaga, H. Notsu, C. Terashima, T. N. Rao, S. G. Park, and A. Fujishima, Electrochem. Solid State Lett., 2002, 5, D1

32 - C. Prado, G. U. Flechsig, P. Grundler, J. S. Foord, F. Marken, and R. G. Compton, Analyst, 2002, 127, 329

33 - F. Marken, C. P. Paddon, and D. Asogan, Electrochem. Commun., 2002, 4, 62

34 – C.H. Goeting, J.S. Foord, F. Marken, R.G. Compton, Diamond Relat. Mater., 1999, 8, L551

35 – T.A. Railkar, W.P. Kang, Henry Windischmann, A.P. Malshe, H.A. Naseem, J.L. Davidson, W.D. Brown, Critical Reviews in Solid State and Materials Sciences, 2000, 25(3), 163-277

36 – G.M. Swain, J.C. Angus and A.B. Anderson, MRS Bulletin, 1998, 9, 56

37 – K.A. Dean and B.R. Chalamala, Appl. Phys. Lett., 2000, 76, 375

38 – C. Dong and M.C. Gupta, Appl. Phys., 2003, 159, L83

39 - J. M. Stotter, S. Haymond, J. E. Butler, G. M. Swain, and J. K. Zak, Abstr. Pap. Am. Chem. Soc., 2001, 222, 117

40 - J. K. Zak, J. E. Butler, and G. M. Swain, Anal. Chem., 2001, 73, 908

41 – B. B. Pate, Surf. Sci., 1986, 165, 83

42 - R. G. Compton, F. Marken, C. H. Goeting, R. A. J. McKeown, J. S. Foord, G. Scarsbrook, R. S. Sussman, and A. J. Whitehead, Chem. Commun., 1998, 1961

43 - R. G. Compton, F. Marken, C. H. Goeting, R. A. J. McKeown, J. S. Foord, G. Scarsbrook, R. S. Sussman, and A. J. Whitehead, Chem. Commun., 1998, 1961

44 - J. S. Foord, K. B. Holt, R. G. Compton, F. Marken, and D. H. Kim, Diam. Relat. Chem., 2001, 10, 662

45 - W. Haenni, P. Rychen, M. Fryda and C.Comninellis,, Ch. Nebel, Ed, 2004, 149

46 - F. Maier, M. Riedel, B. Mantel, J. Rinstein, and L. Ley, Phys. Rev. Lett., 2000, 85, 3472

47 – R. G. Compton, F. Marken, C. H. Goeting, R. McKeown, J. S. Foord, G. Scarsbrook, R.S Sussmann, A. J. Whitehead, Chem Commun 1998, 1961

48 - C. H. Goeting, J. S. Foord, F. Marken, R. G. Compton, Diam, Relat. Mater., 1999, 8, 824

49 - R. Müller, A.Denisenko, M. Adamschik, E. Kohn; Diamond Rel. Mater., 2002, 11, 651

50 – A. Kraft, Int. J. Electrochem. Sci., 2007, 2, 355 - 385

51 - R. Kalish; Carbon, 1999, 37, 781-785

52 - R.Kalish, J.Phys. D: Appl. Phys; 2007, 40, 6467-6478

53 – T. Tshepe, J.F. Prins, M. J. R. Hoch, Diam. Rel. Mate., 1999, 8, 1508

54 – R. G. Compton, J. S. Foord, F. Marken, Electroanalysis 2003, 15, No 17

55 – G. M. Swain, R. Ramesham, Anal. Chem., 1993, 65, 345

56 – C. Lévy-Clément, F.Zania, N.A.Ndao, A. Deneuville, New Daim. Frontier Carbon Technol., 1999, 9, 189

57- M. Panizza, G. Cerisola; Electrochim. Acta; 2005, 51, 191-199

58 - Xu, J.S., Granger, M.C., Chen, Q.Y., Strojek, J.W., Lister, T.E. and Swain, G.M., Analytical Chemistry, 1997, 69, 19, 591-597

59 - Werner, M., Job, R., Zaitzev, A., Fahrner, W.R., Seifert, W., Johnston, C. and Chalker, P.R., Physica Status Solidi A-Applied Research, 1996, 154, 1, 385-393

60 – C. Lévy-Clément, F.Zania, N.A.Ndao, A. Deneuville, New Daim. Frontier Carbon Technol., 1999, 9, 189

61 - M. Hupert, A. Muck, J. Wang, J. Stotter, Z. cvackova, S. Haymond, Y. Show, G. Swain, Diamond Rel. Mater., 2003, 12, 1940 - 1949

62 - Jones, L. E; Thrower, P. A. Carbon 1991, 29, 251

63 - M. Hupert, A. Muck, J. Wang, J. Stotter, Z. cvackova, S. Haymond, Y. Show, G. Swain, Diamond Rel. Mater., 2003, 12, 1940 - 1949

64– Y. R. Zhang, S. Asahina, S. Yoshihara, T. Shirakashi, J.Electrochem. Soc., 2002, 149, H179

65– J. E. Butler, H. Windischmann, MRS Bull. 1998, 22

66 – R. Ramesham, R. F Askew, M. F. Rose, B. H. Loo, J. Electrochem. Soc.,1993, 140, 3018

67 – N. G. Ferreira, L. L. G. Silva, E. J. Corat, Diam. Rel. Mater. 2002, 11, 657

68 – K. Tsunozaki, Y. Einaga, T. N. Rao, A. Fujishima, Chem. Lett. 2002, 502

69 – R. Ramesham, Thin Solid Films 1999, 339, 82

70 – M. Fryda, D. Herrmann, L. Schafer, C. P. Klages, A. Perret, W. Haenni, C. Comninellis, D. Gandini, New Diam. Frontier Carb. Technol. 1999, 9, 229

71- C. H. Goeting, J. S. Foord, F. Marken, R. G. Compton, Diam. Rel. Mater., 1999, 8, 824

72- J. Shaw, A. N. Jones, P. M. S. Monk, C. A. Rego, Diam. Rel. Mater., 2002, 11, 1690

73 - M. Hupert, A. Muck, J. Wang, J. Stotter, Z. cvackova, S. Haymond, Y. Show, G. Swain, Diamond Rel. Mater., 2003, 12, 1940 - 1949

74 - J. Xu, M. C. Granger, Q. Chen, T. E. Lister, J. W. Strojek, G. M. Swain, Anal. Chem., 1997, A 69, 591

75 - G. M. Swain, A. B. Anderson, J. C. Angus, MRS Bull, 1998, 23, 56

76- F. Marken, R. G. Compton, C. H. Goeting, J. S. Foord, S. D. Bull, S. G. Davies, J. Solid State Electrochem., 2001, 5, 88

77 – H. B. Martin, A. Argoitia, J. C. Angus, U. Landau, J. Electrochem. Soc., 1999, 146, 2959

78 - I. Yagi, H. Notsu, T. Kondo, D. A. Tryk, A. Fujishima, J. Electroanal. Chem., 1999, 473, 173

79 – C. H. Goeting, F. Marken, A. Gutierrez-Sosa, R. G. Compton, J. S. Foord, Diam. Rel. Mater., 2000, 9, 390

80 – C. H. Goeting, F. Marken, C. Salter, R. G. Compton, J. S. Foord, Chem. Commun., 1999, 1697

81 – R. G. Compton, J. S. Foord, F. Marken, Electroanalysis 2003, 15, 17, 1350

82 - P. W. May, N. L. Allan, M. N. R. Ashfold, J. C. Richley, Y. A. Mankelevich, Diam. Rel. Mater., 2010, 19, 389-396

83 - A. Van der Drift, Philips Res. Rep. 1967, 22, 267

84 – J. C. Angus, C. C. Hayman, Science, 1998, 241, 913

85- F. G. Celi, J. E. Butle, Annu. Rev. Phys. Chem. 1991, 42, 643

86- C. Hammond, Introduction to Crystallography, Oxford University Press, London, 1992

87 - O. J. L. Fox, PhD Thesis, University of Bristol, 2011

88-D. M. Gruen, MRS Bull., 1998, 23, 32

89-D. M. Gruen, Annu. Rev. Mater. Sci., 1998, 29, 211

90- T. G. McCauley, D. M. Gruen , A. R. Krauss, Appl. Phys. Lett., 1998, 73, 1646

100 - H. Zheng, C. Ma, W. Wang, and J. Huang, Electrochem. Commun., 2006, 8, 6, 977–981

101- H. Lee, S. W. Yoon, E. J. Kim, and J. Park, Nano Letters, 2007, 7, 3, 778–784

102 - J. Filik, Spectroscopy Europe., 2005, 17, 10-17

103 - F. R. Kloss, M. Najam-Ul-Haq, M. Rainer, R. Gassner, G. Lepperdinger, C. W. Huck, G. Bonn, F. Klauser, X. Liu, N. Memmel, E. Bertel, J. A. Garrido, D. Steinmueller-Nethl, Journal of Nanoscience and Nanotechnology., 2007, 7, 4581-4587

104 – R. G. Forbes, Solid-State Electron., 2001, 45, 779

105 – A. V. Karabutov, V. I. Konov, S. M. Pimenov, E. D. Obraztsova, V. D. Frolov, V. G. Pereverzev, and A. A. Smolin, J. Wide Band Gap Mater., 1999, 7, 68

106- D. M. Gruen, MRS Bull. 2001, 26, 771

107 - Jiao, A. Sumant, M. A. Kirk, D. M. Gruen, A. R. Krauss, and O.Auciello, J. Appl. Phys. 2001, 90, 118

108 - Jiao, A. Sumant, M. A. Kirk, D. M. Gruen, A. R. Krauss, and O.Auciello, J. Appl. Phys. 2001, 90, 118

109- P. W. May, M. N. R. Ashfold, Y. A. Mankelevich, Journal of Applied Physics. 2007, 101, 053115 1-9

110 - Liu, X. Xiao, J. Wang, B. Shi, V. P. Adiga, R. W. Carpick, J. A.Carlisle, and O. Auciello, J. Appl. Phys. 2007, 102, 074115

111 - A. Williams, S. Curat, J. E. Gerbi, D. M. Gruen, and R. B. Jackman, Appl. Phys. Lett. 2004, 85, 1680

112 – http://www.chm.bris.ac.uk/pt/diamond/

113 - O. Auciello, J. Vac. Sci. Technol. 1981, 19, 841

114- G. Carter and V. Vishnyakov, Phys. Rev. B, 1996, 54, 17647

115 - C. Sun, W. J. Zhang, N. Wang, C. Y. Chan, I. Bello, C. S. Lee, and S. T. Lee, J. Appl. Phys. 2000, 88, 3354

117 - W. J. Zhang, X. M. Meng, C. Y. Chan, Y. Wu, I. Bello, and S. T. Lee, Appl. Phys. Lett., 2003, 82, 2622

118 –W. J. Zhang, Y. Wu, W. K. Wong, X. M. Meng, C. Y. Chan et al. Appl. Phys. Lett., 2003, 83, 3365

119 – J. Wang, Analytical Electrochemistry, 3rd ed, 2006, 149-151

120 – Lawrence, N. S., Pagels, M., Meredith, A., Jones, T. G. J., Hall, C. E., Pickles, C. S. J., Godfried, H. P. Banks, C. E., Compton, R. G., and Jiang, L. Talanta, 2006, 69, 829-834

121 – Tsunozaki, K.,Einaga, Y., Rao, T. N., and Fujishima, A. Chem. Lett., 2002, 5, 502-503

122 - Soh, K. L. Kang, W. P., Davidson, J. L., Basu, S., Wong, Y. M., Cliffel, D. E., Bonds, A. B., and Swain, G. M. Diam. Relat. Mater., 2004, 13, 2009-2015

123 – Provent, C., Haenni, W., Santoli, E., and Rychen., P. Electrochim. Acta, 2004, 49, 3737-3744

124 - W. P. Kang, J. L. Davidson, Sensors, 2009, 1780 -1783

125 -D J Zhong, F M Tao, Y L Xu, J P Jia Proc., IMechE Part E: J. Process Mechanical Engineering, 2007, 221, 201-205

126 – R. Saito, G. Dresselhaus and M. S. Dresselhaus, Physical Properties of Carbon Nanotubes, Imperial College Press, London, 1998

127 – R. L. McCreery, Chem. Rev., 2008, 108, 2646–2687

128 – S. Rosenblatt, Y. Yaish, J. Park, J. Gore, V. Sazonova and P. L. McEuen, Nano Lett., 2002, 2, 869–872.

129 - P. J. Britto, K. S. V. Santhanam and P. M. Ajayan, Bioelectrochem. Bioenerg., 1996, 41, 121–125

130 - H. Dai, Surf. Sci., 2002, 500, 218–241

131 - M. Pumera, Langmuir, 2007, 23, 6453–6458

132 - C. E. Banks, A. Crossley, C. Salter, S. J. Wilkins and R. G. Compton, Angew. Chem., Int. Ed., 2006, 45, 2533–2537

133 – B. Sljukic, C. E. Banks and R. G. Compton, Nano Lett., 2006, 6, 1556–1558

134 - W. J. Zhang, Y. Wu, W. K. Wong, X. M. Meng, C. Y. Chan et al. Appl. Phys. Lett., 2003, 83, 3365

135 – L. X. Zheng, M. J. O'Connell, S. K. Doorn, X. Z. Liao, Y. H. Zhao, E. A. Akhadov, M. A. Hoffbauer, B. J. Roop, Q. X. Jia, R. C. Dye, D. E. Peterson, S. M. Huang, J. Liu and Y. T. Zhu, Nat. Mater., 2004, 3, 673–676.

136 – A. K. Geim and K. S. Novoselov, Nat. Mater., 2007, 6, 183–191

137 – W. Liang et al, Nature, 2001, 411, 665

138 – S. P. Frank, P. Poncharal, Z. L. Wang, W. A. de Heer, Science, 1998, 280, 1744

139 - I. Dumitescue, P. Unwin and J. V Macpherson, Chem. Commun., 2009, 6886-6901

140– C. E. Banks and R. G. Compton, Analyst, 2006, 131, 15–21.

141 – C. E. Banks, T. J. Davies, G. G. Wildgoose and R. G. Compton, Chem. Commun., 2005, 829–841.

142 – C. E. Banks, R. R. Moore, T. J. Davies and R. G. Compton, Chem. Commun., 2004, 1804–1805.

143 – C. E. Banks and R. G. Compton, Analyst, 2006, 131, 15–21.

144 - Y. Zou, P. W. May, S. M. C. Vieira, and N. A. Fox, J. Appl. Phys., 2012, 112, 044903

145 - P. W. May, N. L. Allan, M. N. R. Ashfold, J. C. Richley, Y. A. Mankelevich, Diam. Rel. Mater., 2010, 19, 389-396

146 – P. Atkins, J. De Paula, Atkin's Physical Chemistry, 8th Ed, 2006, Chapter 7, 221

147 - M. Hupert, A. Muck, J. Wang, J. Stotter, Z. cvackova, S. Haymond, Y. Show, G. Swain, Diam. Rel. Mater., 2003, 12, 1940 – 1949

148 – R. Torz-Piotrowska, A. Wrzyszczyński, K. Paprocki, M. Szreiber, C. Uniszkiewicz, E. Staryga, J AMME, 2009, 37, 2 486-491

149 – Yu.V. Pleskov, Zashchita Metallov, 2006, 42, 2, 115–131

150 - H Ye, R Jackman, P Hing, J. Appl. Phys. 2003, 94, 7878

151 - H. Ye, O. A. Williams, R. B. Jackman, R. Rudkin, and A. Atkinson, Phys.status solidi A, 2002, 193, 462

152 - O.J.L. Fox, J.O.P. Holloway, G.M. Fuge, P.W. May, M.N.R. Ashfold, edited by P. Bergonzo, J.E. Butler, R.B. Jackman, K.P. Loh, M. Nesladek, Mater. Res. Soc. Symp. Proc. 2010, 1203, 17-27

153 - http://www.chm.bris.ac.uk/pt/diamond/

154 – E. Mahé, D. Devilliers, Ch. Comniellis, Electrochimica Acta, 2005, 20, 11 2263-2277

155 - M. Hupert, A. Muck, J. Wang, J. Stotter, Z. cvackova, S. Haymond, Y. Show, G. Swain, Diamond Rel. Mater., 2003, 12, 1940 - 1949

156 - M. Griffiths, C. Ponce de León, F. C. Walsh, AIChE J., 2005, 51, 682

157 –A.G. Guell, K.E. Meadows, P.R. Unwin, J.V. Macpherson, Phys Chem Chem Phys, 2010, 14-12(34):10108-14

158 - Sookhyun Hwang, Youngjoo Kim, Hyonkwang Choi, Minhyon Jeon, Sooyeon Lee, Chinese Journal of Physics, 2001, 49, 5, 1102-1110

159 – K.L. Moazed, R. Nguyen, J.R. Zeidler, Electron Device Letters, IEEE, 1988, 9, 7, 350-351

160 – S.J. Konopka, B. Mcduffie, Anal. Chem. 1970, 42:1741–1746